Studies towards the Data Acquisition of the $\overline{\text{P}}$ANDA experiment & Measurement of a new Upper Limit of the Production Cross Section of $p\bar{p} \to h_c$

Inauguraldissertation zur Erlangung des Doktorgrades
am
Fachbereich 07
Mathematik und Informatik, Physik, Geographie
der
Justus-Liebig-Universität Gießen

vorgelegt von

Milan Nicolas Wagner

aus Ehringshausen

Gießen (2016)

Dekan:	Prof. Dr. Bernhard Mühlherr
Prodekan:	Prof. Dr. Kai-Thomas Brinkmann
Gutachter:	Prof. Dr. Wolfgang Kühn
Gutachter:	Prof. Dr. Claudia Höhne

Für meine Frau

Selbstständigkeitserklärung

Ich erkläre: Ich habe die vorgelegte Dissertation selbstständig und ohne unerlaubte fremde Hilfe und nur mit den Hilfen angefertigt, die ich in der Dissertation angegeben habe. Alle Textstellen, die wörtlich oder sinngemäß aus veröffentlichten Schriften entnommen sind, und alle Angaben, die auf mündlichen Auskünften beruhen, sind als solche kenntlich gemacht. Bei den von mir durchgeführten und in der Dissertation erwähnten Untersuchungen habe ich die Grundsätze guter wissenschaftlicher Praxis, wie sie in der Satzung der Justus-Liebig-Universität Gießen zur Sicherung guter wissenschaftlicher Praxis niedergelegt sind, eingehalten.

Datum Unterschrift

Abstract

The $\overline{\mathrm{P}}$ANDA experiment will be one of the main future FAIR experiments located at Darmstadt, Germany. It has a challenging concept of a new type of Data Acquisition (DAQ) including the full online reconstruction and filtering as well as a high precision synchronization mechanism. The new concept is needed due to a high data rate of 200 GB/s, which has to be reduced by three orders of magnitude before storing.

In this thesis the prototype trigger-less DAQ, a field programmable gate array (FPGA) based system is presented. As a scalable system, it includes first parts of the final DAQ. Thus it is the first system allowing studies of the full DAQ-chain, including the synchronization mechanism. Furthermore, the functionalities during an in-beam enviroment test of the prototype of the $\overline{\mathrm{P}}$ANDA electromagnetic calorimeter were investigated. This test showed that the PTDAQ can be used as a DAQ in prototype tests.

In addition to hardware and firmware development, simulations of benchmark channels are crucial to extract filtering possibilities. Therefore the knowledge of the prodution cross section is necessary.

In the framework of this thesis a new upper limit of the production cross section $\sigma(p\bar{p} \to h_c)$ was extracted. h_c is one of the most unknown charmonium states, and it is not possible to produce pure h_c in one of the other "charm factories" directly. For this purpose, the branching ratio of the decay $\mathcal{B}(h_c \to p\bar{p}) < 5.6 \cdot 10^{-5}$ @ 90% $C.L.$ was determined. For this, data from the BES III experiment located at the BEPCII accelerator in Beijing, China was used. h_c was produced in the decay of the $\psi(2S)$ charmonium resonance, which itself was produced in e^+e^- collisions. A data set of $(447.9 \pm 2.8) \cdot 10^6$ $\psi(2S)$-events was used for this analysis.

The new upper limit of the cross section

$\sigma(p\bar{p} \rightarrow h_c) < 32\ nb$ @ 90% $C.L.$ was calculated by using the method of detailed balance. Furthermore, the lower limit of the integrated luminosity, which is needed to reach the upper limit of the decay $h_c \rightarrow J/\psi\pi^+\pi^-$ was determined to
$\mathcal{L}_{int} \geq 10.1\ pb^{-1}$ @ 90% $C.L.$. This integrated luminosity corresponds to a data taking of less than two hours at the high luminosity mode in the later stage of FAIR and 1.5 days as a worst case cenario in the beginning. For this calculation the estimated luminosities per day of the center of mass energies of the h_c were used.

Zusammenfassung

Das $\overline{\text{P}}$ANDA Experiment gilt als eines der wichtigsten Experimente der geplanten Anti-Protonen und Ionen Forschungsanstalt, welche gerade in Darmstadt, Deutschland gebaut wird. Das $\overline{\text{P}}$ANDA Experiment beinhaltet ein neues und innovatives Konzept zur experimentellen Datenaufnahme. Dazu gehört unter anderem eine vollständige Rekonstruktion, Entflechtung und Reduktion der Daten in Echtzeit, basierend auf deren physikalischen Eigenschaften. Der Grund für dieses neue Konzept liegt unter anderem in der hohen Datenrate von voraussichtlich 200 GB/s. Diese ist weitaus zu hoch um die Daten sinnvoll speichern zu können. Deshalb ist eine Reduktion der Daten um einen Faktor 1000 oder höher vorgesehen. Eine weitere Herausforderung liegt in der Synchronisierung der Ausleseelektronik, welche durch ein weiteres neues System namens SODANET erreicht wird.

In dieser Arbeit wird ein auf FPGA basierendes Prototypensystem mit Namen "prototype trigger-less data acquisition" vorgestellt. Es ist so geplant und angelegt, dass es durch einfache Erweiterungen zu der finalen DAQ von $\overline{\text{P}}$ANDA geführt werden kann. Bereits jetzt sind die ersten Funktionen der $\overline{\text{P}}$ANDA DAQ implementiert, so dass es als erstes vollständiges System, inklusive SODANET, zur Überprüfung der Funktionalität genutzt werden kann. Hierfür wurde an einem Test des Prototypen des elektromagnetischen Kalorimeters, des Proto120 im Photonenstrahl am Mainzer Mikrotron, teilgenommen. Dabei wurden erfolgreich über 88 Millionen Events aufgenommen.

Zusätzlich zu der Entwicklung von Hardware und Firmware ist die Simulation von Physikkanälen notwendig, um unter anderem Wege zur Datenreduzierung zu entwickeln. Hierfür allerdings ist es notwendig, den Produktionsquerschnitt in Proton Antiproton Reaktionen zu kennen.

Aus diesem Grund wurde im Zuge dieser Arbeit ein weiterer Aspekt untersucht, welcher sowohl hinsichtlich der DAQ als auch der Physik, die $\overline{\mathrm{P}}$ANDA untersuchen möchte, relevant ist. Es wurde eine neue obere Grenze für den Produktionsquerschnitt des h_c Charmoniums in Proton Anti-Proton Kollisionen ermittelt, welche kleiner als 89.6 nb @ 90% $C.L.$ ist. Dabei wurde die Methode des detaillierten Gleichgewichts angewendet.

Hierfür wurde eine neue obere Grenze von $5.6 \cdot 10^{-5}$ @ 90% $C.L.$ für das Verzweigungsverhältnis von $h_c \rightarrow p\bar{p}$ benutzt, welche im Rahmen dieser Arbeit bestimmt wurde. Die h_c wiederum entstanden durch den radiativen π^0 Zerfall des $\psi(2S)$ Charmoniums, welchen ich mit Hilfe eines Datensatzes von $(447.9 \pm 2.8) \cdot 10^6$ $\psi(2S)$ Zerfällen des BES III Experimentes in Peking, China untersuchen konnte.

Zum Schluß wurde die minimale integrierte Luminosität berechnet, welche benötigt wird um die obere Grenze des Verzweigungsverhältnisses von $h_c \rightarrow J/\psi\pi^+\pi^-$ zu erreichen. Mit Hilfe der abgeschätzten Luminositäten pro Tag wurde daraus berechnet, wie viele Tage reine Messzeit benötigt werden. Im Anfangsstadium von FAIR werden mindestens 1.5 Tage benötigt, und in der Endphase von FAIR mit dem Hoch- Luminositäts Modus, benötigt man nur mindestens 2 Stunden.

Contents

Chapter 1

Introduction & Motivation

The $\overline{\text{P}}$ANDA (Anti-Proton Annihilation at Darmstadt) experiment will be one of the main experiments at the future Facility for Anti-proton and Ion Research (FAIR), an expansion of the already existing Gesellschaft für Schwerionen (GSI), located in Darmstadt, Germany. As a fixed target experiment using either protons or nuclear targets and high precision cooled anti-proton beams with momenta between 1.5 GeV/c up to 15 GeV/c, it will be able to address fundamental questions of physics, focusing the non-pertubative region of the Quantum Chromodynamics (QCD) [63].

With an energy range between 2.3 GeV to 5.5 GeV, $\overline{\text{P}}$ANDA covers the full charmonium spectrum below and above the open charm threshold. Thus a search of exotic states like tetra quarks (either as a pure four quark composed state or as meson molecule), glueballs (pure gluon state) and hybrids (quark anti-quark pairs with an excited gluon) will be possible [63]. Furthermore the scientific program includes open charm spectroscopy, hypernuclear physics, nucleon structure physics and also studies of hadrons in matter [63].

The total proton-antiproton cross section, which is approximately 60 mb [73] in momentum range of the $\overline{\text{P}}$ANDA experiment, is about six orders of magnitude larger compared to exclusive processes, as it is indicated in figure 1.1.

To fulfill its scientific tasks, $\overline{\text{P}}$ANDA will have a high interaction rate of 20 MHz in average, with a peak up to 50 MHz. Since the event size will be around a few kilobytes, the Data Acquisition (DAQ) has to handle data rates of several hundreds of GB/s. A non-conventional, intelligent DAQ of the $\overline{\text{P}}$ANDA experiment will help to solve this problem. For an effective storing of the data, a reduction of at least three orders of magnitude will be accomplished. In most of the proton anti-proton reactions light hadrons are produced directly, these events are handled as a background. Unfortunately, these events have the same topological signatures than many of the benchmark channels. Due to this the DAQ will be operating trigger-less in a free streaming mode. Instead of triggering, online event filtering using real-time tracking, particle identification and calorimetry information will be performed.

For the filtering, it is necessary to investigate strategies to separate the hadronic background from the signal. Therefore, precise simulations are required and the knowledge of the production cross sections in proton anti-proton annihilations is necessary. Unfortunately, not even all of the production cross sections of charmonium states are known yet.

These cross sections can be estimated theoretically using several models, for example annihilations of di-quark pairs [54], quark-gluon string models [11], or an ansatz using hypothetic contributions of $D\bar{D}$ molecule pairs to the resonances above the open-charm threshold [32].

Another possibility of getting at the cross sections of the charmonia in proton anti-proton reactions is to use the method of detailed balance, which is based on the time-reversal-invariance of QCD. Here one measures the partial width of the decay of the charmonium into $p\bar{p}$ and calculates the cross section. One possibility for this is to produce charmonia in electron–positron–collisions and to analyse their partial decay width into proton anti-proton pairs.

The third generation of the Beijing Electron Spectrometer (BES III) located at the second generation of the Beijing Electron-Positron Collider (BEPCII) in Beijing, China is able to fulfill this scientific task. BEPCII is a symmetric electron positron collider with energies in the charm and τ physics region from around 1.8 GeV up to 4.6 GeV [13] [23]. BES III is an ongoing experiment, nevertheless it has already accumulated the largest data set of on-resonance charmonia.

In this thesis I will focus on both of these topics, with the aim to contribute to solving the problem of how to treat the differences in the cross sections between the total proton-antiproton cross section and the cross sections of exclusive processes. In the frame of this thesis the first Prototype Trigger-less Data Acquisition (PTDAQ) for the $\overline{\text{P}}$ANDA experiment was constructed, which was running in an in-beam environment. Furthermore, a determination of a new upper limit of the production cross section of $p\bar{p} \to h_c$, which is identified from the decay of $\psi(2S) \to h_c\pi^0$ while h_c is going to $p\bar{p}$, was performed.

After a short introduction of the $\overline{\text{P}}$ANDA physics program in chapter 2, I will introduce the $\overline{\text{P}}$ANDA detector, including a detailed description of the DAQ concept in chapter 3 and 5. In chapter 4 the BES III experiment will be introduced. Furthermore, the PTDAQ will be explained in chapter 7, followed by a detailed analysis of the online data taking test. Besides, the upper limit extraction will be described in chapter 8. Finally, these two topics will be summarized and discussed.

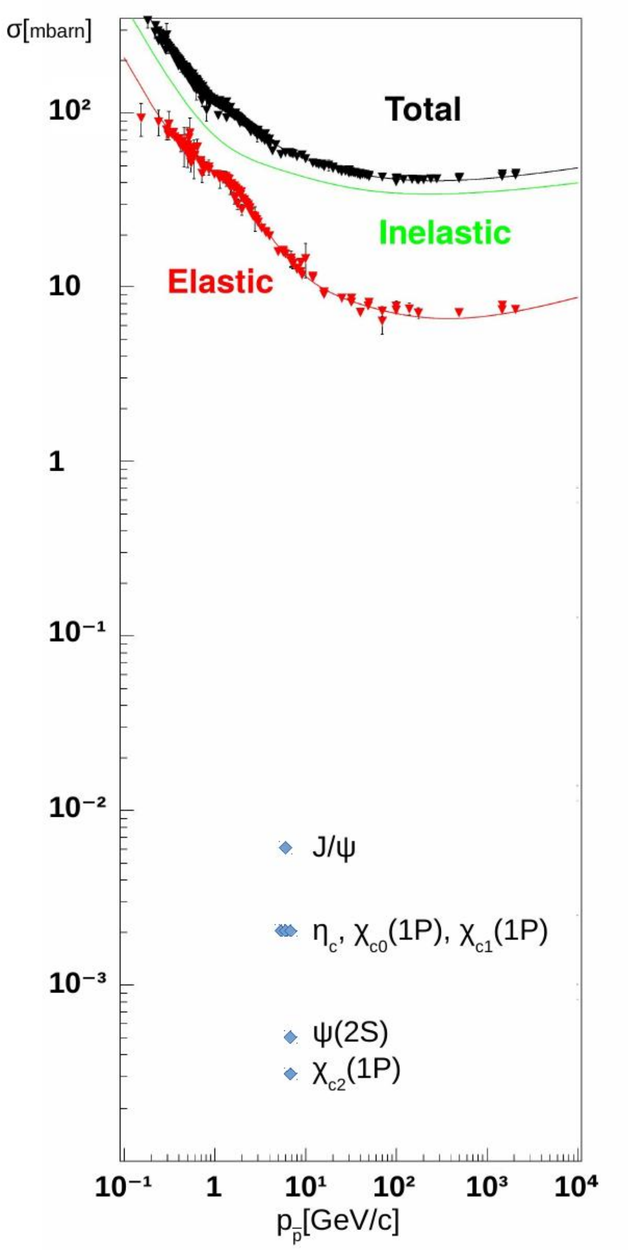

Figure 1.1: The total (black) and elastic (red) cross section for the anti-proton proton reaction, as function of antiproton beam momentum. While the contribution of inelastic events is also shown (green line), the estimated production cross sections of the charmonia are indicated via blue rhombi. The figure is adapted from [56] and the cross sections are calculated by using the ansatz of detailed balance similar as used in [18].

Chapter 2

The $\overline{\text{P}}$ANDA Physics Program

This chapter reviews the phenomena the $\overline{P}$ANDA experiment will investigate. After a short theoretical introduction about the standard model of particle physics, including a description of elementary particles and their interactions, I will illustrate the possibilities of major explorations in hadron physics that $\overline{P}$ANDA can achieve.

2.1 The Standard Model of Particle Physics

The matter surrounding us is build of elementary particles. These particles do not have any substructure by the actual state of knowledge. The theory describing the properties of these particles and their interactions, excluding gravitation, is the Standard Model (SM). It is a relativistic Quantum Field Theory (QFT) combining electro–weak–theory and QCD. In a QFT, interactions as well as particles are described by fields. The elementary particles and their interactions are described in the following sections.

The SM is a gauge theory based on Lie groups [31]. Lie groups are able to characterize the local gauge invariance, one of the basic requirements of a QFT. Local gauge invariance describes an invariance under a set of local transformations, i.e. transformations whose parameters are space-time dependent. The full symmetry group of the standard model is [76]:

$$SU(3) \otimes SU(2) \otimes U(1) \tag{2.1}$$

While SU(3) is a special unitary 3×3 matrix, SU(2) is a special unitary 2×2 matrix and U(1) a unitary matrix.

Furthermore gauge theories are invariant under the kind of gauging.

2.1.1 Elementary Particles

Elementary particles are divided into two categories, depending on their spin. Fermions have spin 1/2, while bosons have integer spin.

The fermions are classified as leptons and quarks. They can be sorted in three so–called generations. Table 2.1 shows the fermions and their properties. To each fermion belongs a corresponding antifermion with equal mass, but opposite charge.

Leptons					
generation		mass $\left[\text{MeV}/c^2\right]$	electromagnetic charge	weak charge	strong charge
1^{st}	e^-	0.511	-1	yes	no
	ν_e	< 0.000225	0	yes	no
2^{th}	μ^-	105.658	-1	yes	no
	ν_μ	< 0.19	0	yes	no
3^{rd}	τ^-	1776.82	-1	yes	no
	ν_τ	< 18.2	0	yes	no
Quarks					
generation		mass $\left[\text{GeV}/c^2\right]$	electromagnetic charge	weak charge	strong charge
1^{st}	up u	0.0023	$+2/3$	yes	yes
	down d	0.0048	$-1/3$	yes	yes
2^{th}	charm c	1.275	$+2/3$	yes	yes
	strange s	0.095	$-1/3$	yes	yes
3^{rd}	top t	173.5	$+2/3$	yes	yes
	bottom b	4.18	$-1/3$	yes	yes

Table 2.1: Fermion properties [73]

Another type of elementary particles are the bosons. In the SM, two kinds of elementary bosons are included: The force carrier bosons with quantum numbers $J^{PC} = 1^{--}$, and the Higgs boson with quantum number $J^{PC} = 0^{++}$. A third kind of elementary boson would be the graviton with quantum numbers $J^{PC} = 2^{++}$. Unfortunately there is no theory which includes the gravitation successfully in the SM yet.

The force carrier bosons are the photon, the $W^\pm$, the Z^0 and the gluons.

The photon (γ) is a massless, electrically neutral particle with spin

1. It mediates the electromagnetic force.

In case of the weak force, there are two different kinds of mediator bosons: One electrically neutral, the Z^0 with a mass of 91.1876 GeV/c^2, and two electrically charged, the $W^\pm$ with a mass of 80.399 GeV/c^2 [73].

The gluons g are massless and electrically neutral. They are the mediators of strong interaction. A gluon is carrying a colour and a different anticolour charge.

The Higgs boson is the quantum exitation of the Higgs field. The interaction between quarks, leptons and the heavy elementary bosons with the field generates their masses.

2.1.2 $SU(2) \otimes U(1)$; Electroweak Interaction

The electromagnetic interaction between electrically charged particles is described by Quantum Electrodynamic (QED), which was the first Abelian local gauge invariant QFT, invented in the late 40's of the last century. Represented by the unitary group $U(1)$, QED is the most precise and best proven theory of an interaction.

In 1934 Enrico Fermi proposed the beta-decay-theory, which was inspired by the QFT [42]. Later on this lead to the weak interaction, which was unified together with EM interaction from Sheldon Glashow, Abdus Salam, and Steven Weinberg [89].

The charged current of the weak interaction (exchanging $W^\pm$-bosons) allows flavour changing. In the SM flavour changing neutral currents at tree level are forbidden. A mechanism called the GIM mechanism, invented by S.L. Glashow, J. Iliopoulos and L. Maiani [45], assures no flavor changing without changing an electromagnetic charge. Only higher order diagrams like box or penguin diagrams using $W^\pm$ allow this kind of transitions.

2.1.3 $SU(3)$; Strong Interaction

$SU(3)$ is the special unitary group with dimension of 3. The number of gauge bosons n is given by $n = DIM^2_{group} - 1$, so that there are 8 gluons [76]. The charge of the strong interaction is described by the concept of colour, therefore the strong interaction is also called colour force. In this description a quark is carrying a colour of red

(r), blue (b) or green (g), while antiquarks are carrying a colour of antired ($\bar{r}$), antiblue ($\bar{b}$) or antigreen ($\bar{g}$). This leads to the name QCD. QCD is a non Abelian gauge theory featuring self-coupling of gluons carrying a colour and a different anticolour. The gluons are either $r\bar{g}$, $r\bar{b}$, $g\bar{r}$, $g\bar{b}$, $b\bar{r}$, $b\bar{g}$, $1/\sqrt{2}(r\bar{r} - g\bar{g})$ or $1/\sqrt{6}(r\bar{r} + g\bar{g} - 2b\bar{b})$ [76]. The strenght of the coupling constant α_s is dependent on the momentum transfer Q^2 or the distance and is shown in figure 2.1. Admittedly the strenght of each coupling constant is Q^2 dependent, but in case of the QCD this phenomenon is most distinct.

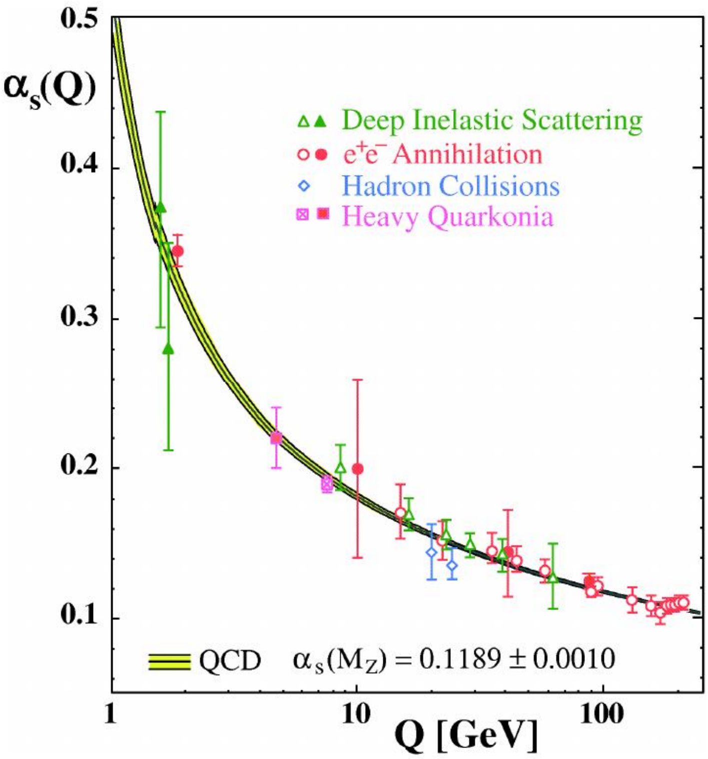

Figure 2.1: World data of measurements of α_s as a function of the respective energy scale Q. The curves are the QCD predictions for the combined world average value of α_s [29].

The coupling gets very weak at high Q^2. This phenomenon is called asymptotic freedom. The range of the strong force is roughly about 1 fm, equivalent to the diameter of a nucleon. The fact that there are no observations of free gluons and quarks is called confinement.

2.2 Hadron Spectroscopy

One of the main physics topics of the $\overline{\text{P}}$ANDA experiment is the hadron spectroscopy, especially the spectroscopy of charmonia [63].

A charmonium is a meson consisting of $|c\bar{c}\rangle$. Charmonia exist in a region from 2.9 GeV to 4.5 GeV [73]. Charmonium states can be classified by using their quantum numbers, either using spin S, orbital momentum L, and total momentum J similar to the atom spectroscopy, or J, the parity $P = -1^{(L+1)}$, and charge conjugation $C = -1^{(L+S)}$ [76].

Charmonium spectroscopy is a powerful probe of non-pertubative QCD. The spectrum of charmonium states can be calculated by solving non-relativistic Schrödinger equations including a potential description of the QCD $V(r)$ [35]. Due to the relatively high mass of a charm quark ($m_c \approx 1.3$ GeV), relativistic effects are negligible. The simplest approach is based on the phenomenological derived Cornell potential using one gluon exchange [35].

$$V(r) = \frac{-4}{3}\frac{\alpha_s}{r} + k \cdot r \tag{2.2}$$

In this potential, α_s is the strong coupling constant and k is the string tension covering the linear behaviour in large distances.

To get more precise results, one can add terms covering the coupling of the orbital momentum and the spin V_{LS}, the spin spin coupling V_{SS} and a tensor term V_T.

$$V(\vec{r}) = -\frac{4\alpha_s}{3r} + kr + V_{SS} + V_{LS} + V_T \quad (2.3)$$

$$V_{SS} = \frac{2\left(\vec{S}_1 \cdot \vec{S}_2\right)}{3 \cdot m_q^2} \cdot \nabla^2 dV_v(r) \quad (2.4)$$

$$V_{LS} = \frac{\vec{L} \cdot \vec{S}}{2 \cdot m_q^2 r}\left[3\frac{dV_v}{dr} - \frac{dV_s}{dr}\right] \quad (2.5)$$

$$V_T = \frac{2\left[3\left(\vec{s}_1 \cdot \vec{r}\right)\left(\vec{S}_2 \cdot \vec{r}\right) - S^2\right]}{12m_q^2}\left[\frac{1}{r}\frac{dV_v}{dr} - \frac{d^2V_v}{dr^2}\right] \quad (2.6)$$

Here m_q is the quark mass, $V_v(r)$ the vector part from one-gluon (vector boson) exchange, V_S the scalar part from confining term, $\vec{L}$ is the orbital momentum and $\vec{S}$ is the corresponding spin of the particles.

As shown in figure 2.2, the theory fits in most instances with the established charmonia, especially below the $D\bar{D}$-threshold, where the mass of the charmonium state is not enough to decay into two D-mesons. These states are narrow according to the OZI rule, invented by Susumu Okubo, George Zweig and Jugoro Iizuka in the 1960s [72] [94] [49]. A qualitative explanation of this rule is: In contrast to charmonia decaying into D-mesons, the decays into light hadrons result in very energetic gluons with a high Q^2 and therefore a small coupling constant α_s [29]. Furthermore, quarkonia decaying into light hadrons need a minimum of two gluons to preserve the quantum numbers. In case of vector mesons like the J/ψ with quantum numbers $J^{PC} = 1^{--}$ even three gluons are needed to preserve the C-parity.

The J/ψ was discoverd in 1974 at Stanford Linear Acclerator Center (SLAC) and Brookhaven National Laboratory (BNL) [27] [26]. Afterwards many other charmonium states were discovered.
Nevertheless some of the predicted states are still not detected yet.

In 2003 a resonance was seen in the decay $B^{\pm} \to K^{\pm}\pi^{+}\pi^{-}J/\psi$ at the Belle experiment [74] called X(3872) with quantum numbers $J^{PC} = 1^{++}$ [12]. It is very close to the $D\bar{D}^{*}$-threshold, but too narrow for a conventional $c\bar{c}$ state and with almost 50 MeV very far from the next predicted pure charmonium state. It is decaying into $J/\psi + X$ [30] as well as into $\psi(2S)\gamma$ [25]. This indicates a $c\bar{c}$ content, due to this reason it is called charmonium-like state. Since that time several charmonium-like states were discovered, as shown in figure 2.2.

Three years ago a very interesting discovery was the Z(3900), in the decay chain $Y(4260) \to J/\psi\pi^+\pi^-$ [16]. The Y(4260) is another charmonium-like state, discovered by the BaBar experiment [24], thus one charmonium-like state is decaying into another one. Furthermore the Z(3900) is a charged state, which excludes the pure $c\bar{c}$ state immediately. Even more interesting was the discovery of its neutral partner, so that there is a full isospin-triplet of the Z(3900)-states [92].

These states are classified in three classes: Y states are neutral and have quantum numbers $J^{PC} = 1^{--}$, X states are also neutral with quantum numbers different to the Y states, and Z states are charged (except for the isospin-triplet partner $Z^0(3900)$).

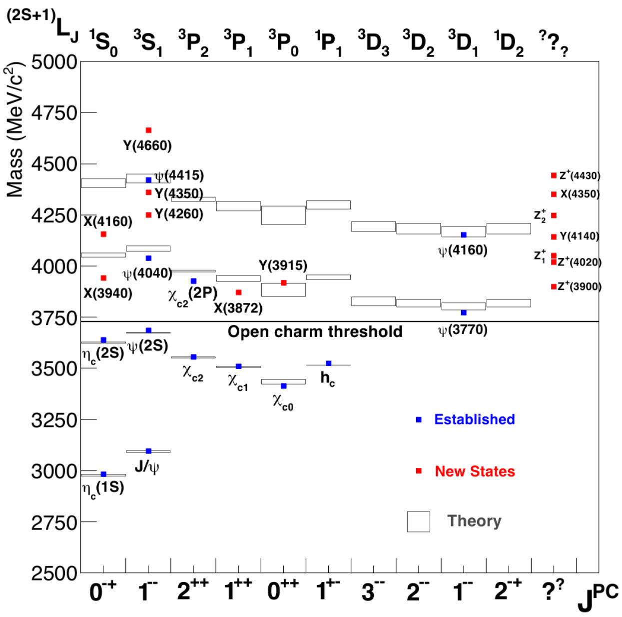

Figure 2.2: The charmonium spectrum: the grey boxes display the theoretically calculated states, the blue rectangles show the established charmonia and the red rectangles show charmonium-like states [10].

Till now the nature of these states is still unknown. There are various theoretical models trying to explain them, using different kind of internal structure ansatzes. The most common ones are listed below:

- Tetraquarks: A bound state consisting of two quarks and two anti-quarks. Either all four form a colorless state immediately, or build a coloured quark-anti-quark-pair before binding to the colorless object [58].
- Cusps: Several theoreticians, like D. V. Bugg [34] or E. S. Swanson [85], propose that the X, Y, Z states are a kinematical effect at the threshold.
- Meson molecules: This ansatz also uses two quarks and two anti-quarks, but in this case two colourless mesons are bound to the charmonium-like state [32] [70].
- Hybrid mesons: Here an exitation of a gluon leads to a new state [37].

The last model is not able to explain the Z(3900). Nevertheless it is not proven yet if all X, Y, and Z states are really the same type of state. There is even a fourth kind of non-conventional particle: the glueball, a state consisting of gluons only. The theoretical existance can be explained by using the gauge invariant QCD-lagrangian [76].

$$\mathcal{L}_{QCD}(q, A) = \bar{q}\,(i\gamma^{\mu}D_{\mu} - m)\,q - \frac{1}{4}G^{a}_{\mu\nu}G^{\mu\nu}_{a} \tag{2.7}$$

In this equation q and $\bar{q}$ represent the quark and anti-quark field, γ^{μ} is the Dirac matrix while $\mu/\nu = 0 - 3$, D_{μ} is the covariant derivative and $G^{a}_{\mu\nu}$ is the gluon field strength tensor:

$$G^{a}_{\mu\nu} = \partial_{\mu}A^{a}_{\nu} - \partial_{\nu}A^{a}_{\mu} + gf^{abc}A^{b}_{\mu}A^{c}_{\nu} \tag{2.8}$$

Here A^{a}_{μ} are the gauge boson fields while $a = 1 - 8$, f^{abc} is the structure constant and g is the coupling constant between quarks and gluons [76].

In contrast to the electromagnetic field strenght tensor in the QED lagrangian, the gluon field strength tensor $G^{a}_{\mu\nu}$ is squared in the QCD lagrangian. This allows self-interaction between gluons [76], so that a bound state of pure gluons is possible.

Since the gluon is a massless particle, the mass of glueballs is only created by the strong interaction. For this reason studying glueballs enables a unique approach to the mass creation by the strong interaction.

Even though glueballs with non exotic quantum numbers are able to mix with $q\bar{q}$ states of the same quantum numbers, which complicates the distinction, one has various possibilities to identify glueballs. For example each quarkonium nonet for a given J^{PC} contains two isospin zero neutral mesons; finding a third one would theoretically hint that one of the three could be a glueball candidate. Due to the mixing the distinction is more complicated, because all of these three candidates will have a gluonic content. To identify the gueball candidate with the strongest gluonic content, one can use quark model calculations for example, which predict the order of the total width of pure $q\bar{q}$-states. In case of $q\bar{q}$-states in the light quark sector with quantum numbers 0^{++} the order should be:

$$\Gamma(n\bar{n}) > \Gamma(s\bar{s}) > \Gamma(a_0) \geq \Gamma(K^*)$$

where $n\bar{n} \equiv (u\bar{u} + d\bar{d})/\sqrt{2}$. The total width of a_0 is $\Gamma(a_0) = 265 \pm 13\ MeV$ [73], the total width of K^* is $\Gamma(K^*) = 270 \pm 80\ MeV$ [73], the total width of a pure $n\bar{n}$ state is expected to be $\Gamma(n\bar{n})700MeV$ [20], and in case of a pure $s\bar{s}$: $\Gamma(s\bar{s})500MeV$ [20].

As these widths indicate, the narrow state $f_0(1500)$ with a width of 109 MeV [73] is considered as a possible candidate for the glueball ground state ($J^{PC} = 0^{++}$) with a mixing with the nearby states of the 0^{++} $q\bar{q}$ nonet [20].

Another possibility to identify the gueball candidate with the strongest gluonic content is to analyse the decay rates of the state. Pure glueballs have to decay flavor-blind, which means that – different to mesons – glueballs should decay into all flavor varieties. The decay rates for the mixed states of scalar glueballs in the light quark sector can be found in [20].

Furthermore, glueballs can have exotic quantum numbers e.g. $J^{PC} = 0$, $J^{PC} = 1^{+}$, or $J^{PC} = 2^{+}$, which are forbidden for mesons[1].

[1] These quantum numbers are not forbidden for tetraquarks, hybrids and meson-molecules.

2.3 Hadron Production

Hadrons are produced in particle interactions. For example, one can use electron positron interactions like the BES III experiment [13], or hadron and anti-hadron interactions, which will be used at the $\overline{\text{P}}$ANDA experiment [75]. Furthermore, interactions like proton and proton at the LHC are possible, but they will not be further discussed in this thesis.

One distinguishes two different kinds of production mechanisms: The formation, where the initial particles form one final particle, and the production, which produces several particles as a final state. This is indicated in figure 2.3

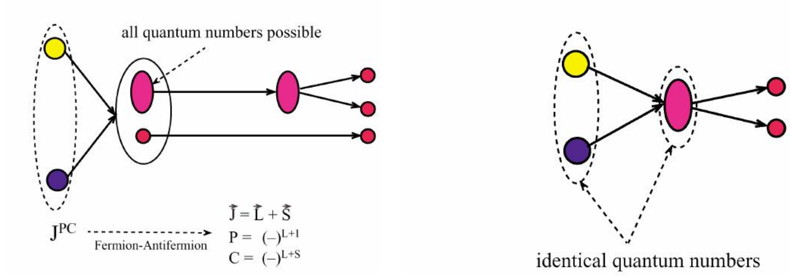

Figure 2.3: Left: Illustration of the production mechanism. Right: Illustration of the formation mechanism [63]

In electron positron interactions the quantum numbers of the final state are fixed to the virtual photon[2] quantum numbers $J^{PC} = 1^{--}$. Other quantum numbers e.g. $J^{PC} = 1^{++}$ are also possible, but since this would be a second order photon exchange it would be suppressed by a factor of $\alpha^2 \approx 1/18769$ [73]. To have access to particles with different quantum numbers, one either has to analyse the production reaction of a specific hadron together with some other hadrons, like neutral pions for example $\psi(2S) \to h_c\pi^0$ [14], or one has to analyze radiative decays from higher lying resonances like $\psi(2S)$ or $\psi(3770)$ via real photon to the η_c or χ_c states [68] [17].

In contrast to electron-positron interactions the dominating interaction in anti-hadron hadron reactions is the strong interaction. Furthermore, hadron and anti-hadron are composite particles. This kind of interaction allows an orbital momentum inbetween the par-

[2]In interactions, with center of mass energies below the mass of the Z-boson, the virtual Z is suppressed.

ticles, so that all non-exotic quantum numbers, shown in table 2.2, can be formed.

L	0		1				2		
J^{PC}	0^{-+}	1^{--}	0^{++}	1^{+-}	1^{++}	2^{++}	2^{--}	2^{-+}	3^{--}
# gluons	3		2				3		

Table 2.2: Possible initial state quantum numbers depending on the number of gluons and the angular momentum between the anti-proton and the proton.

The production mechanism in anti-proton proton reactions allows states with exotic quantum numbers (not shown in table 2.2) together with an additional recoil particle. A neutral pion with $J^{PC} = 0^{-+}$ as recoil particle would allow the production of $J^{PC} = 1^{-+}$ and 2^{+-} exotic states.

2.4 Hadrons in Nuclear Matter

Another interesting topic is the predicted shift of hadron masses and widths of mesons when produced in nuclear matter. This has been studied for light hadrons in proton-, photon- or nucleus-nucleus collisions [63]. Theories predict a mass shift at finite density for vector mesons [19], due to chiral dynamics and partial restoration of the symmetry in a hadronic medium. The aim of the $\overline{\text{P}}$ANDA experiment is to study cold implantation of heavy quarks through antiproton-nucleus collisions in the region of charmonium and open-charm [63].

2.5 Nucleon Structure

The next important topic covered by the $\overline{\text{P}}$ANDA experiment is the investigation of the nucleon structure. Real and virtual Compton-scattering of photons on the nucleus is an essential technique to obtain structural information of the nucleon. Inclusive deep-inelastic scattering can lead to more precise knowledge of the quark and anti-quark distributions in the nucleon via a measurement of the forward virtual Compton amplitude [63]. In the $\overline{\text{P}}$ANDA experiment one will use crossed-channel Compton scattering:

$$p\bar{p} \to \gamma\gamma$$

Theoretically this process can be described with the model of Generalized Parton Distributions (GPDs) for large s values [28]. Measuring the differential cross sections of the Compton scattering in the crossed-channel and in the related exclusive annihilation channels can be compared with theoretical calculations based on GPDs. In the exclusive annihilation channels one of the photons is forming a vector meson or a lepton pair or is replaced by a scalar meson in the final state. This will provide an improved understanding of the annihilation process and its description with QCD [63].

Another theoretical approach describing the process $p\bar{p} \to \gamma\gamma$ are the so-called Transition Distribution Amplitudes (TDAs) [77] parameterizing the transition of a proton into a (virtual) photon according to the right diagram in figure 2.4. It is also possible to describe the exclusive meson production $p\bar{p} \to \gamma\pi^0$ using TDAs [78].

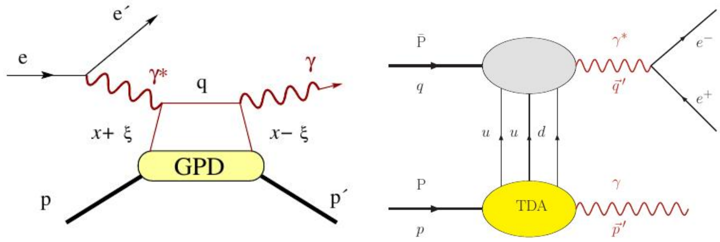

Figure 2.4: Left: Simplified diagram of the deep-inelastic Compton-scattering described by the GPD. Right: The diagram of $p\bar{p} \to \gamma\gamma$ including TDA [63].

Furthermore the $\overline{\text{P}}$ANDA experiment will investigate the time-like form factor of the proton [63]. The form factors can be expressed as a function of the four momentum transfer:

$$q^2 = w^2 - \vec{q}^{\,2} \tag{2.9}$$

In this equation q is the full four momentum transfer, w the energy transfer, and $\vec{q}$ the momentum transfer.

Depending on the sign of q^2, there are two regions called time–like ($q^2 > 0$) and space–like ($q^2 < 0$) form factors. In a non-relativistic interpretation, form factors are used to describe the internal structure of a hadron. Fourier transformations of space-like electric $|\mathrm{G}_E|$ and magnetic $|\mathrm{G}_m|$ form factors are used to describe the spatial charge and magnetization distribution of a hadron, while the time-like factor can be interpreted as the frequency spectrum of the electromagnetic response of the nucleon [63].

As shown in figure 2.5, the space-like form factor is studied over the full region of $-Q^2$. It can be extracted via electron scattering. In contrast to this, the time-like form factor is only investigated in the lower region of Q^2. Next to the kinematical threshold $Q^2 = 4m_p^2c^4$ measurements were done [63]. In the high Q^2 region just a few data points with low statistics were measured [56], so that $|G_e|$ and $|G_m|$ form factors could not be separated. By using $p\bar{p} \rightarrow e^-e^+/\mu^-\mu^+$ events, $\overline{\text{P}}$ANDA will be able to measure up to $Q^2 = 15GeV^2$ [63]. Furthermore, analysing $p\bar{p} \rightarrow e^-e^+\pi^0$ or $p\bar{p} \rightarrow \mu^-\mu^+ + \pi^0$ will enable $\overline{\text{P}}$ANDA to explore the so-called unphysical region below the threshold [63].

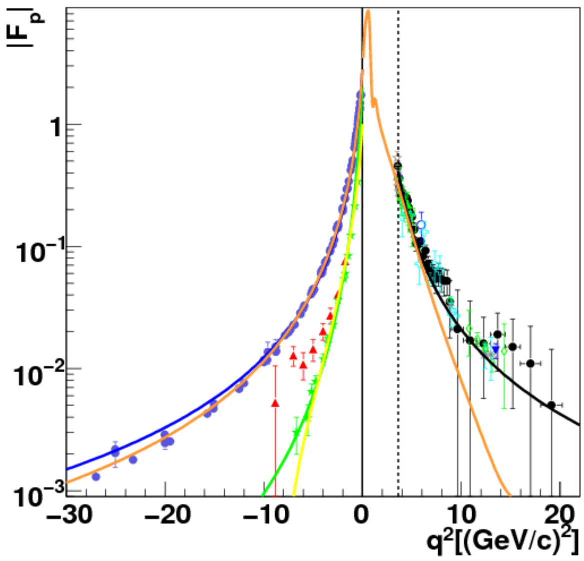

Figure 2.5: World data on proton form factors as function of q^2 from [86]. $q^2 < 0$: $|G_m|$ data (blue circles), dipole function (blue line); electric form factors, $|G_E|$, from unpolarized measurements (red triangles) and from polarization measurements (green stars). The green line is a monopole prediction for the ratio $|G_E| / |G_m|$. Time-like region ($q^2 > 4M_p^2$): $|G_E| = |G_m|$ (various symbols). Shifted dipole (black line); prediction from vector-meson-dominance model [48] (yellow line).

2.6 Hypernuclear Physics

A hyperon is a baryon with at least one strange quark, e.g. the Λ which is a neutral baryon with quark content uds. By exchanging a nucleon in a nucleus with a hyperon, one obtains a hypernucleus. Even though the first hypernucleus was already discovered 1952 in Warsaw by Marian Danysz and Jerzy Pniewski [91] and single Λ–hypernuclei were studied up to ${}^{208}_{\Lambda}Pb$ [71], the overall knowledge of double hypernuclei states is quite low. By now merely 6 double Λ–hypernuclei were found [63].

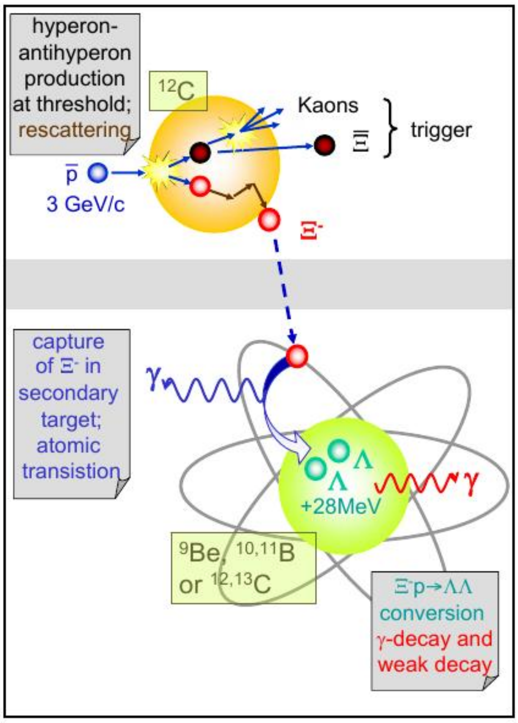

Figure 2.6: Schematical view of the hypernuclei production at $\overline{\text{P}}$ANDA . The figure is taken from [63]

At $\overline{\text{P}}$ANDA double Λ–hypernuclei will be produced in two steps. First Ξ^+ Ξ^- pairs will be produced in anti-proton interactions with a ^{12}C target. The Ξ^- will produce a double Λ–hypernucleus in a secondary nuclear target, as shown in figure 2.6. For the hypernucleus physics a dedicated configuration of the experimental setup of the $\overline{\text{P}}$ANDA detector is required, more information is available at [63]. A high production rate of Λ–hypernuclei will allow measurements of the decay properties as well as level scheme [63].

Chapter 3

The $\overline{\text{P}}$ANDA Experiment

In this chapter the $\overline{\text{P}}$ANDA experimental setup is described. The target- and forward spectrometer will be briefly discussed. Furthermore a short overview of the FAIR, where the $\overline{\text{P}}$ANDA detector will be located, is given at the beginning.

3.1 FAIR

One of the main physics projects in Europe in the field of basic science is the expansion of GSI into FAIR, shown in figure 3.1. This upgrade includes new synchrotrons and storage rings, which provide high intensity heavy ions, up to uranium, and rare isotopes as well as high precision anti-proton beams. This allows a broad spectrum of research opportunities [79]:

Atomic and Plasma Physics and Applications (APPA) will investigate plasmas at high pressure and low temperatures as they exist e.g. in the interior of large planets. Furthermore, it will improve materials for space missions and will research for more efficient methods of the use of ion beams for curing cancer.

Nuclear Structure, Astrophysics and Reactions (NUSTAR) will enhance the knowledge of the inner parts of a star. Also it will analyse nuclear configuration of the great amount of heavy elements and the internal structure of neutron stars and will try to solve other astrophysical problems.

Other research opportunities are Compressed Baryonic Matter (CBM) physics that will search for the chiral symmetry restoration and the origin of hadron masses among other things, and finally physics which will use anti-proton annihilation ($\overline{\text{P}}$ANDA).

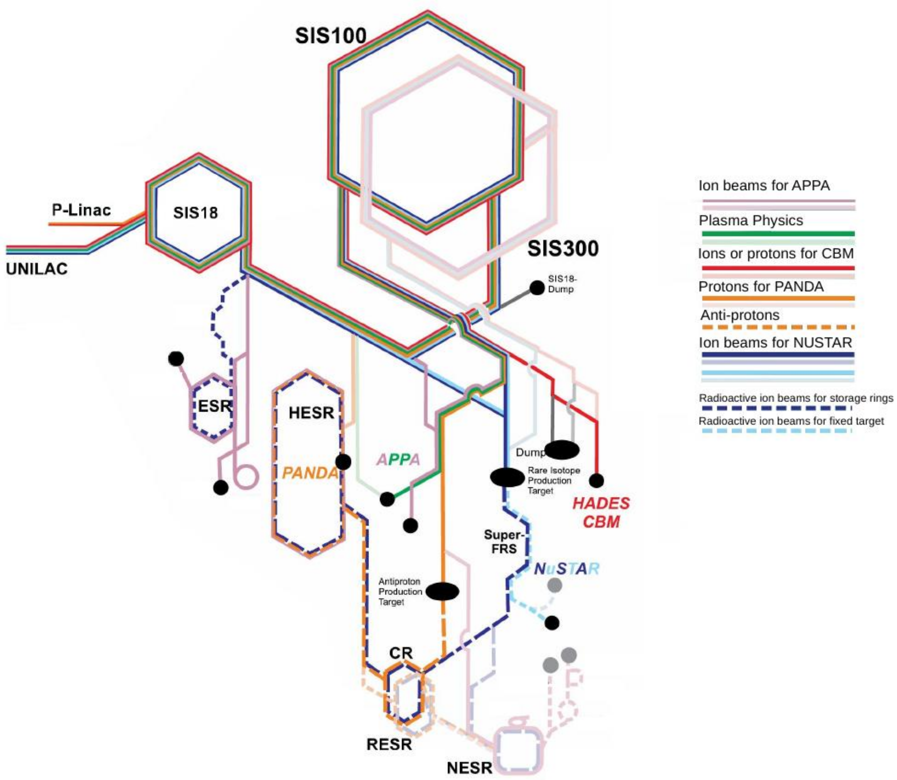

Figure 3.1: Schematical view of the FAIR facility based on a drawing from Petra Schütt. It displays the Synchrotrons (SIS18, SIS100 and SIS300), the Collector Ring (CR), the Experimental Storage Rings (ESR, NESR, HESR), the Fragment Separator (FRS) and the accumulator ring (RESR). The bright colours indicate the modularized start version of FAIR, while the pale colours show modules which will be build in an upgrade. The solid lines show the primary beam lines and the dashed lines show the secondary beam lines. The main experiments are Atomic and Plasma Physics and Applications (APPA), Nuclear Structure, Astrophysics and Reactions (NUSTAR), Compressed Baryonic Matter (CBM) and $\overline{\text{P}}$ANDA .

After the pre-acceleration in the Linear Accelerator (p-LINAC) and the heavy-ion-synchrotron (SIS 18), protons will be accelerated in SIS 100 to an energy up to 29 GeV. In interactions with a 60 mm thick nickel target [82] anti-protons will be produced, which will be filtered by a magnetic separator. After stochastic cooling in the Collector Ring (CR), the anti-protons will be injected into the High Energy Storage Ring (HESR) [79].

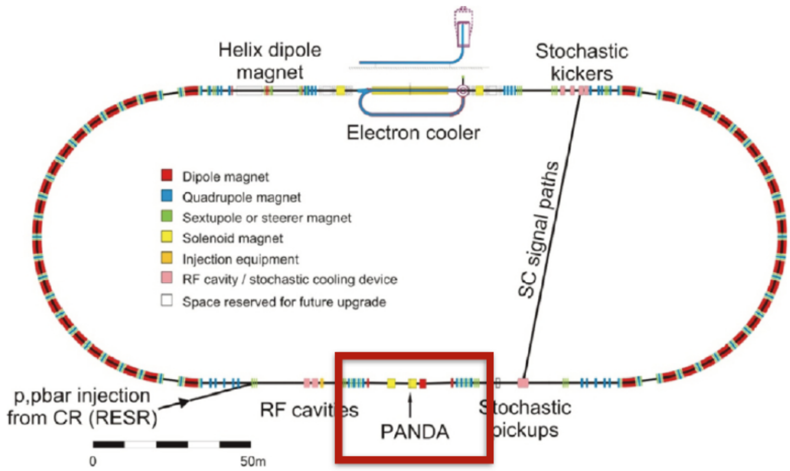

Figure 3.2: Schematical view of the HESR, with an indication of the location of the $\overline{\text{P}}$ANDA detector as well as the injection point of anti-protons from the CR. The figure is taken from [75].

Designed for a momentum range from 1.5 GeV/c to 15 GeV/c, the HESR shown in figure 3.2 will provide accumulation and final cooling for the anti-proton beam [84]. The HESR will have two different kinds of operating modes: One with a Root Mean Square (RMS) momentum spread of $\sigma p/p \leq 4 \cdot 10^5$ in the momentum range from 1.5 to 8.9 GeV/c and a luminosity ($\mathcal{L}$) of $\mathcal{L} = 2 \cdot 10^{31}\ cm^{-2}s^{-1}$, called High Resolution mode (HR), and one with a high intensity beam of 10^{11} anti-protons, leading to a luminosity of $\mathcal{L} = 2 \cdot 10^{32}\ cm^{-2}s^{-1}$ called High Luminosity (HL) mode [75]. This mode will have a RMS momentum spread of $\sigma p/p \approx \cdot 10^4$ in the momentum range of 1.5 to 15 GeV/c.

In case of the start version of FAIR the Luminosity will be reduced. A table displaying the estimated luminosities of certain anti-proton momenta is given in the attachment F.

3.2 The $\overline{\text{P}}$ANDA Detector

The $\overline{\text{P}}$ANDA experiment will be a fixed target experiment consisting of a target- and a forward-spectrometer displayed in figure 3.3.

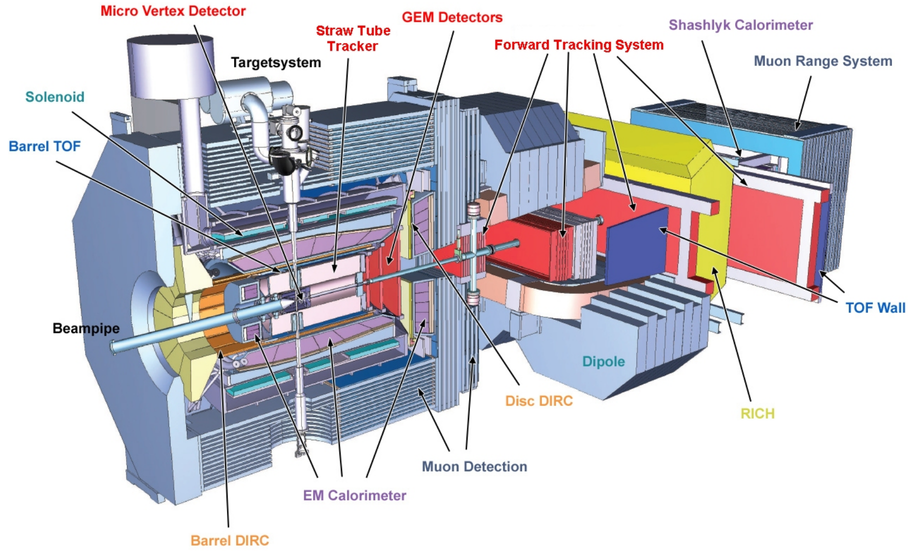

Figure 3.3: Schematical view of the $\overline{\text{P}}$ANDA detector. Shown are the target- and forward spectrometers and their detector components Micro Vertex Detector (MVD), Detection of Internally Reflected Cherenkov (DIRC), Time of Flight (ToF) detectors, Electromagnetic Calorimeter (EMC), Gas Electron Multiplier (GEM), the magnets, the muon detectors and the beampipe. The figure is taken from [6].

3.2.1 The Target System of the $\overline{\text{P}}$ANDA Detector

The design of the $\overline{\text{P}}$ANDA detector allows exchangeable targets. To reach the luminosity, a density of $4 \cdot 10^{15}$ H_2 per cm^2 has to be achieved [75]. It is also designated to use heavier gas tpyes like deuterium, nitrogen or argon as targets. In case of hydrogen two different types of targets, a **Hydrogen Pellet Target** and a **Cluster Jet Target**, are under development. Studies beyond anti–proton–proton collisions, like in hypernuclear physics and anti–proton–nuclear collisions, will be realised with solid targets [75].

By dribbling frozen gas molecules, called pellets, via a very fine nozzel into the vacuum, the hydrogen pellet target will get access to high effective densities. The lateral spread of the pellet stream is constrained by a radius from 25 μm to 4 μm, and a relative momentum spread of 1 mm [75]. Due to the frequency dependance of this approach its time distribution will be non–uniform. This leads to a larger variation of the instantaneous luminosity, compared to the cluster jet target [75].

The cluster jet target will be established by streaming a homogeneous, condensed and cooled gas into the vacuum, also using a nozzel. This approach will provide a continuous, controllable target density. By using hydrogen as a gas, 10^3 to 10^6 molecules will cluster in average [75]. The uncertainties of the interaction point, in case of a cluster jet target, in the plane perpendicular to the beam axis is defined by the focus of the beam and along the beam axis the lateral spread of the jet [75].

3.3 Target Spectrometer

The target spectrometer shown in figure 3.4 consists of several subdetectors which are described in the following sections.

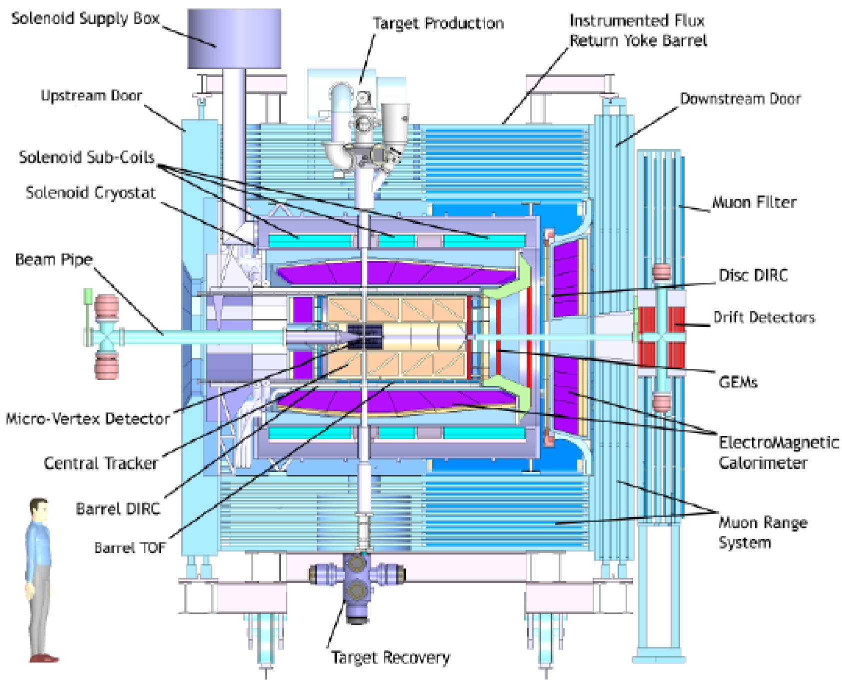

Figure 3.4: Side view of the target spectrometer [75]. It will consist of several subdetectors to allow tracking, particle identification, and calorimetry. Furthermore the magnets and the beam pipe are shown.The figure is taken from [75].

3.3.1 Solenoid Magnet

The superconducting solenoid magnet will have a lenght of 2.8 m, an inner radius of 90 cm and will use a laminated iron yoke for flux return. It will provide a homogenuous 2 T magnetic field with a uniformity better than 2%. From the specification it is limited to $\int B_r/B_z < 2\ mm$ [75].

3.3.2 Micro Vertex Detector (MVD)

The innermost part of the $\overline{\mathrm{P}}$ANDA detector will be the MVD. It will consist of two pixel- and two doublesided-stipe-layers of radiation-hard silicon. Arranged in a barrel-like shape, it will have an inner radius of 2.5 cm and an outer radius of 13 cm [75]. In addition to the barrelshape detector, six disks (four pixel and two stripe disks) will be implemented in forward direction. The MVD will mainly be used for reconstructing the primary vertex. In addition it will be used to reconstruct secondary verticies, and it will also improve the momentum resolution in case of tracking.

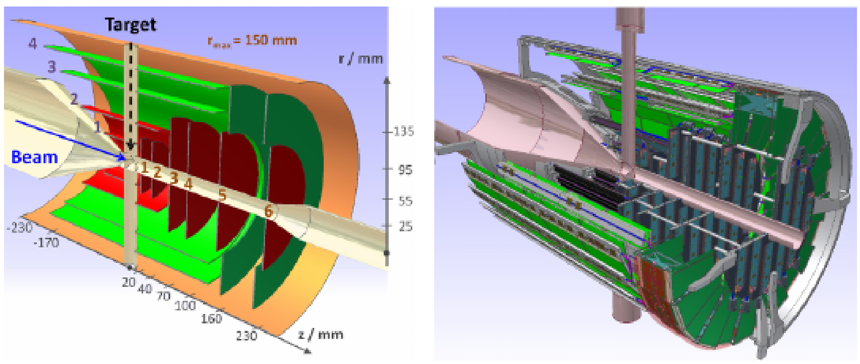

(a) (b)

Figure 3.5: Schematical view of the MVD layout (a) silicon pixel detectors in red and double-sided silicon stripe detectors in green, (b) a CAD drawing of the detector. The figure is taken from [75].

3.3.3 Straw Tube Tracker (STT)

The MVD will be surrounded by another tracking detector, the STT. A straw tube is an aluminised mylar tube with a radius of 5 mm [75]. For stabilization it is operated with 1 bar over-pressure. Each tube will surround a gold plated tungsten wire of 20 μm thickness. Consisting of 4636 straws, the STT will be arranged in 27 layers in a hexagonal shape, as shown in figure 3.6. 8 skewed stereo layers will allow a 3 mm resolution in the direction of the beam. A resolution higher than 150 μm in the plane perpendicular to the beam axis will be achieved.

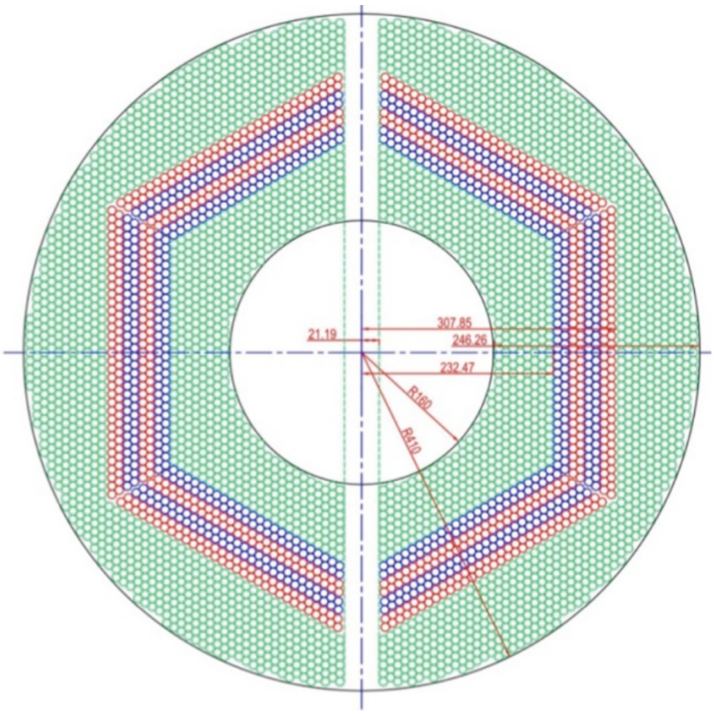

Figure 3.6: Cross section of the plane perpendicular to the beam axis of the straw tube tracker [60]. The stereo layers are indicated in blue and red.

3.3.4 Gas Electron Multiplier (GEM) Foils based Detector

Since the STT is not fully covering particles emitted lower than 22° polar angle, Gaseous micro-pattern detectors based on GEM foils will be used to increase the acceptance of the detector. Three double planes with two projections per plane in distances of approximately 1.1 m, 1.4 m and 1.9 m downstream of the target will be installed.

The GEM detector will be able to handle very high counting rates of around $3 \cdot 10^4 cm^{-1}s^{-1}$, due to relativistic boost of the reaction products as well as the small angle $p\bar{p}$ elastic scattering [75].

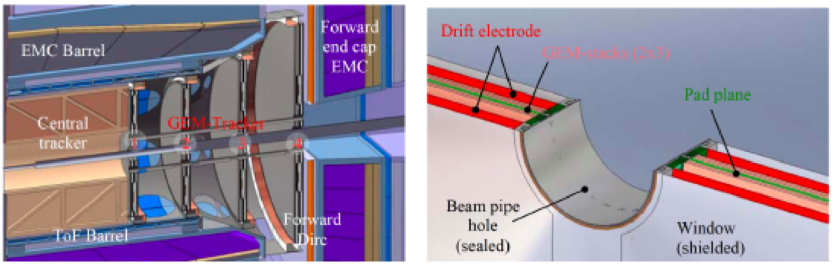

(a) (b)

Figure 3.7: Schematical view of the Gas Electron Multiplier detectors with location indication in the target spectrometer (a) and internal structure of a single disk (b) [75].

3.3.5 Particle Identification (PID)

The identification of particles is an important issue of every high energy experiment. In the $\overline{\text{P}}$ANDA experiment a concept based on information of several subdetectors is used for this purpose. To distinguish pions and muons, information determined by the μ-detector will be used. A separation of electrons and photons will be achieved by using information determined by the EMC. A pion/kaon/proton separation will be obtained by measurements of the energy loss (dE/dx) of charged particles in the tracking detectors and their time of flight, together with measurements of Cherenkov-light.

In the target spectrometer the Cherenkov-light will be measured by using the concept of Detection of Internally Reflected Cherenkov (DIRC). The detector will be divided in a barrel DIRC covering the angles between 22° and 140° and a Disc DIRC for the forward direction of the target spectrometer. In the following section the detector will be described briefly.

DIRC

Cherenkov light is emitted as soon as a particle has a velocity v above the Cherenkov threshold in a certain medium. Formula 3.1 relates the velocity of the particle and the angle of the emitted Cherenkov photon.

$$v = \arccos \frac{1}{n\beta} \tag{3.1}$$

Here n is the refraction index and $\beta = v/c$.

In the $\overline{\text{P}}$ANDA experiment 80 slices of artificial quartz (fused silica) with a thickness of 1.7 cm and a refractive index of 1.47 will be used. The Cherenkov-light will propagate via internal reflection inside the radiator slice to its end. There the light will enter a focusing volume with a reduced refraction index, to increase initially small angular differences. Due to the operating in the magnetic field, the readout of this detector will be done by using Micro-Channel Plate Photomultiplier Tubes (MCP PMTs) [75].

The Cherenkov angle can be reconstructed by using the position measurement ($RMSp \simeq 150\ \mu m$) as well as time information, with a resolution better than 50 ps. Furthermore tracking informations from the the inner tracking detectors will be used.

Afterwards, the charged particles can be identified by using the velocity of the particle, which can be calculated by using equation 3.1, and its momentum known from the inner tracking detectors.

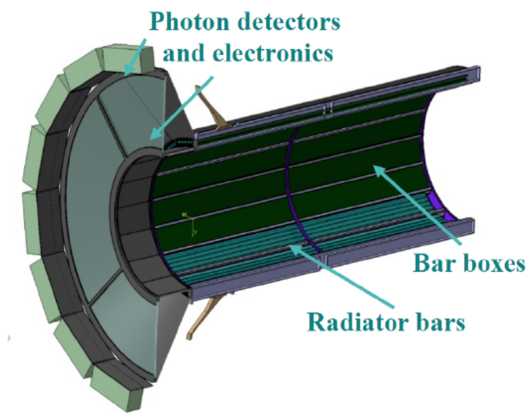

Figure 3.8: Simplified structure of the barrel DIRC. The figure is taken from [46].

The barrel DIRC will not be able to cover the full polar angle range. For this reason, an additional DIRC detector will be placed in front of the forward end-cap EMC in a distance of 2 m from the IP. It will hedge a polar angle between 5° and 22°. The forward end-cap DIRC will consist of four regular dodecagon shape plates, each 2 cm thick, expressing four independent quadrants of the disc with a radius of 110 cm [75].

Time-of-Flight

A second type of particle identification detector is planned to be used in the $\overline{\text{P}}$ANDA experiment: The scintillator tile barrel detector will be used to measure the time of flight of slow particles with large polar angles. It will consist of 5760 scintillating tiles with a size of $28.5 \times 28.5\ mm^2$ placed outside the DIRC detector. Additionally, 1000 tiles will be arranged in the forward part. This detector will be read out by two silicon photo multipliers per tile and give a precise time measurement of approximately 100 ps [75].

3.3.6 Electro Magnetic Calorimeter (EMC)

The EMC of the $\overline{\text{P}}$ANDA experiment will provide precise identification of electrons, positrons and photons in a broad enery range from 10 MeV up to 15 GeV, for almost 4π coverage. Furthermore, the EMC will provide a timing resolution of $\sigma_t < 1\ ns$. A list of requirements is displayed in table 3.1

General properties	Required performance value		
energy resolution σ_E/E	$\leq 1\% \oplus \leq 2\%/(E/GeV)$		
energy threshold (photons)	10 MeV		
energy threshold (singel crystal)	3 MeV		
RMS noise (energy equivalent)	1 MeV		
angular coverage in % of 4	99		
Subdetector specific requirements	backward	barrel	forward
	$\geq 140°$	$\geq 22°$	$\geq 5°$
energy range maximum	0.7 GeV	7.3 GeV	14.6 GeV
spatial resolution σ_θ	0.5°	0.3°	0.1°
maximum signal load f_γ	100 kHz		500 kHz
shaping time t_s	400 ns		100 kHz
maximum annual dose	10 Gy		125 Gy

Table 3.1: List of requirements for the $\overline{\text{P}}$ANDA EMC, taken from [39].

The scintillating material of the EMC will be lead tungstate, $PbWO_4$ (PWO). It is also used in the electromagnetic calorimeter of the Compact Muon Solenoid (CMS) experiment at the LHC. It emits an almost Gaussian shaped scintillation spectrum with a wavelenght of $\lambda_{mean} = 420\ nm$ and a Full Width at Half Maximum (FWHM) of 40 nm.

The advantages of PWO are the high effective atomic number $Z_{eff} = 75.6$, a radiation lenght $X_0 = 0.89\ cm$ and a small Moliere radius of 2 cm. Nevertheless, PWO has a disadvantage, too. Compared to NaI[1] it has a very low light yield. The relative Light Yield

[1] The light yield of NaI is used as a reference for all scintillating materials.

(LY) to NaI, in case of PWO used in CMS, is only 0.3%. A second version of PWO (PWO-II) was developed by the $\overline{\text{P}}$ANDA collaboration to increase this value to LY = 0.6%. For this purpose, a different doping ratio of the rare earth elements, Lanthanum (La) and Yttrium (Y), is used in PWO-II. Furthermore, cooling the crystals down to $-25°C$ increases the value to LY = 2.5%.

The EMC will consist of 11.360 PWO-II crystals in the barrel part, and additional 4100 crystals distributed to forward and backward end cap, shown in figure 3.11. The layout of the EMC is constrained by the size of the solenoid magnet. The barrel part will be divided in to 16 similar slices, as shown in figure 3.9.

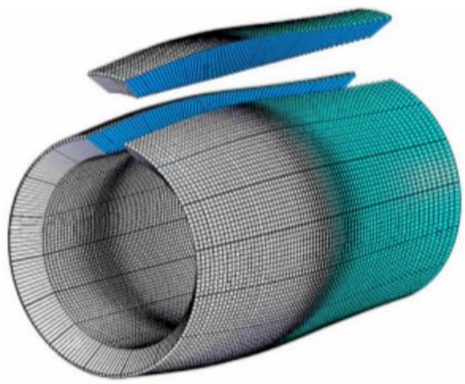

Figure 3.9: The layout of the barrel electro magnetic calorimeter indicating the 16 slices. The figure is taken from [81].

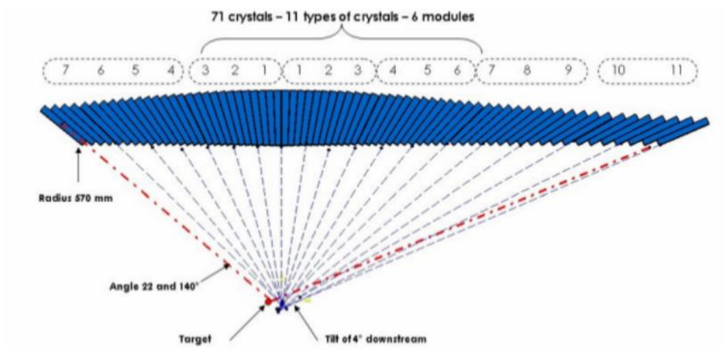

Figure 3.10: A single slice geometry. The figure is taken from [81].

To decrease the amount of material between the crystals and to reduce the amount of escaping photons, the crystals in each slice will be tilted by 4° in the polar angle as well as in the azimuthal angle with respect to the target. Due to this, as indicated in figure 3.9 (b), 11 slightly different parallelepiped shaped crystals will be used in a slice with a lenght of 200 mm.

Two different kind of photo sensors will be used in the EMC. Because of the magnetic field normal Photo Multipliers (PMs) are not suitable. In the barrel and the end-cap part Large Area Avalanche Photo Diodes (LAAPDs) will be used. For some crystals in the forward end-cap part under low polar angles Vacuum Photo Tetrodes (VPPTs) are foreseen.

A LAAPD is a photo diode based on a p-n-junction driven by a reverse bias voltage, which is significantly higher compared to conventional Si-photo diodes. This allows secondary ionizations, resulting in avalanches. The collected amount of charge is proportional to the primary charge. Depending on the bias voltage, an amplification factor of several hundred can be achieved, which is necessary because of the small LY of the PWO-II.

The LAAPDs have a rectangular shape with an active area of 1 cm^2. They are about 200 μm thick and have a high Quantum Efficiency (QE) in the wavelength range of PWO ($\sim$ 80%). Furthermore, they are insensitive to the magnetic field.

The VPPTs have a much faster response compared to the LAAPDs, thus they can be used in the high rate areas under low polar angles where event rates of up to 500 kHz are expected. In contrast to conventional PM, VPPTs can be operated in strong magnetic fields. While only one VPPT will be equipped to a crystal, two LAAPDs will be mounted on one to increase the active area.

The signals from the photo sensors will need an amplification. In the $\overline{\text{P}}$ANDA experiment two different preamplifiers will be used in the EMC: a customized Application-Specific Integrated Circuit (ASIC) for $\overline{\text{P}}$ANDA Front-end Electronics (APFEL ASIC) for the barrel part, and the Low Noise and Low Power charge Preamplifier (LNP-P) in the forward end-cap. The ASIC is designed to be equipped with two LAAPDs, while in the forward end-cap one will need one LNP-P for each LAAPD or VPPT, respectively [38].

As front end electronic devices sampling Analog to Digital Converter (sADCs) from Uppsala are foreseen. More information about the readout electronics can be found in chapter 7.2.

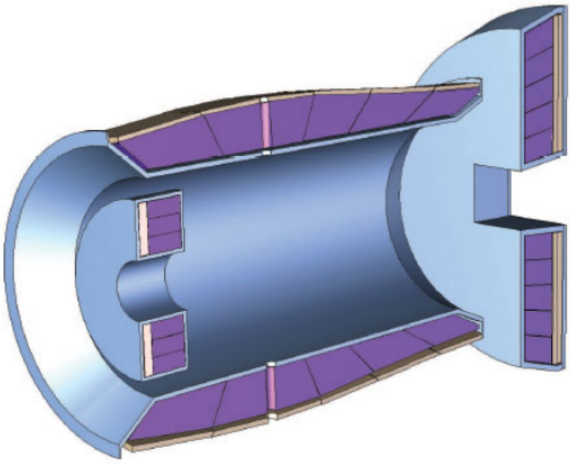

Figure 3.11: Layout of the barrel electro magnetic calorimeter including forward and backward end cap. The figure is taken from [81].

3.3.7 Muon Detector

Most of the particles passing the EMC and even the solenoid magnet will be pions and muons. To distinguish them is essential for the $\overline{\text{P}}$ANDA experiment. These particles will be minimal ionizing and will deposit around 1.5 GeV/m.

The separation of muons and pions can be divided into low and high energy areas. For low energies ($E \ll 1\ GeV$) pions and muons can be absorbed in this detector, which enables an energy measurement. While low energetic muons deposit most of their energy at the point of absorbtion, low energetic pions will deposit most of their energy in the first layers of the detector with a falling tail to further layers.

For high energies pions will produce a hadronic shower, while muons will pass the detector without being absorbed and leaving an almost straight ionization trace.

Therefore, a detector using the return yoke of the solenoid magnet as absorber material instrumented with rectangular aluminium Mini Drift Tubes (MDTs) will be installed. The sensitive MDT layers will alternate with 3 cm iron layers, while the innermost as well as the outermost absorber layer will be 6 cm thick. In the barrel region 13 layers are foreseen.

Since particle travelling in forward direction have higher momenta, due to the Lorenz-boost, the iron layers in the forward region will be 6 *cm* thick.

There will be 2,600 MDTs in the barrel part and 700 MDTs in the forward part [75].

3.4 Forward Spectrometer

A second spectrometer is placed in forward direction to increase the polar angle coverage to $5° < \Theta < 10°$ [75]. Due to the low transversal momenta of the particles travelling in forward direction, a different magnetic field geometry is required to measure their momenta. Its subdetectors will be briefly described in the following sections.

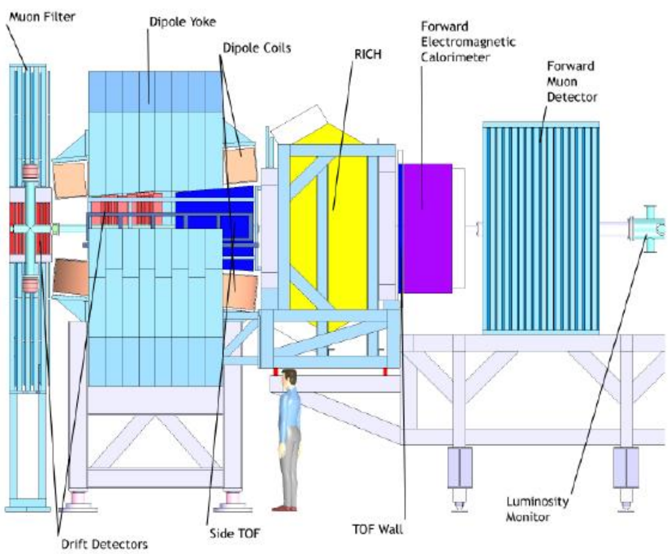

Figure 3.12: The forward spectrometer layout, showing all subdetectors [75].

3.4.1 Dipole Magnet

A 2 *Tm* dipole magnet will be placed in 4 *m* distance to the Interaction Point (IP) and will be used for the momentum analysis of charged particles in the forward direction. The non-reacting antiprotons will also be deflected (deflection of 2.2° at a momentum of 15 GeV/c) by the magnetic field. Since it is planned to reuse them, correction magnets will be placed around the detection system. The dipole magnet will have a lenght of approximately 2 m and a gap of 1 m [75].

3.4.2 Forward Tracker

To track the particles in the forward direction, 6 independent stations consisting of 4 double-layers of straw tubes will be used. The inner layers 2 and 3 of each station will be shifted by $\pm 5°$, to allow a tracking in the xy-plane. Two of these stations will be placed before, inbetween and after the dipole magnet, respectively [75].

3.4.3 Particle Identification

Kaons, pions and protons in a momentum range between 2 GeV/c and 15 GeV/c in forward direction will be separated by using a Ring Imaging Cherenkov Detector (RICH). The proposed detector setup will consist of two radiators, silica aerogel (refraction index 1.0304) and C_4F_{10} gas (refraction index 1.00137). The radiation lenght of the detector will be 10.8% X_0 [75].

Next to the RICH, a second detector type will be used for particle identification as well as for time of flight measuring. It will be a wall of plastic-scintillators with a time resolution of 50 ps placed 7 m away from the IP. This will allow a precise K/π and K/p separation in a momentum range between 2.8 GeV/c and 4.7 GeV/c. Since slow particles will not pass the dipole magnet, it is planned to build a smaller but similar detector inside the magnet [75].

3.4.4 Forward EMC

In the forward direction, 7.5 m from the target, photons and electrons will be detected by using a shashlyk-like calorimeter. The detector will consist of 351 modules (13 rows and 27 columns), while each of the modules will consist of a 680 mm long lead-scintillator with a lateral size of 110×100 mm. These modules will be read out by incorporated wavelength-shifting fibers coupled to photomultipliers. A higher granularity and an energy resolution of $4\% \sqrt{E}$ will be achieved by dividing each module into 4 readout sections [75], as shown in figure 3.13.

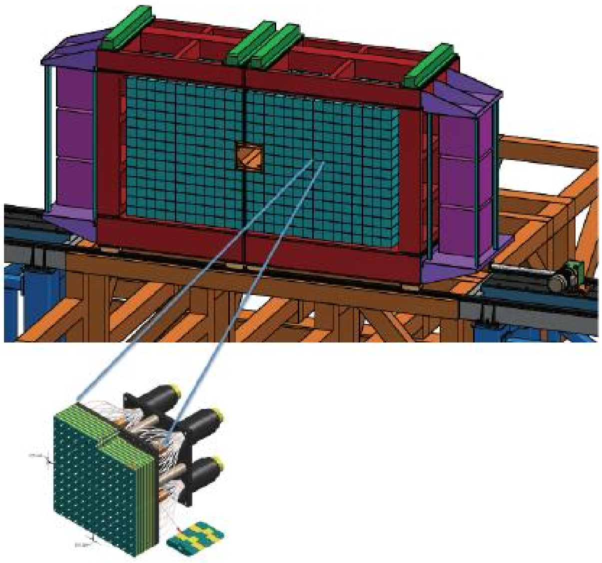

Figure 3.13: Forward EMC layout, with a zoom to show the internal structure[38].

3.4.5 Forward Muon Detectors

To distinguish pions and muons with very high momenta, a tracking detector of absorber layers and rectangular aluminium drift tubes will be installed in a distance of 9 m from the IP. This detector also allows the detection of pion decays and the approximate energy determination of neutrons and antineutrons [75].

3.4.6 Luminosity Monitor

Four layers of High Voltage-Monolithic Active Pixel Sensors (HV-MAPS) will be used to determine the luminosity at $\overline{\text{P}}$ANDA.

It will consist of diamond wafers with a pixel size of $80 \times 80\ \mu m^2$ [75]. It will measure the elastic scattering of the anti-proton with the protons of the target in the region of the interference between the Coulomb and the nuclear contribution at a small scattering angle [75].

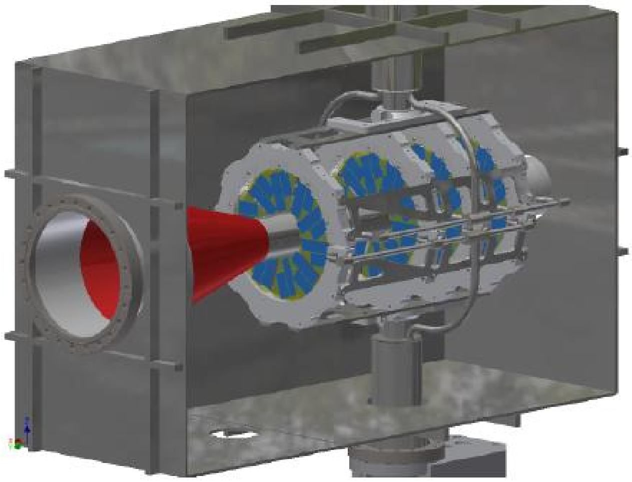

Figure 3.14: Schematical view of the luminosity detector[81].

3.5 Data Acquisition

The $\overline{\text{P}}$ANDA DAQ will be trigger-less using e.g. autonomous FEE, sampling ADCs with local feature extraction, and high level algorithms with event reconstruction. A detailed description of the $\overline{\text{P}}$ANDA DAQ is given in section 5.

In addition to the development of hard- and firmware for the DAQ, simulations are necessary to develop filter mechanisms. A simulation of a physics reaction needs various inputs, as e.g. the production cross section in proton anti-proton interactions.

The h_c is one of the most unkown charmonia below the open charm threshold, only 52 % of its decay channels are known yet. Within this thesis the upper limit of the production cross section of $p\bar{p} \to h_c$ was extracted from the decay of $\psi(2S) \to h_c\pi^0$ and $h_c \to p\bar{p}$. For this, a data set of $(447.9 \pm 2.8) \cdot 10^6$ $\psi(2S)$ events of the BES III experiment was used. In the next chapter a description of the BES III detector setup will be given.

Chapter 4

The Beijing Electron Spectrometer

To extract the upper limit of h_c production cross section in proton anti-proton collisions, I used a data set of approximately $(447.9 \pm 2.8) \cdot 10^6$ $\psi(2S)$*-events from the third version of the Beijing electron spectrometer [15]. In this chapter I will give a short overview of the BEPCII collider before I will explain the detector setup in detail.*

4.1 Beijing Electron Positron Collider

The Beijing Electron Positron Collider (BEPC) located at the Institute of High Energy Physics (IHEP) in Beijing, China, was hosting the two previous versions of the Beijing Electron Spectrometer (BES) experiment and BES II from 1989 till 2004. It was a symmetric single ring operating in a single bunch mode with a peak luminosity of $\sim 1 \cdot 10^{31} cm^2 s^{-1}$ in the energy region of charmonium and τ physics [13].

BEPCII, the new symmetric collider, is a completely new machine, including new beam pipes, the vacuum system, the magnets, and its power supplies. It is a double ring operating in a multi bunch mode to obtain a peak luminosity of $\sim 1 \cdot 10^{33} cm^2 s^{-1}$ [13], which allows the accumulation of large data samples in energies between $2 - 4.6\ GeV$ [13].

4.2 BES III Detector

The BES III detector shown in figure 4.1 is designed in a symmetric onion-shell layout. It consists of several subdetectors for tracking, particle identification and calorimetry. In the following sections each subdetector will be described briefly. For more information please see [13].

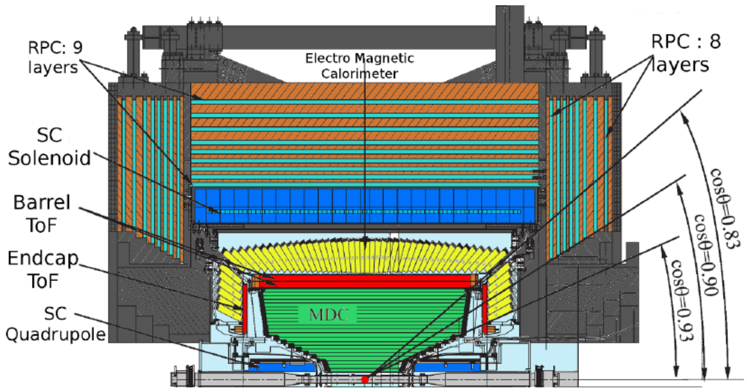

Figure 4.1: Artistic view of the BES III detector[88], showing all subdetectors including Mini Drift Chamber (MDC), the Time of Flight (ToF) and Resistive Plate Chambers (RPC) as well as the Superconducting (SC) magnets. The acceptance of the subdetectors is indicated via the $\cos(\theta)$.

The inner subdetectors, like the drift chamber, the time of flight detector, and the electromagnetic calorimeter, are surrounded by a superconducting solenoid magnet, which provides a 1 T magnetic field. Resistive plate chambers for pion muon separation are placed outside of the magnetic field [13].

4.3 Mini Drift Chamber (MDC)

The MDC is the tracking detector of BES III, also allowing dE/dx measurements. It is the innermost detector of the BES III experiment. Divided into an inner and an outer part with radii of 60 mm and 800 mm and a lenght of 2400 mm, it covers a polar angle of $|\cos\Theta| < 0.93$ and an azimuthal angle range of 0 to 2π. Together with the magnetic field, it provides a precise measurement of charge and momentum. The momentum resolution of a charged particle with a momentum of 1 GeV/c is 0.5% [13].

The gas mixture used in the MDC is 60 % He / 40 % C_3H_8. 6796

25 μm thick gold-plated tungsten signal wires, each surrounded by 8 field wires made of gold plated aluminum with a diameter of 110 μm, are distributed to 43 cylindrical layers of drift cells. Drift cells have a width of 12 mm in the inner part and 16.2 mm in the outer chamber. This leads to a spatial resolution of $\sigma_{r\phi} \sim 135\ \mu m$. To achieve a spatial resolution of $\sigma_z \sim 2\ mm$ in z-direction, the layer 8 as well as the layers 21 to 36 are stereo layers [13].

4.4 Time of Flight (ToF)

The ToF detector is used for two purposes. First of all it is used for particle identification. For up to 1 GeV/c particles a π/K separation at the 2σ level is possible. In addition it delivers a fast trigger signal.

Divided into a barrel and an endcap part, the ToF covers a polar angle of $|\cos\Theta| < 0.95$ in total. In this connection, the barrel part covers $|\cos\Theta| < 0.83$ and the endcap part covers $0.85 < |\cos\Theta| < 0.95$.

As detector material, plastic scintillators are used. In the barrel part, the scintillator bars have a length of 2380 mm and a thickness of 50 mm. By reading out the bars twosidedly, a time resolution of 100 ps can be obtained. The bars are mounted in two cylindrical layers around the MDC. 88 bars are used for this purpose.

In the endcap ToF, the plastic scintillators are fan-shaped with an inner radius of 410 mm and an outer radius of 890 mm. One layer of 48 scintillators is arranged behind the MDCs endplate. They are single-ended read out by a fine-mesh PMT. In case of di-muon events a time resolution of 110 ps is achievable. Unfortunately the time resolution for electrons in the endcap ToF is only 150 ps [13].

4.5 Electromagnetic Calorimeter (EMC)

Photon energies from 0.2 GeV to 2 GeV and their positions are measured by the EMC, which consists of 6240 thallium doped casium iodide (CsI(Tl)) scintillating crystals. 5280 crystals are arranged in 44 rings in the barrel part of the EMC. The rest are distributed in two endcaps in 6 rings each [13]. It is also used for electron/pion separation and a trigger signal.

The crystals itself have trapezoidal shape, with a lenght of 28 cm (corresponding to 15 X_0) and a size of the front face of 5.2 cm $\cdot$

5.2 *cm*. To avoid escaping photons, the crystals are tilted 1.5° in the direction of ϕ and 1.5° to 3° in the direction of Θ [13].

At an $\sqrt{s} = 3.686$ *GeV* Bhabha events were used to measure the energy resolution of 2.3% in the barrel and 4.1% in the endcap. For photons, the resolution is 2.7% for the barrel and 4.2% for the endcap systems. For 1 GeV photons the position resolution is 6 *mm* in the barrel part and 9 *mm* in the endcap.

The EMC covers an angle of $|\cos\theta| < 0.82$ in the barrel system, and the endcap covers a region of $0.83 < |\cos\Theta| < 0.93$ [13].

4.6 Muon detection

Muons are separated from hadrons by using Resistive Plate Chambers (RPC) which alternate with steel layers of the return yoke of the solenoid magnet. In the barrel, nine layers of RPCs are used. Since muons lose around 160 *MeV* of energy in the EMC, the minimal momentum to identify muons is 0.4 GeV/c [13].

Chapter 5

The $\overline{\text{P}}$ANDA DAQ

One main challenge of the $\overline{\text{P}}$ANDA experiment is the DAQ. With an event size of several kB, and an event rate of 20 MHz in average, a data rate of approximately 200 GB/s is expected at $\overline{\text{P}}$ANDA, which is way too much to store. In the following, the DAQ concept to handle the specific requirements will be explained.

5.1 Hardware Platforms & Processing Units

The final hardware of the $\overline{\text{P}}$ANDA DAQ is not decided yet. Several options are discussed as a processing unit, one is using Field-Programmable Gate Arrays (FPGAs). The main feature of this integrated circuit is the reconfiguration ability allowing the adaption of many different kind of purposes.

FPGAs consist of two basic components: flip-flops and Lookup Tables (LUTs). A flip-flop is a 1-bit register and a LUT is a truth-table allowing to generate almost every function with a fixed number of inputs. Furthermore, FPGAs can have more complex components like memory cells (block RAM) and clocking components like frequency synthesizers. Even more complex components like a completely integrated circuit e.g. a Central Processing Unit (CPU) can be built in. In addition, FPGAs have general-purpose input/output (I/O) ports to allow connections to external devices, like clock sources, memory chips and Ethernet Physical transceivers (PHYs) or to Multi-Gigabit Transceivers (MGTs) that allow high bandwidth data transfer up to 10 Gb/s.

The firmware for FPGAs can be written in a Hardware Description Language (HDL). The HDL used in this thesis is Very high speed integrated circuit (V)HDL. The firmware which is uploaded into the FPGA is called bitstream. The VHDL code is processed in several steps. The first step is "synthesizing" where the code is translated into a so-called netlist. In a second step called "place and route", the required components of the FPGA are assigned and the location of these components as well as the routing inbetween them is defined.

Other possible processing units would be ASICs, CPUs, and General-Purpose computing on Graphics Processing Units (GPGPU). All of them have their advantages and disadvantages. An ASIC for example can be run with higher frequencies compared to FPGAs. Furthermore, an ASIC is not limited to available resources and technologies of any given FPGA. The drawbacks are very high production costs and design efforts, and no flexibility. In the $\overline{\text{P}}$ANDA experiment ASICs will be used as Front End Electronics (FEE) devices like the APFEL ASIC for the barrel EMC or the PANDA Strip Asic (PASTA) [75] chip for the MVD.

CPUs or GPUs have several advantages. First of all the programming is more common in a way that the development of algorithms will need less manpower. Furthermore, algorithms that can be implemented can be more precise, due to the resource limitation of the FPGA. Nevertheless, providing the high bandwidth which will be needed in some parts of the $\overline{\text{P}}$ANDA experiment is very expensive.

5.1.1 Advanced Telecommunications Computing Architecture (ATCA)

Even though the FPGA based hardware used in the $\overline{\text{P}}$ANDA physics experiments is almost always customized, it is useful to stay with an industrial standard. The reason for this is the usage of the already developed and purchasable infrastructure like power supply, cooling devices, or interconnection between modules.

The ATCA standard [2] offers high bandwidth, which is different to the standards which were used in the past like VMEbus, FASTBUS, and CAMAC. The high bandwidth is an essential feature for the $\overline{\text{P}}$ANDA DAQ. Furthermore, an ATCA shelf offers a full-mesh backplane. This allows point to point interconnection from each board to each board via bi-directional links. The ATCA shelf has even more features like supporting special ports for network hubs, or shelf management via Intelligent Platform Management Interface (IPMI), allowing the control of the powering, the cooling and the control of each board individually.

5.1.2 The Compute Node (CN)

In a close collaboration of the trigger lab of the institute of high energy physics in Beijing, China and the II. Physikalisches Institut Gießen, the multi-purpose FPGA-based data processing platform CN was developed [44]. Beginning as a pure $\overline{\text{P}}$ANDA project, the development is now a synergy venture between the $\overline{\text{P}}$ANDA experiment and the Belle II experiment (an upgrade of the existing Belle experiment located at the high energy accelerator research organization (KEK) in Tsukuba, Japan). Using the CN as part of an upgrade of the zero degree detector of BES III is also under discussion.

After several iterations, the CN is now an ATCA [2] based carrier board [83], equipped with up to four single-height, full-size Advanced Mezzanine Cards (AMC) [1] in the extended Telecommunications Computing Architecture for physics standard (xTCA), called xTCA-based FPGA Processor (xFP) [93].

The carrier board itself is equipped with a Xilinx Virtex-4 FX60 FPGA [57] and provides the (inter-)connections between all xFP cards as well as the ATCA backplane. A picture as well as a schematical view is given in figure 5.1.

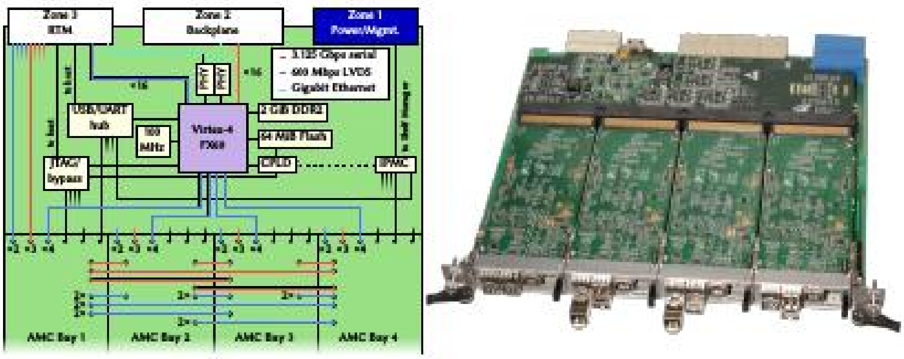

Figure 5.1: Right: picture of the ATCA based carrier card hosting four xFP cards, left: schematic of the CN. This figure is adapted from [59].

For more processing power, the FPGA of the xFP is a Xilinx Virtex-5 FX70T in an FFG1136 package [93]. More details on the

FPGA can be found in [9].

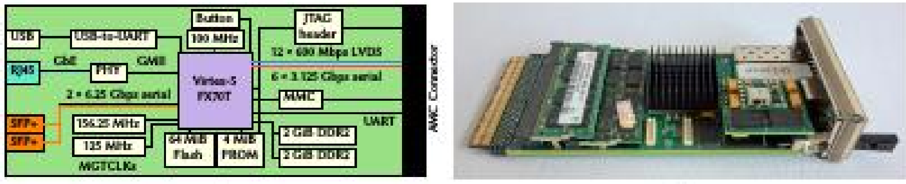

Figure 5.2: The xFP v4.0 AMC card. Left: Schematic view of the cards components. Right: Photograph of a card equipped with two DDR2 SO-DIMM modules. This figure is adapted from [59].

The xFP is designed with two RAM slots supporting up to 2 × 2 GB DDR2 RAM to store data until processing. It is also equipped with a non-volatile storage of 64MB of flash memory, four SFP+ cages for e.g. optical links with up to 6.25 Gb/s and one RJ45 gigabit Ethernet connector [93].

5.2 The $\overline{\text{P}}$ANDA Data Acquisition Concept

Most of the data during a run is created by direct light hadron production in anti-proton proton reactions. These events can be handled as backround. The total annihilation cross section of proton anti-proton reactions is several orders of magnitudes higher than the interesting cross sections, see figure 1.1.

In other experiments the data rate is reduced by a trigger using very simple requirements of the topology of the events. Unfortunately this is not possible at the $\overline{\text{P}}$ANDA experiment, due to the fact that the topology of many benchmark channels is looking just like the topology of the background channels. Therefore the events will be reconstructed and filtered online.

Furthermore, the DAQ is featuring another task: Since some of the sub–detector readout systems are slower than the eventrate of 20 MHz in average, there will be overlapping events. These events have to be disentangled in real time.

The trigger in other experiments has another purpose, which is synchronizing the readout. In $\overline{\text{P}}$ANDA this will be achieved by the socalled Synchronization Of Data Acquisition Network (SODANET) [47].

5.2.1 The Readout Scheme

The DAQ at the $\overline{\mathrm{P}}$ANDA experiment will be build of several building blocks to solve the described features of the trigger-less operation and no direct event structure. These building blocks are:

- Intelligent FEE
- SODANET and Data Concentrator (DC)
- Burst Building Network (BBN)
- Event Building Network (EBN)
- Event Filter Network (EFN)

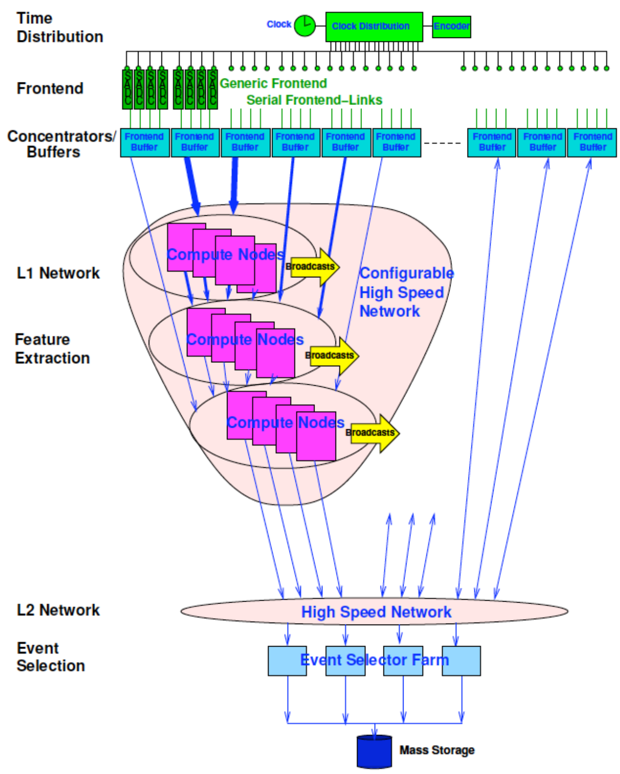

Figure 5.3: Simplified DAQ read-out scheme. A synchronization signal from a very precise clock (shown in light green) will be distributed to the autonomous FEE (shown in dark green). At the DC level (shown in light blue) the data from the FEE will be collected and clustered before it will be send to the L1 Network, which will include the BBN and EBN. The L1 and the L2 networks will supply interconnection between the CN (shown in pink) for efficient reconstruction of the events. At the event selection the data will be filtered before storing (shown in dark blue). The figure is taken from [4].

5.2.2 Intelligent FEE

To reduce the data in an efficient way, the reduction will be done starting at a very early stage. In $\overline{\text{P}}$ANDA intelligent FEE devices will be used, which will be autonomously able to detect hits and preprocess data.

One example is the sADC from Uppsala. It will be used at the $\overline{\text{P}}$ANDA EMC. This ADC is able to run in two different modes: the feature extraction mode and the pulse data mode. In case of the feature extraction mode the sADC is sending a hit package consisting of two data words per hit (compare figure 5.5). In this package only a timestamp, the channel number and the sum over all samples of the detected pulse is send. In contrast to this, in the pulse data mode, every sample of one hit will be send. The sADC is programmed in a way that it will use the feature extraction as a baseline mode. The pulse data mode will only be used in case of multiple hits during the read out, or if explicitly adjusted by the slow control.

5.2.3 SODANET & DC

The SODANET is structured in the following way: There is one source, which is sending the SODANET protocol to so-called SODANET hubs. The hubs distribute the protocol to the DC, as it is displayed in figure 5.4. The SODANET protocol is based on the TRBnet protocol. The TRBnet is described in [67].

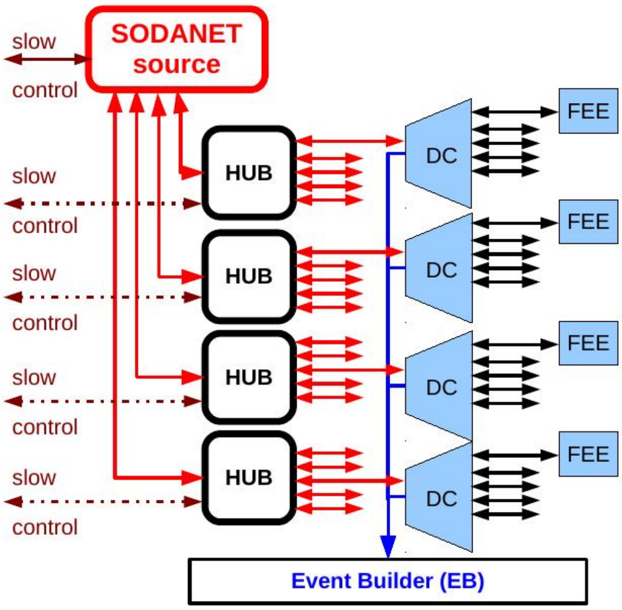

Figure 5.4: Simplified SODANET scheme[64]. The red lines indicate the bidirectional SODANET links. Each hub features the possibility for a second slow control connection, while slow control commands can be distributed via the SODANET link. Black lines indicate the bidirectional front-end-link, which is detector dependent. The blue lines indicate the data link, which is unidirectional. The EB includes the burst building network as well as the event building network.

There are two different types of SODANET commands, which can be distinguished by the highest bit:

1. Super-Burst-Command (SBC):
   - Super-burst start, eventually end of previous superburst
   - Bit 31 := '1'
   - Bits 30 - 0 := Super-Burst-Number (SBN)
2. Calibration command:
   - Bit 31 := '0'
   - Bit 30 := Time calibration
   - Bit 29 := DAQ start
   - Bit 28 := DAQ stop
   - Bit 27 := reset
   - Bits 26-8 := undefined
   - Bits 7-0 := CRC checksum (CRC8-CCITT)

At the beginning of each super-burst[1], the SBC is sent to each DC. Here the 16 bursts are counted. Furthermore, the DC checks the correct sequence of the SBNs and marks errors in the output format. A missing SBN is inserted at the DC from a local counter.

The commands are structured in 64-bit words, while data packages of 8-bits are alternating with a k-character.

K.27.7	data[31 -24]	K.27.7	data[23 - 16]	K.27.7	data[15 - 8]	K.27.7	data[7 -0]

After recieving a package, the DC feedbacks a 16-bit package to the SODANET hub or the source, respectively.

In case of a SBC:

K.27.7	bits 7-0 from the SBN

In case of a calibration command:

K.27.7	CRC checksum

Data from the DC is sent either via data link in case of a CN-based burst builder network, or via User Datagram Protocol (UDP) in case of a commercial switch based burst builder network. The data link is a basic 8bit/10bit encoded protocol, using K-characters as start- or end of frame and as idle character. Since the data format in the burst building network is based on 32 bit words, a special reciever from Simon Reiter, filtering out the idle characters and converting the data link to the local link interface is used in the CN-BBN.

Start of frame:	K.28.7
Idle:	K.28.5
End of frame:	K.28.6

An example of a data word in the data link format is:

[1] A super-burst is defined as 16 bursts, with a timeframe of $(2 + 0.4)\ \mu s$ each.

K.28.5	K.28.7	data[31 -24]	data[23 - 16]	K.28.5
data[15 - 8]	K.28.5	data[7 -0]	K.28.6	K.28.5

The idle characters inbetween the words are due to the fact that the DC starts to send data as soon as data arrives from the FEE. At the DAQ/FEE meeting in 2013 in Alba, Italy the $\overline{\text{P}}$ANDA data format was decided. It is shown on the left in figure 5.5. So far only the EMC has adapted this format.

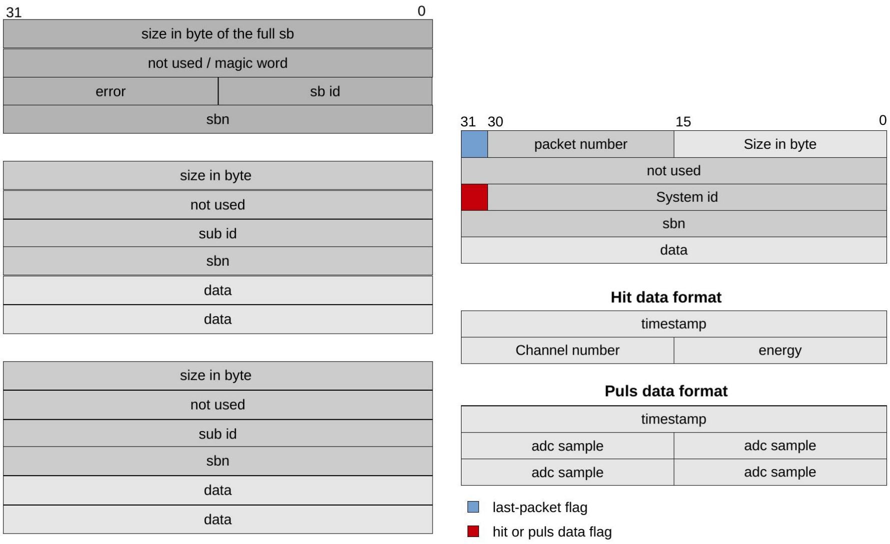

Figure 5.5: Left: General $\overline{\text{P}}$ANDA data format. Right: EMC data structure, for either hit data (ADC in feature extraction mode) or pulse data (used in case of pile up).

As a DC a Xilinx Kintex ultrascale based board designed by Pawel Marciniewski from Uppsala, Sweden is foreseen. A schematical view of this board is displayed in figure 5.6. The DC provides point-to-point communication, buffering and online data manipulation.

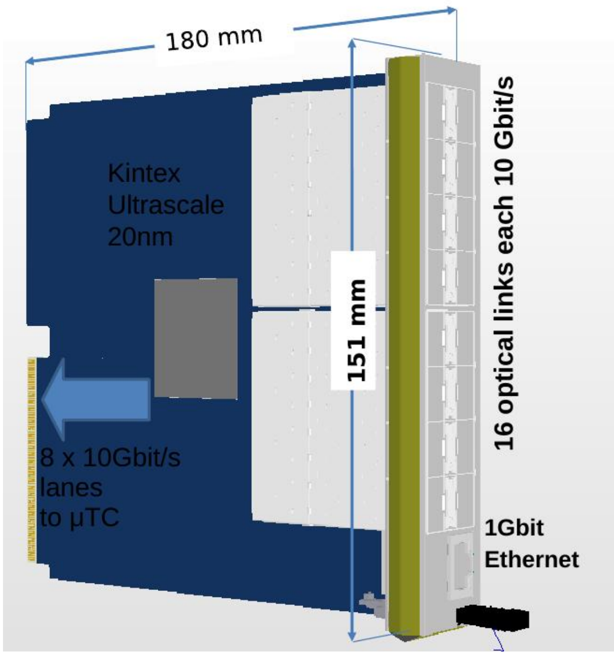

Figure 5.6: Schematical view of the FPGA based DC board[65], featuring a Xilinx Kintex ultrascale FPGA, 16 10 Gbit/s optical transceivers and 1 GbitEthernet. Furthermore, 8 10 Gbit/s lanes will be connected to the μTCA backplane. It will have a μTCA formfactor.

5.2.4 BBN & EBN

At the $\overline{\text{P}}$ANDA experiment an avarage event rate of 20 MHz will be achieved, which is equivalent to one event per 50 ns. The drift-time in one straw is approximately 200 ns, so that there will be overlapping event structures. In figure 5.7 the event time (first hit in the STT) vs the time stamps of a Monte Carlo (MC) simulation is plotted [3].

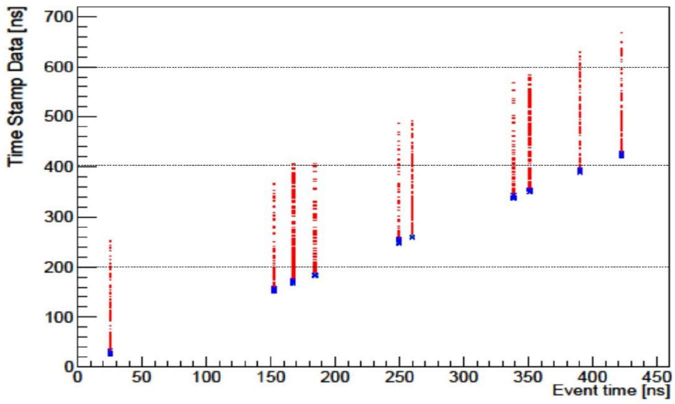

Figure 5.7: 2 dimensional plot of the timing structure of events in the STT. The first hit-time of an event is marked with a blue cross, while red dots indicate the individual time-stamp of one straw. The figure is taken from [3].

In contrast to a MC simulation, only the time-stamp will be available in real data. This shows how difficult an event-building at the $\overline{\text{P}}$ANDA experiment will be. An event-like structure is achieved by implementing a small gap of 400 ns every 2 μs called bursts into the anti-proton beam. The DC will merge 16 of these bursts including 16 gaps to a super burst. The BBN will merge the super bursts from the DCs to a full super burst of either a subdetector or the full detector and distribute them to the event building network. Depending on the kind of BBN even more functionalities could be available at this stage.

Two different kind of BBNs are under discussion:

1. A BBN constructed of commercial switches
2. A FPGA based system

A BBN constructed of commercial switches has the advantage that it will be easily set up. But on the other hand one looses the possibility of preprocessing and partial reconstruction of the data. As part of this thesis the PTDAQ was build as the first FPGA based BBN.

The task of the EBN is to reconstruct, disentangle and filter the events. It is not decided on which kind of processing platform the EBN will run. Most likely it will be a mix of everything, depending on the performance. Under discussion is a coarse online FPGA based reconstruction in a first step and more fine online reconstruction on a PC farm. Till now it was shown that tracking algorithms can be performed on FPGAs and on GPUs. Furthermore, a cluster finding algorithm was developed for FPGAs. A second type of cluster finding algorithm as well as a PID algorithm are under development.

5.2.5 EFN

The EFN will perform a coarse online analysis to reduce the data by using:

- Combinatorics
- Mass Window Selection
- Filter Specific Selection
  - Event Tagging

17 channels, shown in table 5.1, using 57 tagger modes are analyzed so far. The filter channels will run in parallel and use a logic OR. This allows to analyse several data channels in parallel. Nevertheless, it reduces the tagging efficiencies[2], due to cross tagging as it is indicated in figure 5.8.

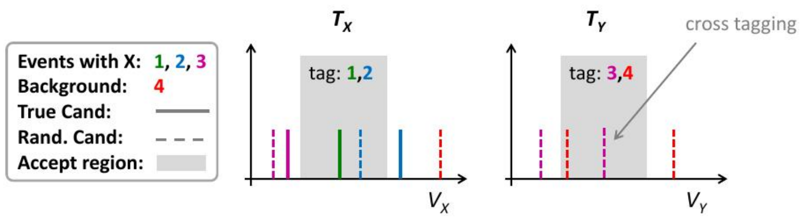

Figure 5.8: An example for cross tagging is: Take two different tagger channels T_X and T_Y, while the final state of T_X is included in T_Y, like $D_0 \rightarrow K\pi$ and $\lambda_c \rightarrow pK\pi$. Event type 3 is a random candidate of channel T_X in the channel T_Y. However it is tagged due to the logic OR. Due to this less events are rejected. The figure is taken from [50]

[2]Efficiency is the number of correctly tagged events divided by all tagged events.

Trigger #	Resonace	Channels (BR[%])	# of tagger
1	η_c	$K^+K^-\pi^0$ (1.2), $K_SK^\pm\pi^\mp$ (2.4), $K^+K^-\pi^+\pi^-\pi^0$ (3.5), $\gamma\gamma$ $K_SK^\pm\pi^+\pi^-\pi^\mp$ (1.8)	5
2	J/ψ	e^+e^-(5.9), $\mu^+\mu^-$ (5.9)	2
3	χ_{c0}	$\pi^+\pi^-K^+K^-$ (1.8), $K^\pm\pi^\mp K_S\pi^0$ (0.8)	2
4	D_0	$K^-\pi^+$ (3.9), $K^-\pi^+\pi^0$ (13.9), $K^-2\pi^+\pi^-$ (8.1), $K_S\pi^+\pi^-\pi^0$ (3.7), $K_S\pi^+\pi^-$ (2.0)	5
5	D^+	$K^-2\pi^+$ (9.4), $K^-2\pi^+\pi^0$ (6.1), $K_S2\pi^+\pi^-$ (2.1), $K_S\pi^+\pi^0$ (4.8)	4
6	D_s^+	$K^+K^-\pi^\pm$ (5.5), $K^+K^-\pi^\pm\pi^0$ (5.6)	2
7	D_0^*	$D_0\pi^0$ (61.9), $D_0\gamma$ (38.1)	10
8	D^{*+}	$D_0\pi^+$ (67.7), $D^+\pi^0$ (30.7)	9
9	D_s^{*+}	$D_s^+\gamma$ (94.2)	2
10	λ	$p\pi^-$ (63.9)	1
11	λ_c^+	$pK^\mp\pi^\pm$ (5.0), $pK^\mp\pi^\pm\pi^0$ (3.4), $pK_S\pi^0$ (1.2)	3
12	Σ^+	$p\pi^0$ (51.6)	1
13	ϕ	K^+K^- (48.9)	1
14	e^+e^-+X	X = none / γ / π^0	3
15	$\mu^+\mu^-+X$	X = none / γ / π^0	3
17	$\gamma\pi^0$		1

Table 5.1: List of foreseen trigger channels, taken from [50]. K_s is decaying into $\pi^+\pi^-$ and π^0 into $\gamma\gamma$.

These filter channels allow to analyze approximately 800 different data channels, depending on the E_{cm}, in charmonium-, open charm-, and baryon spectroscopy. The investigations on the filter are still ongoing and require precise simulations.

Chapter 6

Prototype Trigger-Less Data Acquisition (PTDAQ)

To study the $\overline{\text{P}}$ANDA DAQ, a first prototype system was developed within the framework of this thesis: the prototype trigger-less data acquisition. It is a system based on FPGAs designed to have "intelligence" in an early stage, which means the possibility to run algorithms online.

6.1 System Architecture

Starting with one xFP board[1] in a μTCA shelf, the PTDAQ is a scalable system leading to the final DAQ for the $\overline{\text{P}}$ANDA experiment. In a starting scenario the shelf only supplies power and cooling. By extending the system to more xFP boards, depending on the μTCA shelf, more features of the shelf infrastructure can be used, e.g. an interconnection via the shelf-backplane is possible by using the backplane ports of the xFP board. The μTCA standard does not provide star topology on the backplane, therefore a customized shelf is under investigation. An option closer to the final $\overline{\text{P}}$ANDA DAQ would be to use the ATCA based CN as it is displayed in figure 6.1. The CN would allow the interconnection between up to four xFPs. By using the FPGA on the carrier card, in addition to the backplane connectivity of an ATCA shelf, large systems can be realized.

[1] more informations about the hardware in section 5.1.2

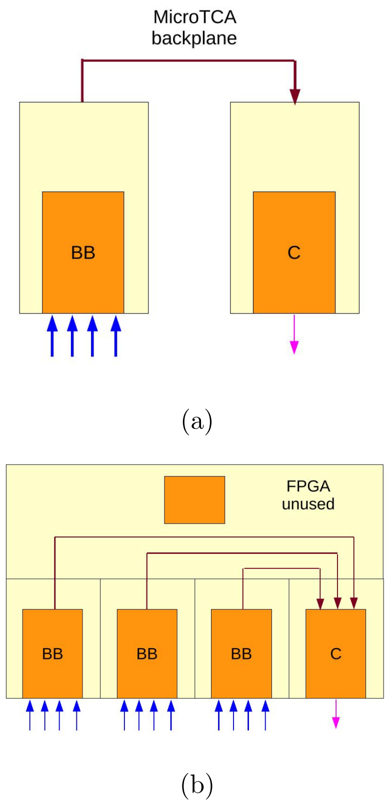

Figure 6.1: (a) Dataflow for an extension of the PTDAQ using two xFP boards in a μTCA shelf. One xFP is used as an converter (C). (b) Dataflow for an extension of the PTDAQ using the connection in the internal backplane of the CN. This allows a connection of up to 12 DCs.

The main task of the PTDAQ is the burst- or event building during detector prototype tests. For this, freely streaming data from FEE is collected and synchronized via SODANET at DC level, and finally is received at the PTDAQ. A schematic view of the data flow is shown in figure 6.2. Furthermore, the PTDAQ features low-level online filtering. Examples of low-level filtering are coincidences of different detector devices or special geometrics based on channel numbers. In addition the filter can be used to reject the empty packages.

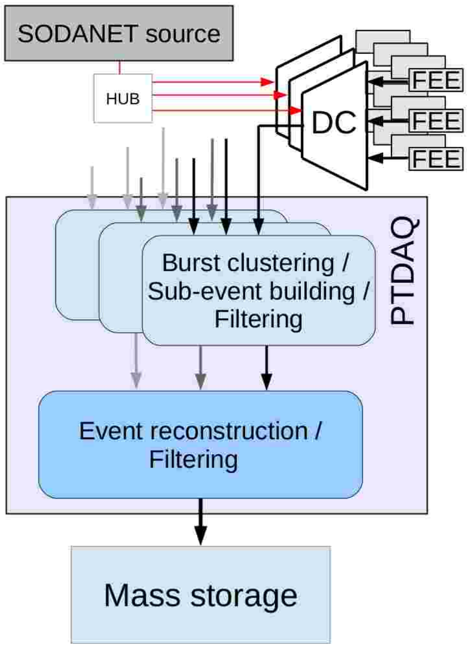

Figure 6.2: Simplified PTDAQ read-out scheme.

6.2 Burst Building Algorithm

The basic firmware of the PTDAQ implements the burst building algorithm. It has two inputs and one output and clusters these two different data streams according to their SBN[2]. Input number one is preferred (compare figure 6.3). Per definition, each DC is sending a data frame per SBN. To be as fast as possible, the incoming data is processed as soon as there is a SBN at each input. Nevertheless it is possible that one input is sending with a short time delay, thus the data is buffered at the input. By now this buffer is only in the block RAM. In principle the xFP would allow large buffers of up to 4 GB, which would require special buffer management as it was used e.g. in the Online Selection Nodes (ONSEN) of the Belle II DAQ system [59].

If one input fails sending data or the time difference is too large in a way that the buffer runs full, the algorithm sends data of the remaining input and marks an error in the header of the output frame.

[2]for more information about the data format, see section 5.2.3

Furthermore it recalculates the size of the new frame and adds a new header, consisting of four 32 bit words (size, not used, error and id, and the SBN). Till now the id of the burst builder has to be choosen before synthesizing. In a later version of the PTDAQ the id should be adjustable via the slow control. To simplify the analysis of the data the burst builder also sends two trailer words, which will not be used in the later $\overline{\text{P}}$ANDA data format.

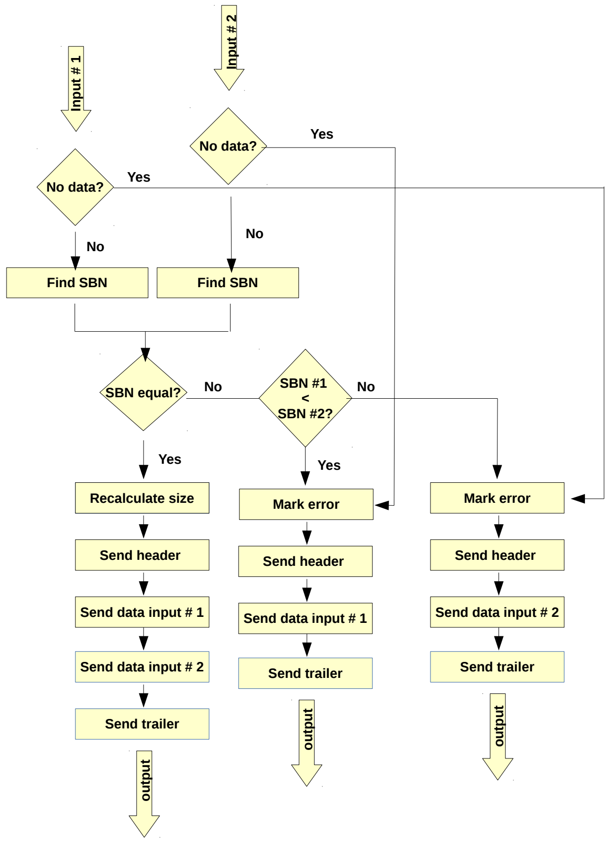

Figure 6.3: Flowchart of the burst building algorithm.

This algorithm also has a second functionality, which has to be choosen before synthesizing. In this case it also sorts the incoming data according to the SBN and recalculates the size, but does not add header and trailer. This feature can be used to enlarge the number of inputs of the system as shown schematically in figure 6.4. Due to the hardware layout of the xFP card a multiple input[3]

[3]more than two inputs

burst building requires a second xFP. To have the possibility of four inputs, a connection via the backplane between both cards is necessary. In this case an interconnection could be the Aurora protocol from Xilinx, for more information see [59].

As all firmware parts which are used in the PTDAQ, the burst building algorithm firmware uses a Local Link (LL) interface at the in- and output. The LL is described in the appendix A.

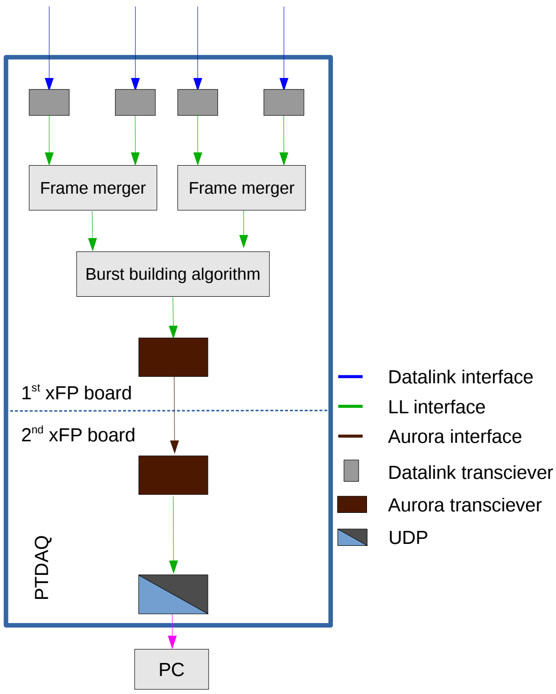

Figure 6.4: Schematical example for a multiple input use. By using xFP only for four as well as for three inputs a second xFP is required.

6.3 Other Firmware related to the PTDAQ

6.3.1 Filter Firmware

The filter firmware can be used either at an input or at an output of the burst builder. It has various features. Basically one can filter on a full 32 bit string. Furthermore it is possible to select specific bits out of the 32 bits. This allows to filter on a specific part of the data word, for example a channel number in the EMC data format is placed at the upper 2 bytes in the data word. Instead of filtering on an exact value one is able to filter on smaller or greater than the adjusted value. This can be used to filter out empty events by filtering on the minimal size of an empty package[4].

To avoid searching in the header or to filter on one particular word in the frame, one is able to skip some data words before starting to search on the specific filter. For instance, the rejecting of empty packages is performed by filtering on bigger than the minimal size of an empty package.

A full description of the filter firmware can be found in [80].

6.3.2 Transport Layer Protocols

The standard interface of the PTDAQ is the data link: The connection between the DCs and the PTDAQ is a simple 8b/10b encoded protocol using basic k-characters, as described in section 5.2.3. This link is using a 100 MHz clock, which allows a 1 Gbit/s input. The interconnection between the third version of the Trigger and Readout Board (TRBv3) and the xFP limits the input bandwidth. The xFP uses a 156.25 MHz clock for the MGTs and the TRBv3 uses a 200 MHz clock. As a MGT clock an internally generated clock of 100 MHz was used in both cases. This allows 1 Gbit/s as the highest possible data rate.

The maximum bandwidth from PTDAQ to PC is limited to 1 Gbit/s.

For an interconnection from xFP to PC an UDP implementation from Greg Korcyl [53] is used. A description of the usage of the IP core is shown in the appendix A.

[4]An empty package in the $\overline{\text{P}}$ANDA data format has at least four header words.

Chapter 7

The PTDAQ Online Test

In November 2015 an in-beam environment test was performed at the Mainzer Microtron (MAMI) using the PTDAQ and SODANET during a test of the electromagnetic calorimeter prototype Proto120. A second detector was read out, the Glasgow Tagging Photon Spectrometer. 48 crystals from the Proto120 and 16 channels of the Glasgow Photon Tagging Spectrometer distributed of its full energy range were read out. A data set of several million events was collected after stabilizing the DAQ chain.

In the following, a short introduction of the detector as well as the accelerator is given before a detailed explanation of the test procedure and the taken data is analyzed.

7.1 Mainzer Microtron

The accelerator consists of five stations. Supplied by a source, 100 keV electrons are accelerated in an injector Linear Accelerator (LINAC) up to 3.97 MeV. Afterwards, a cascade of three Race Track Microtrons (RTMs) increases their energy up to 855 MeV. Finally, the Harmonic Double Sided Microtron (HDSM) is able to accelerate the electrons to an energy up to 1.5 GeV [7]. A schematical view of the facility is displayed in figure 7.1.

7.1.1 The Glasgow Photon Tagging Spectrometer

The Glasgow Photon Tagging Spectrometer consists of 353 overlapping scintillating plastic detectors, each 24 mm wide and 2 mm

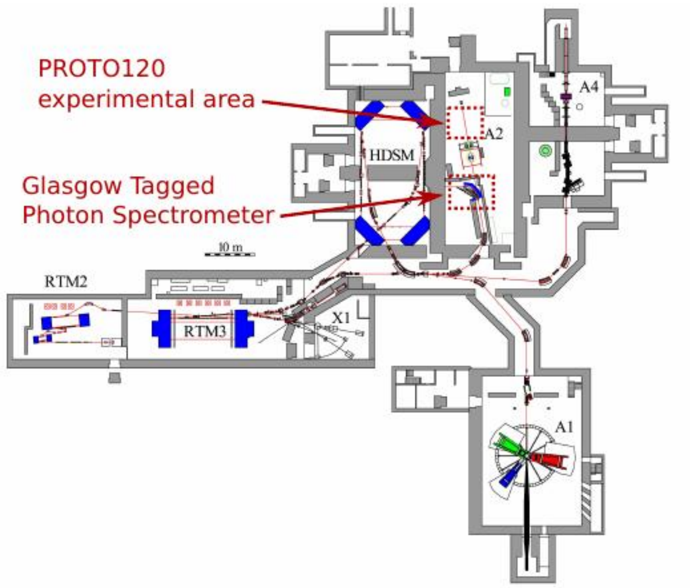

Figure 7.1: Schematical view of the mainzer microtron facility, showing the experimental areas X1, A1, A2 and A4 as well as the race track microtrons (RTMs) and the Harmonic Double Sided Microtron (HDSM) [7]. Furthermore, the location of the emc prototype PROTO120 and the Glasgow Tagging Photon Spectrometer are marked in red.

thick, read out via PMTs [66]. A basic scheme is shown in figure 7.2. At the MAMI facility, electrons are accelerated and produce bremsstrahlung photons in a radiator made of copper or diamond, which results in a continuous photon beam. Using a dipole magnet with a field of $B = 1.8T$ [66], the electrons are bent towards the focal plane. By measuring the impact position of the electron, its momentum p_e after iradiation of the bremsstrahlung photons can be calculated via the Lorentz force with the known curvature R.

$$p_e = R \cdot q \cdot B \tag{7.1}$$

Since the initial energy of the electron E_0 is known and the energy of the tagged electron is calculated, the energy of the photon E_γ is determined by:

$$E_\gamma = E_0 - E_e \tag{7.2}$$

In this case choosing coincidences with a set of plastic scintillators leads to well defined photon energy beams. The energy of the photons selected in the test is given in table 7.1.

Channel Number	Photon Energy [MeV]
15	766.76 ± 1.70
14	743.92 ± 1.72
13	681.17 ± 2.04
12	641.73 ± 2.12
11	599.91 ± 2.26
10	462.34 ± 2.64
9	438.13 ± 2.65
8	406.30 ± 2.72
7	376.65 ± 2.75
6	238.40 ± 2.78
5	191.58 ± 2.84
4	159.78 ± 2.86
3	128.20 ± 2.86
2	104.08 ± 2.83
1	80.12 ± 2.79
0	56.36 ± 2.74

Table 7.1: Relation between tagger channel and photon energy.

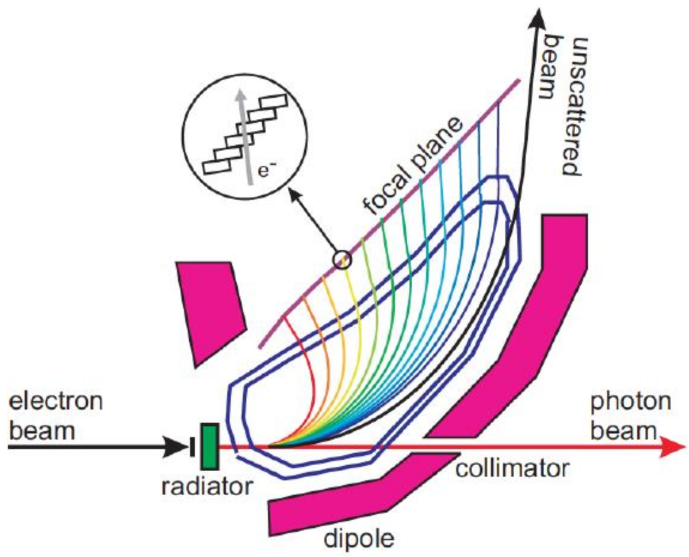

Figure 7.2: Schematic view of the Glasgow Photon Tagging Spectrometer[8].

7.1.2 The Electromagnetic Calorimeter Prototype

The barrel EMC of the $\overline{\text{P}}$ANDA detector will be divided into 16 slices. Each slice will have 11 slightly different shaped PWO crystals, depending on their position in the slice. The prototype EMC (Proto120) consists of three blocks of each 40 crystals of type 1, 2 and 3 arranged in 10 columns and 4 rows [38], shown schematically in figure 7.3.

This prototype is very close to the final barrel EMC using the almost final electronics and mechanical components. Just like the final EMC, the Proto120 is separated into a cold and a warm volume. The cold one is at $-25°C$ and includes the crytals and parts of the readout electronics [38].

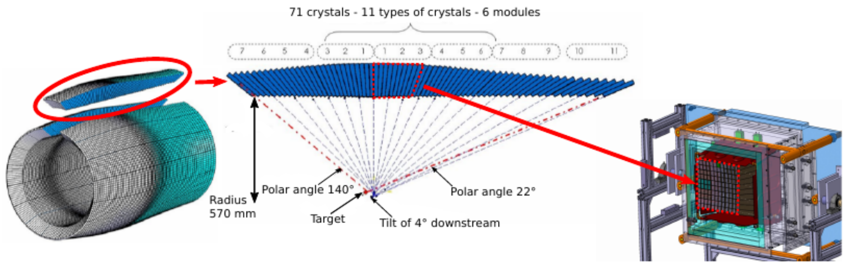

Figure 7.3: Schematic view of the Barrel EMC with an indication of which subsection out of a barrel slice the Proto120 consists of[38].

Each crystal is read out via two 1 cm^2 rectangular LAAPDs [39], while these are read out by one customized APFEL ASIC [90]. The two channels are independent and consist of a charge sensitive preamplifier, a third order semi-Gaussian shaper stage and a differential output driver, as shown schematically in figure 7.4.

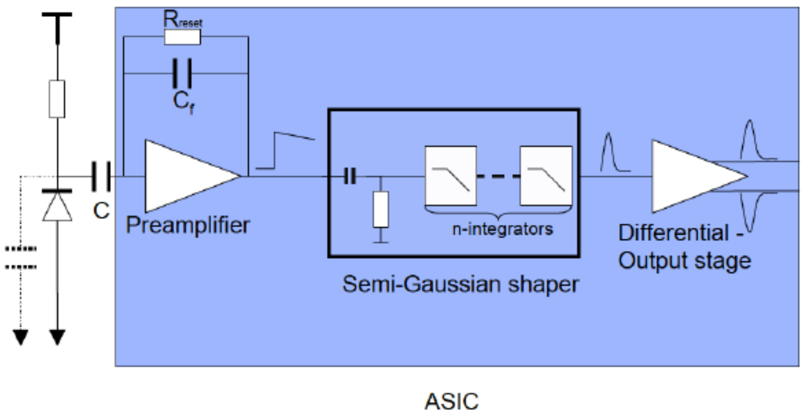

Figure 7.4: Schematic view of the APFEL ASIC[81].

The APFEL ASIC is placed in the cold volume to reduce the electronic noise. Four flex cables connect APFEL ASICs to a Printed Circuit Board (PCB) backplane to overcome the distance between the cold and the warm volume [38]. The PCBs are designed to guide the signal as well as the supply of low and high voltages. The differential signal is guided via a driver PCB buffer board, which is connected with two PCB sto the sampling ADC, as shown in figure 7.5.

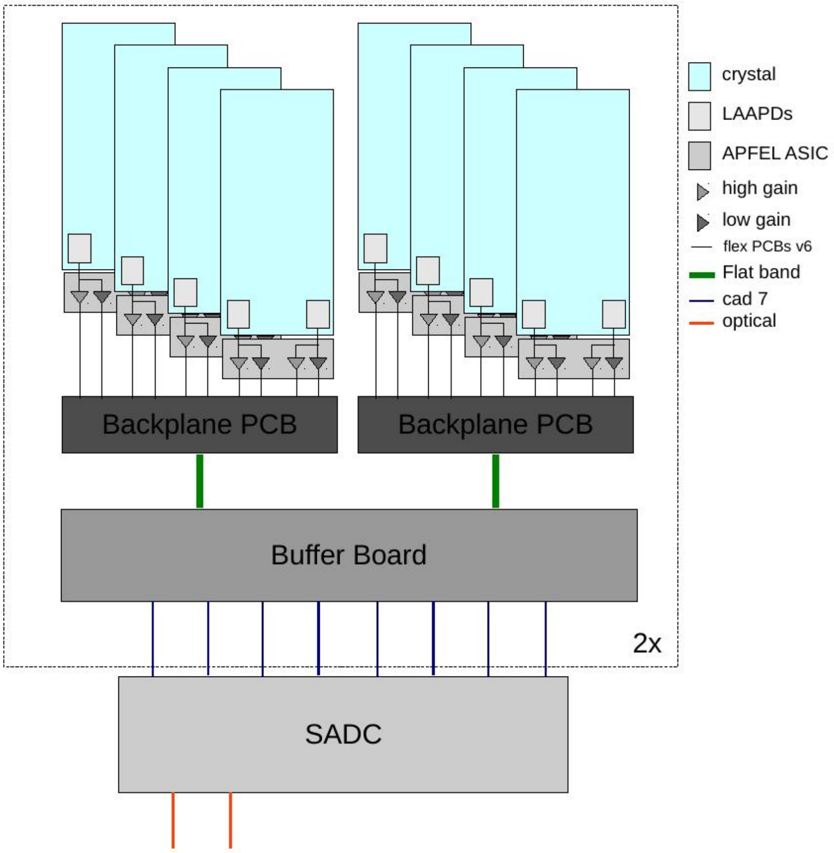

Figure 7.5: Schematic of the Proto120 read-out plan. For simplification, only 8 crystals are drawn, even though 16 can be connected to one ADC.

Conventional DAQ of the Proto120

The inner part of this DAQ chain up to the PCB buffer boards is identical to the readout scheme using the PTDAQ. The rest of the conventional DAQ of the Proto120 is different and uses a 50 MHz, 16 bit sampling ADC (SIS 3302). It is a triggered DAQ using a logic AND between the tagger signal and the ADC signal. For the coincidence circuit of the tagger and the ADC standard NIM and CAMAC modules are used, as shown in figure 7.6.

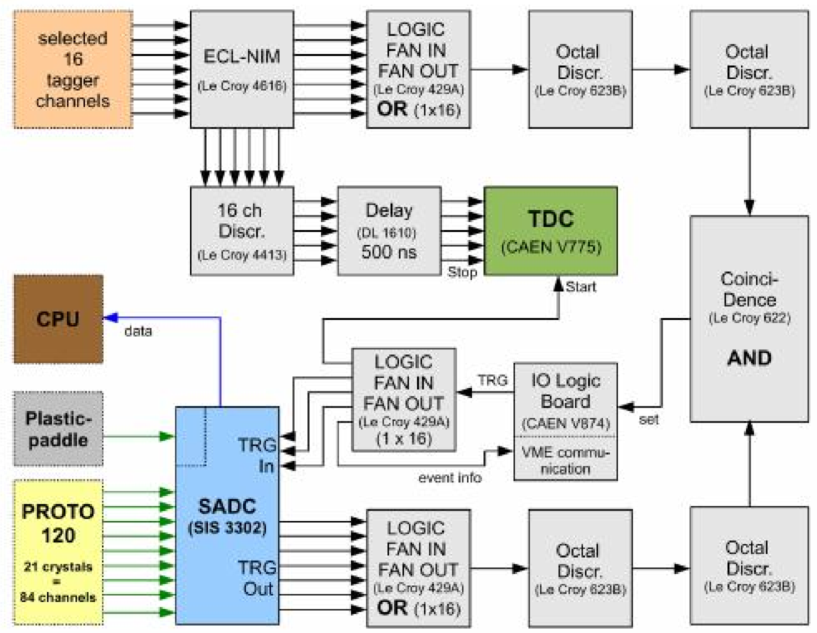

Figure 7.6: Conventional DAQ scheme of the Proto120[38].

7.2 Beam Time Procedure

During this in-beam test, two different types of crystals were used: "normal" fully polished crystals and crystals which had one sided depolished. A crystal matrix is displayed in figure 7.7. In total, 48 crystals of the Proto120 and 16 channels of the Glasgow Photon Tagging Spectrometer were read out. Therefore, four customized sampling ADCs were used as front-end electronic devices. In addition, two data concentrators and a SODANET source were used. Before the description of the data analysis, the hardware components will be circumstantiated. A picture of the setup at MAMI is shown in figure 7.10.

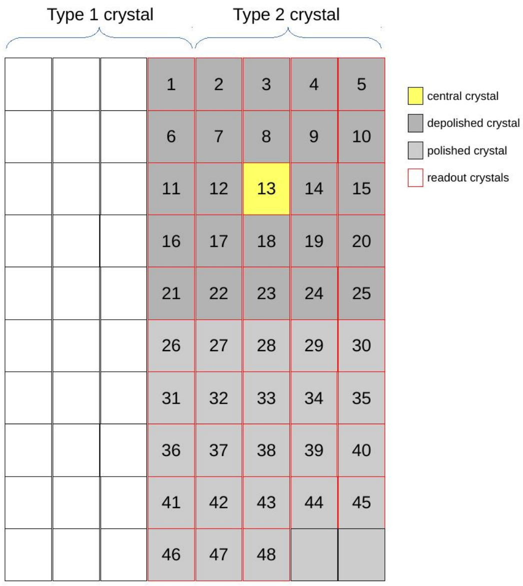

Figure 7.7: Schematic of the cystal matrix used in the in-beam enviroment test. 48 crystals were read out in total, the yellow one indicates the crystal where the beam was focused.

Sampling ADC

The sampling ADC was designed by our colleagues from Uppsala, Sweden [51]. It is a FPGA based board featuring two Xilinx Virtex-6 FPGAs, two optical outputs and 64 input channels [51]. Four channels are used per crystal directly, in case of transferring a differential signal of low and high gain from both LAAPDs. For this purpose, a special adapter was build in Gießen together with the electronic workshop. The layout can be found in the attached chapter B. An adapter build in Gronigen, Netherlands allows single-ended readout, which was used to read out the Glasgow Photon Tagging Spectrometer.

The ADC has a sampling rate of 80 MS/s and a resolution of 14 bit [51] and is shown in figure 7.8.

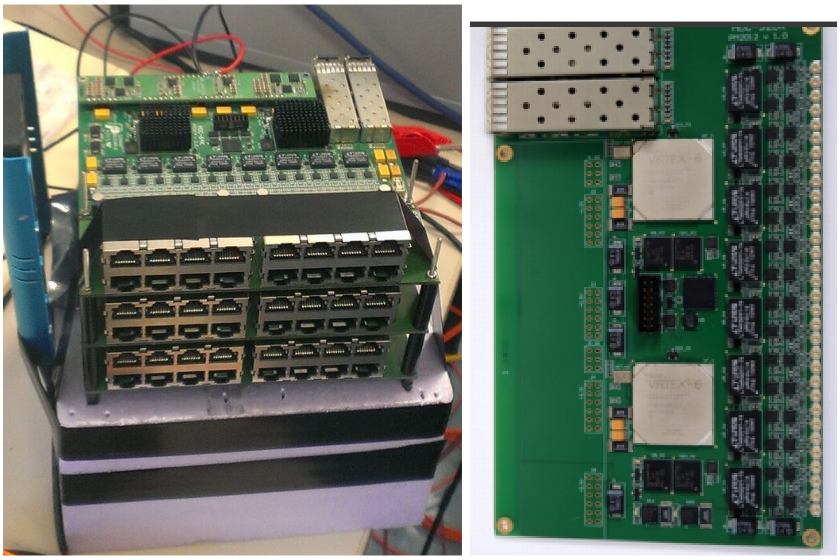

Figure 7.8: Left: Photograph of three stacked sADCs equipped with the connector build in Gießen. Right: Picture of the sADC from Uppsala.

Trigger and Readout Board Version 3

The TRBv3 [87], shown in figure 7.9, was originally designed for the High Acceptance Di-Electron Spectrometer (HADES) detector. It is used as an interim solution for the SODANET platform. It is a multi-purpose FPGA based board featuring 5 Lattice ECP3-150EA FPGAs [87]. Using extensions via AddOn-boards, up to 32×3.2 Gbit$/s$ optical transceivers are available.

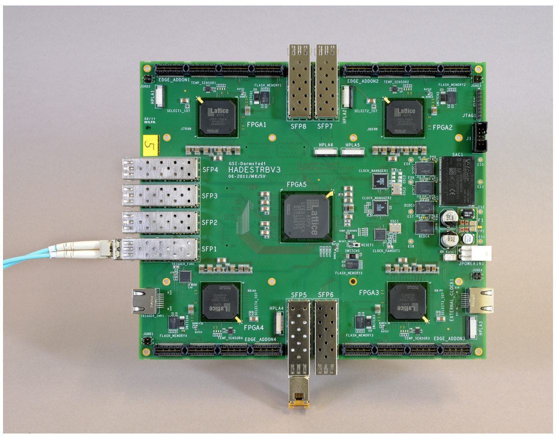

Figure 7.9: Photo of a pure TRBv3 without any AddOn-boards[87].

During the test 2 of these boards were used. On one TRBv3 a SODANET source and one DC were implemented on peripheral

FPGAs, while on the other one a peripheral FPGA was used as a DC.

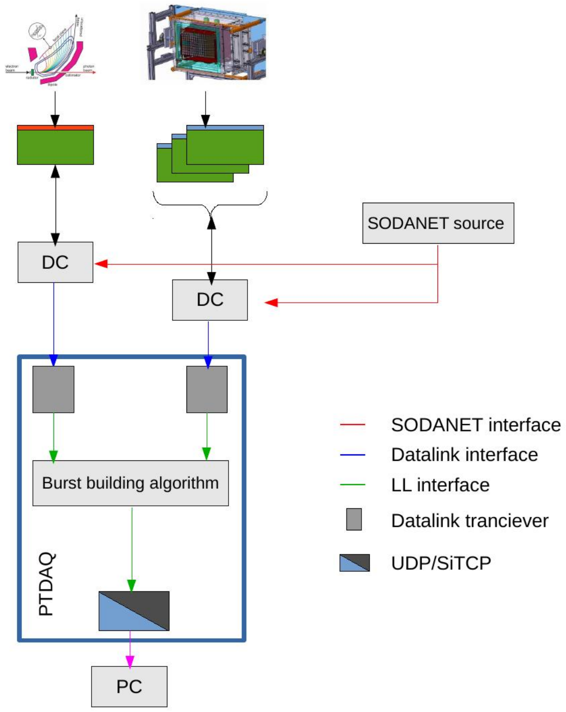

(a)

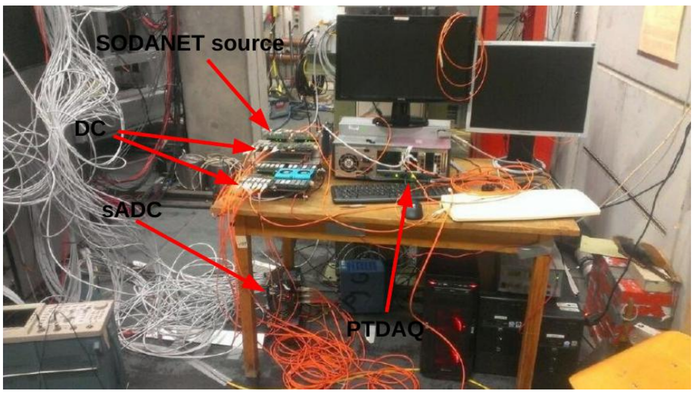

(b)

Figure 7.10: (a) Schematical data flow including internal firmware components of the PTDAQ. (b) Picture of the setup at the MAMI in-beam environment test. It shows 2 trigger and readout boards version 3 (TRBv3) used as SODANET source and as Data Concentrator (DC), as well as the sADC and the PTDAQ. On the left hand side the Proto120 can be recognized.

7.3 Analysis of the collected Data

This test was a proof of principle of the full $\overline{\text{P}}$ANDA DAQ chain procedure. Data was taken and 88,500,500 bursts were successfully build. In the following a description of the data analysis is given.

7.3.1 SODANET Error

As mentioned before, a DC has to send a package to each SBN eventhough there is no data coming from the sADC. If this is not the case, one has two possibilities: either one of the DCs is not sending data (one-sided), or both (two-sided). To check one-sided SODANET errors, the marked error in the data format is analyzed, and as a redundancy check one can verify if the new size is smaller than the minimal size of the empty package. In 2751 of the bursts, one-sided SODANET errors were found, which correpondes to 0.003% of all bursts.

In case of two-sided SODANET errors, checking size and marked errors is not sufficient. For this purpose missing SBNs were analysed and no two-sided SODANET error was found.

7.3.2 Burst Building Error

To check if an error in the burst building algorithm has happened during data taking, a comparison of the SBNs in the bursts was performed. Furthermore the data format was scanned for the magic words in header and trailer. Overall no burst building errors were found in the recorded data.

7.3.3 Performance test of the PTDAQ

To test the performance of the PTDAQ, the energy distribution of the central crystal was analyzed. To reduce the background, a cut on the coincidence between the tagger and the central crystal was used.

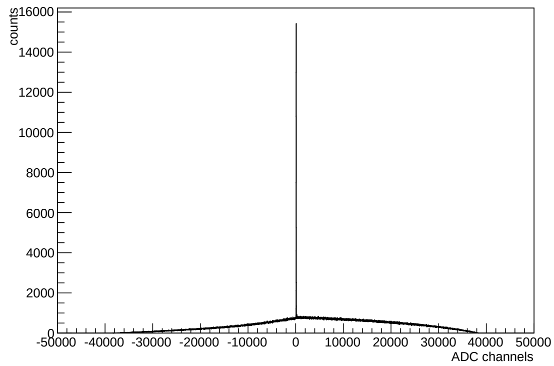

Figure 7.11: Distribution of Δt between all taggers and the central crystal.

Furthermore, the background under the peak was substracted. In figure 7.12 the Δt between the tagger channels and the central crystal, after the background rejection, is displayed.

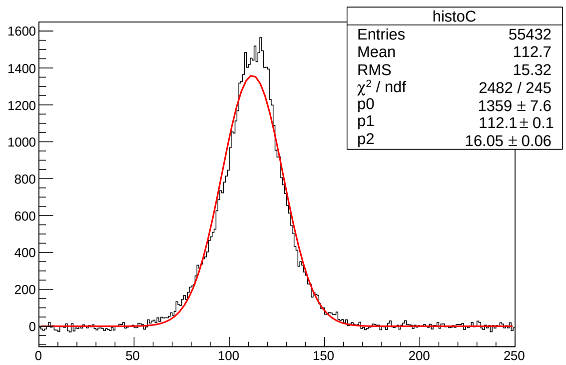

(a)

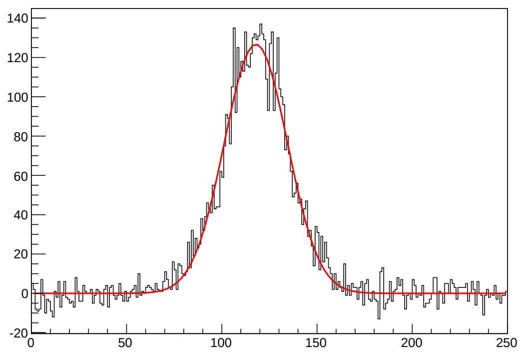

(b)

Figure 7.12: (a) Distribution of Δt between all taggers and the central crystal with substracted background. (b) Distribution for tagger number 1.

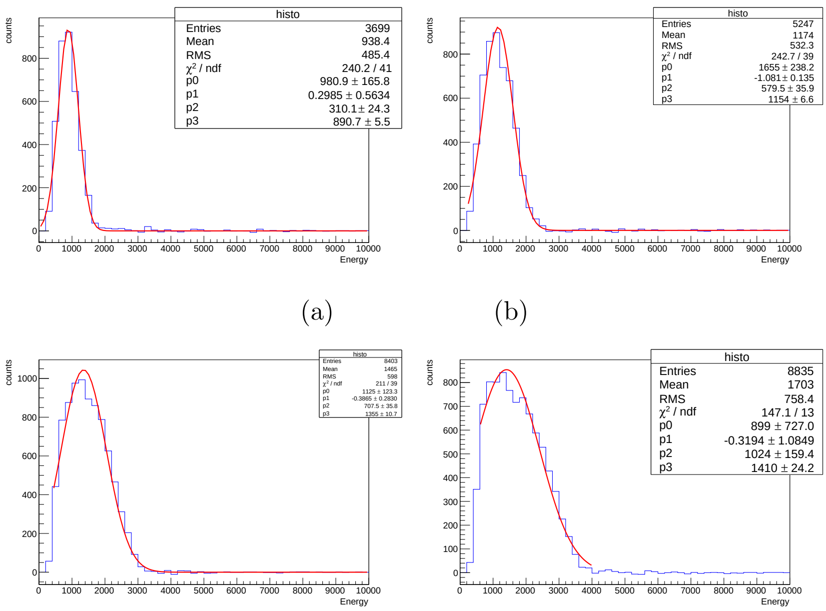

(a) (b)

(c) (d)

Figure 7.13: The figures (a) - (d) show the energy distribution of the central crystal for different tagger channels. (a) corresponds 56.36 ± 2.74 , (b) 80.12 ± 2.79, (c) to 104.08 ± 2.83, and (d) to 128.20 ± 2.86.

Unfortunately during the test the detector was misaligned, which explains the bad resolution of the energy distributions of energies above 100 MeV. Nevertheless, the energy rises linearly, as shown in figure 7.14.

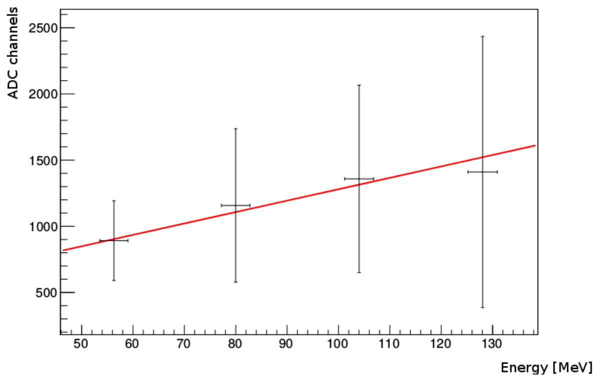

Figure 7.14: Energy versus ADC channels showing a linear behaviour. The broad resolution is due to the fact that the detector was misaligned.

This concludes that the performance of the PTDAQ is sufficient to be used as a DAQ for detector prototype tests.

Chapter 8

Analysis of $h_c \to p\bar{p}$

Within the frame of this thesis a new upper limit of the cross section $p\bar{p} \to h_c$ was determined by using the ansatz of detailed balance, which allows to calculate the cross section back from the measured partial width of the decay $h_c \to p\bar{p}$. For this purpose a data set of $(447.9 \pm 2.8) \cdot 10^6$ $\psi(2S)$-events from the BES III experiment was analyzed [15].

In this chapter a detailed description of this analysis will be given. Starting with the event selection criteria, which lead to the reconstruction efficiency, via a comparison with a former analysis to the systematic uncertainty evaluations, and finally an explanation of the calculation of the upper limit is given. Furthermore an interpretation of the impact of this value for the $\overline{P}ANDA$ experiment is discussed.

8.1 Motivation

As the $\overline{\text{P}}$ANDA collaboration wants to investigate the hadron physics in the charmonium region, precise simulations of specific channels – benchmark channels – are required. For this purpose, the knowledge of production cross sections of proton anti-proton to charmonia is essential. Unfortunately only a few cross sections are measured yet, therefore investigations of the unknown production cross sections are necessary. By producing charmonium states in electron–positron–collisions and analysing their partial decay width into proton anti-proton pairs, the production cross section can be calculated by using the method of detailed balance.

One very interesting charmonium state is h_c with a mass of $3525.38 \pm 0.11\ MeV/c^2$ [73], which is below the $D\bar{D}$-threshold. Although most charmonia below this threshold are studied quite extensively, we only know about 52% [73] of its decays. With its quantum numbers $J^{PC} = 1^{+-}$, it can not be produced directly in electron-positron-collisions. To analyse the partial widths of the h_c one has to attain it as a decay product of higher lying charmonium states. In this thesis I used the decay $\psi(2S) \rightarrow h_c \pi^0$.

Various theoretical calculations predict very different partial widths for the h_c decaying into proton and anti-proton. For example, calculations using helicity selection rules of pertubative QCD predicted a suppression on the decay $h_c \rightarrow p\bar{p}$ [33]. By comparing the allowed decay $\chi_c(1) \rightarrow p\bar{p}$ with its partial width of
$\mathcal{B}(\chi_c(1) \rightarrow p\bar{p}) = (7.72 \pm 0.35) \cdot 10^5$, the branching ratio should be significantly smaller [73]. Nevertheless, other theories like effective Lagrangian methods estimate much larger partial widths in the order of 10^{-3} [62].

Furthermore there is a prediction from Francesco Murgia using QCD models including constituent quark mass corrections [69].

$$2.1 \cdot 10^{-5} \geq \mathcal{B}(h_c \rightarrow p\bar{p}) \geq 1.0 \cdot 10^{-5}$$

This is smaller than the current upper limit, which is smaller than $1.5 \cdot 10^{-4}$ at 90% confidence level [73], determined by the BES III experiment in the year 2012 [17]. This analysis used $106.8 \cdot (1.00 + 0.70\%) \cdot 10^6$ $\psi(2S)$ decay [17] events, while now more than 4 times the amout of $\psi(2S)$ decays is available, which maybe allows to reach this limit.

Futhermore, the E835 experiment at Fermi National Accelerator Laboratory, USA [21], measured the partial width to be $10 \pm 3.5 < \Gamma(p\bar{p} \to h_c) \cdot \mathcal{B}h_c \to \eta_c\gamma) \leq 12 \pm 4.5eV$. Using the total width of the h_c, this value corresponds to a branching ratio range of $1.8 \cdot 10^{-5} < \mathcal{B}h_c \to p\bar{p}) \leq 4.6 \cdot 10^{-5}$. Even though this limit is below the upper limit measured at the BES III experiment, the particle data group "does not use the following data for averages, fits, limits, etc" [73].

8.2 Event Selection Criteria & Efficiency Extraction

In order to obtain the signal reconstruction efficiency (ϵ) I used a Monte Carlo simulation of the signal decay chain

$$e^+e^- \to \psi(2S) \to h_c\pi^0 \to p\bar{p}\gamma\gamma$$

of 10000 events and in addition an inclusive $\psi(2S)$ Monte Carlo simulation provided by the BES III collaboration.

The event selection of the decay is realized in three steps. First a reconstruction of two charged tracks using MDC informations and two neutral particles using the EMC and a missing signal in the MDC is done. Afterwards I used a kinematical fit constrained by energy and momentum conservation and in addition constraining the mass of π^0. This fit is called 5C-fit, according to its five constrains. Afterwards, a figure of merit is calculated to get the best ratio of background suppression by keeping the highest possible reconstruction efficiency.

The selection criteria results in an efficiency of $\epsilon = (31.2 \pm 1.0 \pm 7.7)\%$. The systematic uncertainties will be described in section 8.5 and the statistical error σ_s is calculated:

$$\sigma_s = \frac{1}{\sqrt{N}} = 1\ \% \tag{8.1}$$

Here N is the number of events in the MC sample. It should be mentioned that these values include the acceptance of the detector.

How these cuts are reducing the efficiency is displayed in table 8.1 and will be described in the following sections.

Cut	Number of Events in MC
total number	10000
2 charged particles	8918
$N_\gamma > 2$	6019
Pass 5C fit	4121
figure of merit cut	3118

Table 8.1: The cut flow of selection criteria, showing the reduction of each step and the final efficiency $\epsilon = (31.2 \pm 1.0 \pm 7.7)\%$.

Charged Tracks

In addition to the basic requirement of two charged tracks with a net charge of zero, a cut on the decay vertex was applied.

- Exactly two charged tracks and a net charge of zero
- Vertex cut
  - z direction: $\Delta z < 20\ cm$
  - xy plane: $\Delta xy < 2\ cm$

Particle Identification

For each charged track a hypothesis is calculated in a way that the track is either created by a pion, a kaon or a proton. For this, information from the ToF and the energy loss of the particle in the MDC is used. The particle hypothesis with the largest probability is assigned to the track. In this analysis two charged tracks are required.

Neutral Particles

The π^0 decays to two photons in $(98.823 \pm 0.034)\%$ [73] of all cases. A minimum of two photons is demanded, since in each event background photons can be created. To distinguish the photons from background photons, some basic requirements are needed.

- For background and noise suppression the energy deposited of the photon E_γ has to be higher than a certain value:
  - $E_\gamma > 25$ MeV if $|\cos\Theta| < 0.8$ (barrel region)
  - $E_\gamma > 50$ MeV if $0.86 < |\cos\Theta| < 0.92$ (endcap region)
- To reduce the bremsstrahlungs contamination:
  - Angle between photon and a positive charged track larger than $10°$

  - Angle between photon and a negative charged track larger than 30°, the stricter cut is to exclude photons from the anti-proton annihilation.

- A minium of 2 photon candidates is required

π^0 Reconstruction

To assure a correct reconstruction of the π^0 via the correct two photons, a kinematical fit constraining the initial four momentum and the mass of the π^0 was used. This fit is calculating a χ^2 for each photon combination by taking the four momenta of the proton and anti-proton into account. The combination with the smallest χ^2 is chosen to be the event.

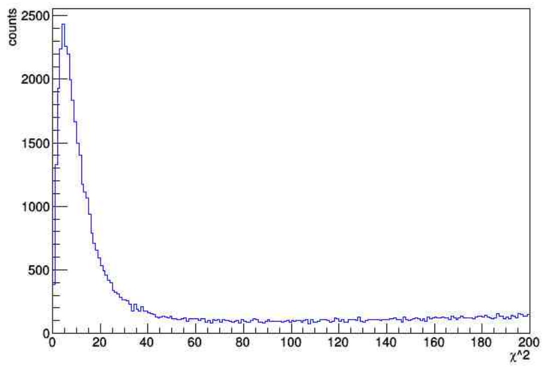

Figure 8.1: χ^2 distribution of the 5C-fit of the data.

The invariant mass of the π^0 after the 5C-fit is a delta function. To have the possibility to see the resonance in the spectrum, the non-fitted data was stored separately before the 5C-fit.

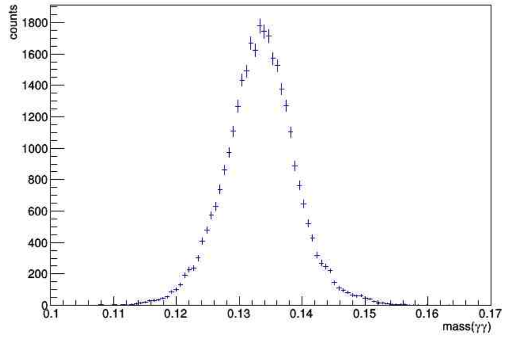

Figure 8.2: The invariant mass distribution of two photons of the data, with a clear peak at the mass of the π^0.

Figure of Merit

To obtain the best cut value for the χ^2-distribution of the 5C-fit, a figure of merit ($\mathcal{F}$) was calculated as part of this thesis. The best ratio of signal (N_S) to square root of signal plus background N_{S+B} was taken.

$$\mathcal{F} = \frac{N_S}{\sqrt{N_{S+B}}} \tag{8.2}$$

The ratio is calculated for bins with a width of 5. The best ratio was determined at $\chi^2 = 30$, visualized with a red dotted line in figure 8.3.

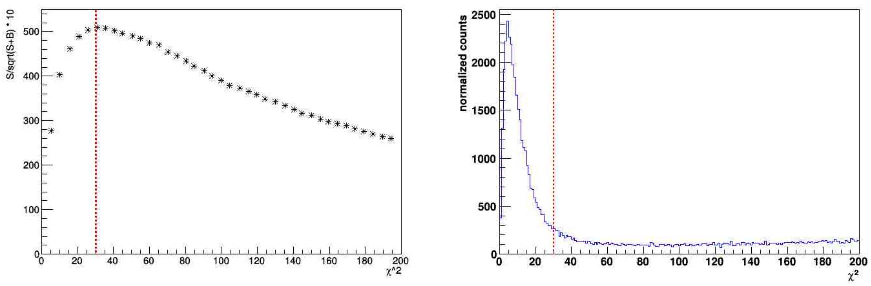

Figure 8.3: Left: Distribution of the figure of merit depending on the 5C-fit-χ^2. For better visualization a mulplication with a factor 10 was applied. Right: The χ^2 distribution. The dashed red line indicates the best value, resulting in a cut.

The extracted values as well as the corresponding plots can be looked up in the attachment D.

8.3 Comparison with former BES III Analysis

The analysis of $\psi(2S) \to h_c\pi^0$, $h_c \to p\bar{p}$ was done in 2012 with a data set of $106.8 \cdot (1.00 + 0.70\%) \cdot 10^6$ $\psi(2S)$ events. It is published in [17]. The analysis procedure was a bit different in this analysis, since the decay of $h_c \to p\bar{p}$ was just one part of several $c\bar{c} \to p\bar{p}$. To compare the former analysis with my analysis, I analyzed the smaller data set from 2009. As one is able to see in figure 8.4, the invariant mass distribution from the former analysis is almost as it is in this work.

The invariant mass distribution of proton and anti-proton is fitted using a Gaussian distribution for the signal and an Argus function to describe the dominant background. The Argus function allows to fit a background with a precise cutoff at one side; in this analysis it is defined by the difference between the mass of the initial particle $\psi(2S)$ and the mass of the π^0. In the former analysis the Gaussian was allowed to have a negative yield, to cover the possibility of destructive interference. Since the significance is only 1.9 σ of such a destructive interference, a negative yield of the Gaussian distribution will not be allowed in the analysis of the full data set.

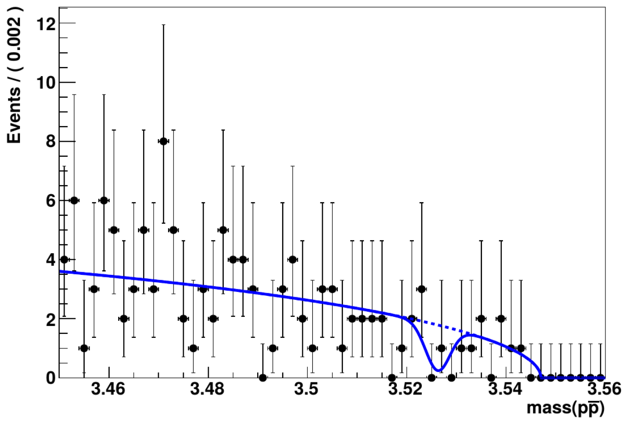

(a)

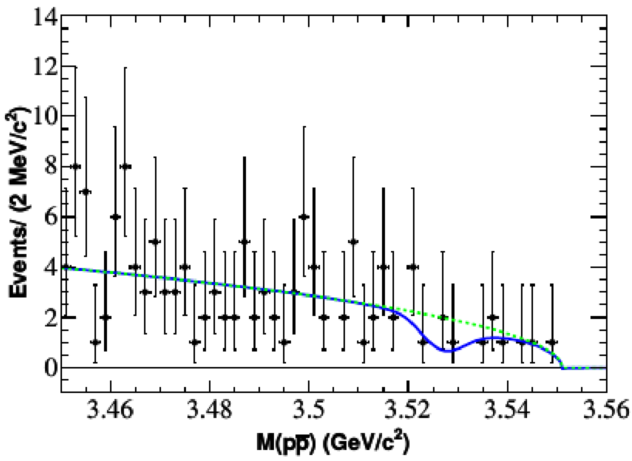

(b)

Figure 8.4: (a) Invariant mass distribution of proton and anti-proton using my analysis. The spectrum is fitted with an Argus function representing the background and a Gaussian for the signal. (b) The distribution from the former analysis, using almost the same fit function.

8.4 The Full Data Set

Even by using the full data set, no evidence of a positive signal yield was found, so that a partial width measurement was not possible. In figure 8.5 the data is also fitted with an Argus function for the background and a Gaussian for the signal. The abscence of a signal results in a new upper limit extraction, discussed in the following sections.

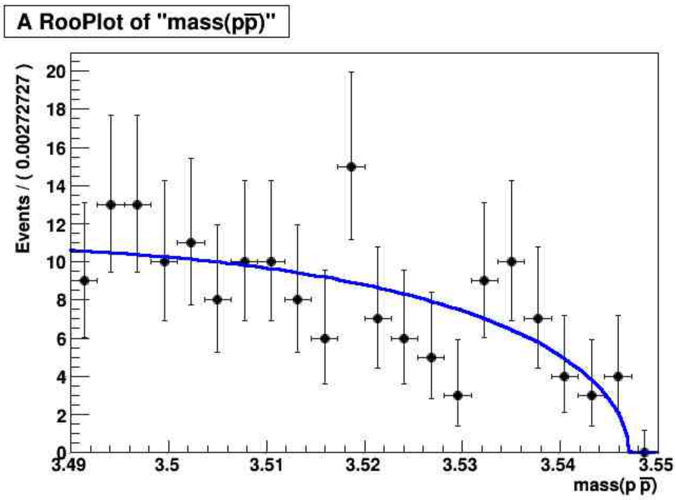

Figure 8.5: Invariant mass distribution of proton and anti-proton fitted with an Argus as a background function and a Gaussian as a signal. The blue line represents the combined fit-function. Since there is no signal yield of the Gaussian, an upper limit extraction is required.

8.5 Systematic Uncertainties

In the calculation of the upper limit the total systematic uncertainty σ is taken into account by a factor $(1-\sigma)$. The total error is calculated as the square root of the sum over the squared uncertainties x_i, given in equation 8.3.

$$\sigma = \sqrt{\sum_i x_i^2} \tag{8.3}$$

While an overview of the systematic uncertainties is listed in table 8.2, a precise description of each error is given in the following subsections.

source	uncertainties [%]
tracking efficiency	2.0
difference in $\vec{p}$	2.5
photon efficiency	2.0
Total number of $\psi(2S)$	0.6
Particle ID	2.0
Kinematic Fit	2.0
π^0 Selection	3.0
Fitting Range	5.2
sum	7.7

Table 8.2: List of all systematic uncertainties, as well as the final sum. The efficiency error includes the error from the fit as well as the statistical one.

8.5.1 Tracking Efficiency

The decay $J/\psi \to p\bar{p}\pi^+\pi^-$ was used by the data quality group [41] to study the tracking efficiency for proton and anti-proton. For this purpose, the difference of the transverse momentum (p_t) between the MC and the data was analyzed. As displayed in figure 8.6 the difference for $p_T \geq 0.3$ GeV/c is very small.

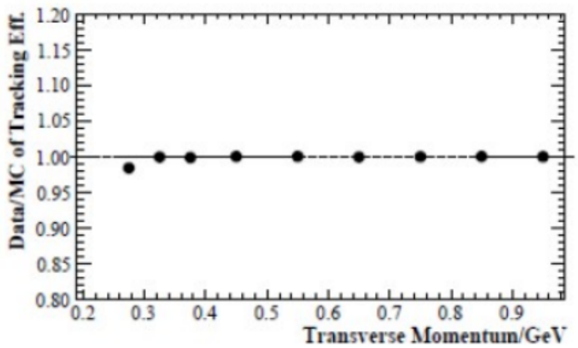

(a)

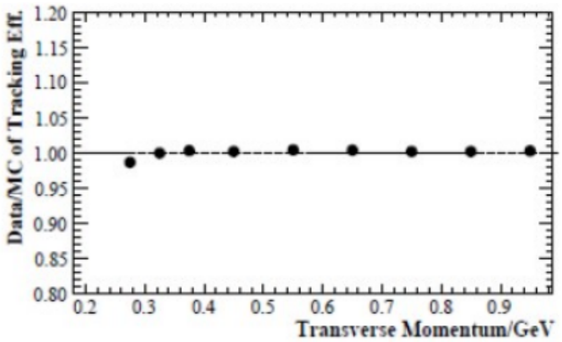

(b)

Figure 8.6: The difference between the data and the MC in tracking efficiency dependent on the transverse momentum, (a) for protons and (b) for anti-protons, taken from the analysis $J/\psi \to p\bar{p}\pi^+\pi^-$ [41].

The transverse momentum of proton and anti-proton shown in figure 8.7 is almost always larger than 0.3 GeV/c. Thus the systematic uncertainty of the tracking efficiency taken to account is 1.0% per track.

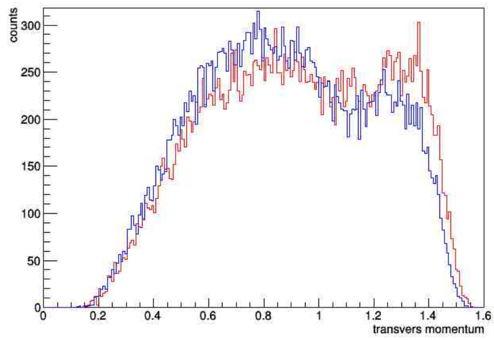

Figure 8.7: Transverse momentum distribution of the protons (blue) and anti-protons (red). The difference in the distributions is due to the different photon cut, see appendix C.

8.5.2 Photon Efficiency

The systematic uncertainty of the efficiency to detect a photon is measured by the quality group [40] in the decay of $J/\psi \rightarrow \rho^0\pi^0$, $\rho^0 \rightarrow \pi^+\pi^-$ and $\pi^0 \rightarrow \gamma\gamma$. As it is shown in figure 8.8, the uncertainty is 1%.

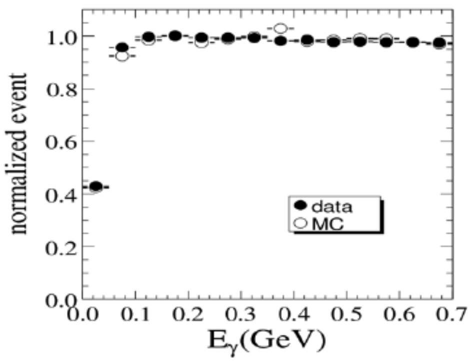

(a)

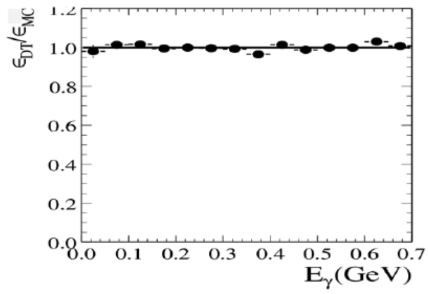

(b)

Figure 8.8: Systematic uncertainties for photon efficiency [40]. (a) Photon efficiency of MC as well as data. (b) Difference between MC and data.

8.5.3 Number of $\psi(2S)$

As each measurement, the total number of $447.9 \cdot 10^6 \psi(2S)$ also has an uncertainty. As given in the publication [15], the error is measured to be 0.61%.

8.5.4 Particle ID of the Proton/Anti-Proton

The difference between a Monte Carlo and the data analysis of the decay $J/\psi \to p\bar{p}\pi^+\pi^-$ was used to determine the uncertainty of the identification of protons or respectively anti-protons [17].

As shown in figure 8.9 the variety for high momentum protons is quite small.

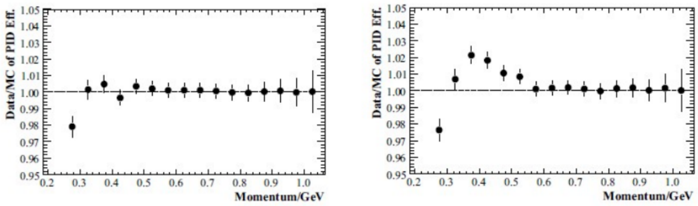

Figure 8.9: The systematic uncertainty for PID along with momentum [17], (a) for protons and (b) for anti-protons.

In figure 8.10 the momentum of the anti-protons (red) and the protons (blue) is displayed. Both momentum distributions are for almost 95% above 0.6 GeV/c. A systematic uncertainty of 2.0% in total is assumed.

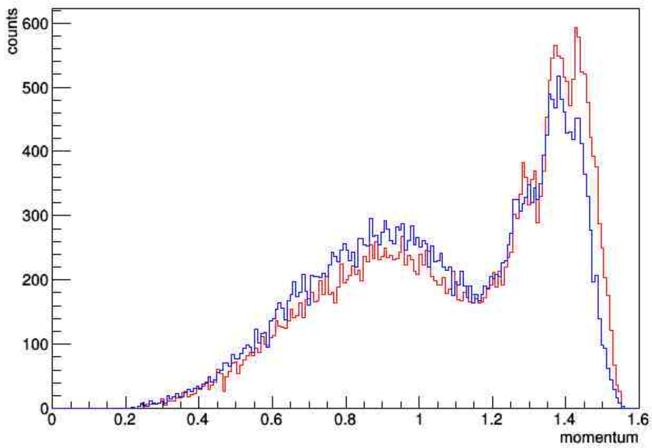

Figure 8.10: Momentum distribution of protons (blue) and anti-protons (red).

8.5.5 Momentum distribution of protons and anti-protons

The momentum distribution of protons and anti-protons shown in figure 8.10 differs, due to the different photon angle cut (compare appendix C). Due to this, the difference between the momentum distributions of the protons in the inclusive Monte Carlo and the data analysis is shown in figure 8.11. The maximum difference is taken as the systematic uncertainty, in case of protons 0.5 % and in case of anti-protons 1.5 %.

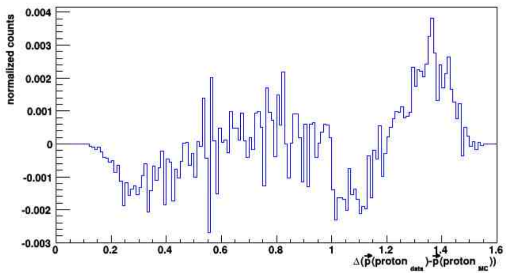

(a)

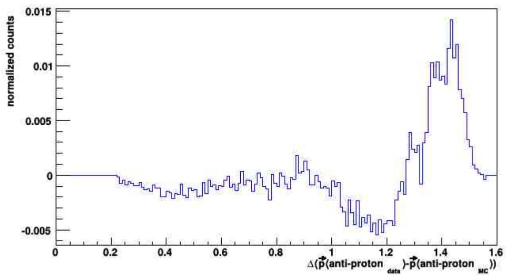

(b)

Figure 8.11: The differences in the momentum distribution of the data and the inclusive MC, for protons (a) and anti-protons (b).

In addition the differences between the momentum distribution of protons and anti-protons in the data, drawn in figure 8.12, is taken into account. The systematic uncertainty is 2 %.

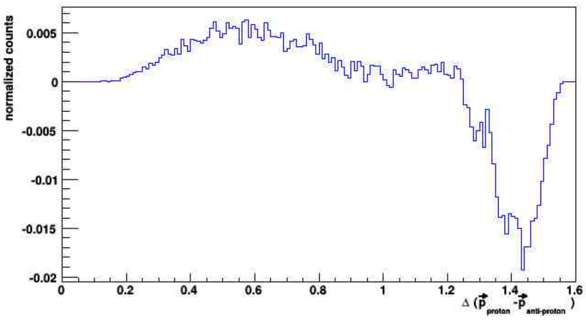

(b)

Figure 8.12: The differences of the momentum distribution of protons and anti-protons.

8.5.6 Kinematic Fit

To get the systematic uncertainty of the kinematic fit, an inclusive Monte Carlo was analyzed. The size of the MC sample is about four fifths of events of the data set itself. In figure 8.13 the χ^2-distributions of the kinematical fits are shown. Since the data sample of inclusive MC is a bit smaller than the real amount of data, a scaling factor of 0.8 is used to display both in one histogram. The systematic uncertainty of 3% is derived by taking the maximum difference of the distributions.

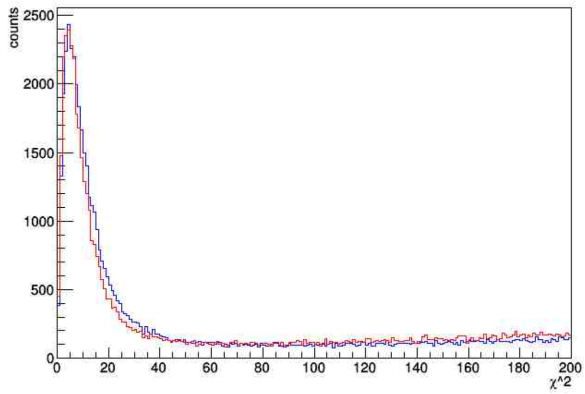

Figure 8.13: Comparison of the χ^2-distributions of the inclusive MC (in red) and real data (in blue). A scaling factor of 0.8 is used on the real data.

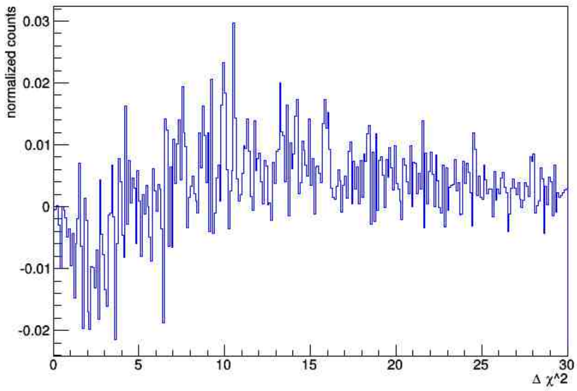

Figure 8.14: Differences of the χ^2-distributions normalized to 1. The maximum difference is used as a systematic uncertainty of 3%.

8.5.7 π^0 Selection

By studying the decay $\psi(2S) \to \pi^0\pi^0 J/\psi, J/\psi \to l^+l^-$, the efficiency of the π^0 was determined [14]. In this analysis J/ψ and the high momentum π^0 were tagged and the efficiency was resolved by analysing the missing π^0 in the recoil. The systematic uncertainty is obtained by the difference between the MC and the data, shown in figure 8.15. For the π^0 selection in this analysis, 3% is taken as the systematic uncertainty.

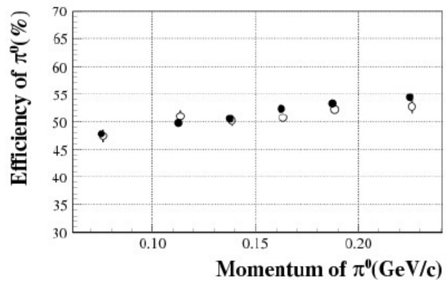

(a)

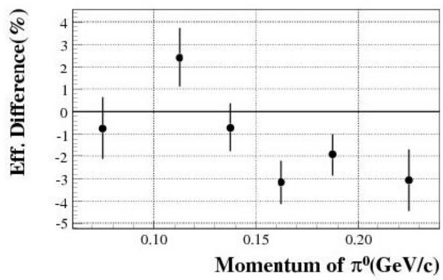

(b)

Figure 8.15: (a) π^0 efficiency in the data (dot) and MC simulation (circle) and (b) the relative difference of π^0 efficiency between the data and the MC simulation [14].

8.5.8 Fitting Range

For the fitting range variation, an enlargement of 10% in each direction was applied to determine the uncertainty. The difference of the yield extraction is used as a total systematic error of 5.2%.

8.6 Upper Limit of the Partial Width of $h_c \to p\bar{p}$ Calculation

To calculate the upper limit of the partial width for this decay, an unbinned-logarithmic-likelihood-fit of the invariant mass spectrum of proton anti-proton was performed, see figure 8.5. Furthermore a profile for the logarithmic likelihood distribution of the entries in the Gaussian was calculated. A projection of this profile is displayed in figure 8.16 and the extracted values are listed in table E.1.

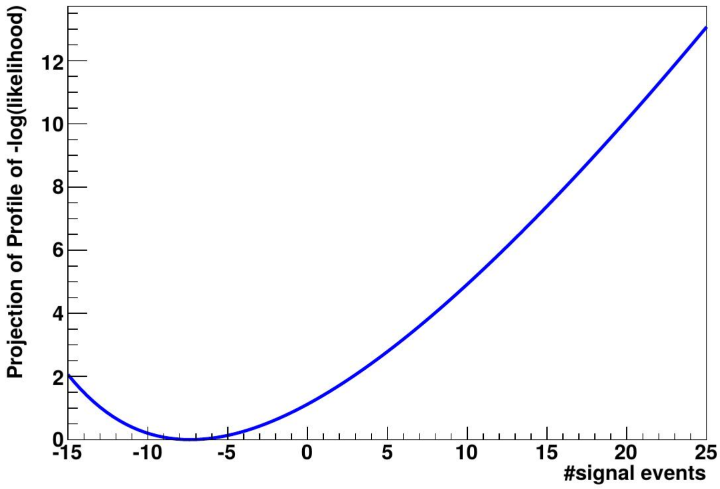

Figure 8.16: Projection of the logarithmic likelihood profile for entries in the signal yield.

From this, the likelihood only for positive entries was calculated and plotted in figure 8.17. By normalizing the integral, a 90 % Confidence Level (C.L.) was recieved, which leads to an upper limit N_{up} of 6.2 $h_c \to p\bar{p}$ events.

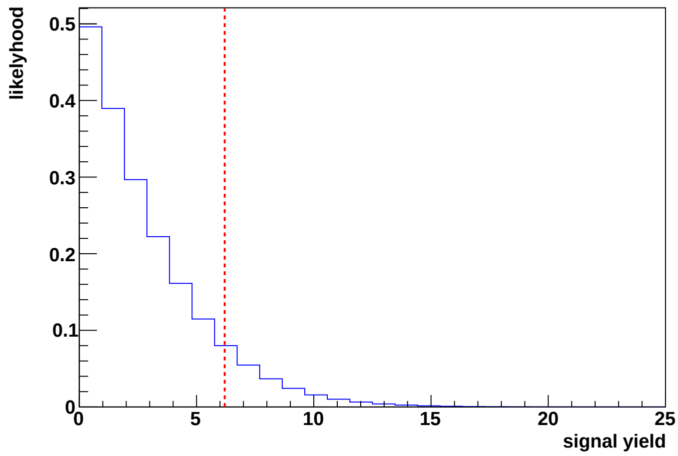

Figure 8.17: The normalized likelihood versus the number of entries in the yield of the Gaussian. Dashed red line indicates the upper limit of the number of signals at 90% C.L.

By using $N_{up} = 6.2$, the upper limit of the combined branching ratio of $\mathcal{B}(\psi(2S) \to \pi^0 h_c) \times \mathcal{B}(h_c \to p\bar{p})$ can be calculated.

$$\mathcal{B}(\psi(2S) \to \pi^0 h_c) \times \mathcal{B}(h_c \to p\bar{p}) < \frac{N_{up}}{N_{total} \cdot \epsilon \cdot (1 - \sigma)} \tag{8.4}$$

Here N_{total} is the total number of $\psi(2S)$ decays, ϵ is the efficiency and σ is the total systematic uncertainty.

$$\mathcal{B}(\psi(2S) \to \pi^0 h_c) \times \mathcal{B}(h_c \to p\bar{p}) < 4.8 \cdot 10^{-8} @\ 90\ \% C.L. \tag{8.5}$$

The partial width of the decay $\psi(2S) \to \pi^0 h_c$ was already determined at the BES III experiment in 2010 [14].

$$\mathcal{B}(\psi(2S) \to \pi^0 h_c) = (8.6 \pm 1.3) \cdot 10^{-4} \tag{8.6}$$

The upper limit of the partial width of $h_c \to p\bar{p}$ at 90% C.L. is:

$$\mathcal{B}(h_c \to p\bar{p}) < 5.6 \cdot 10^{-5}\ @\ 90\%\ C.L. \tag{8.7}$$

8.7 Calculation of the Upper Limit Production Cross Section of $p\bar{p} \rightarrow h_c$

As mentioned before, the method of detailed balance was used to derive the upper limit of the production cross section σ. The h_c resonance is described by the Breit Wigner formula:

$$\sigma = \frac{4\pi\,(2J+1)}{s-4m_p^2} \cdot \frac{\mathcal{B}\,(h_c \rightarrow p\bar{p})}{\left[1+2\,(\sqrt{s}-M_{h_c}/\Gamma_{h_c})\right]^2} \tag{8.8}$$

In this formula J is the total angular momentum, $m_p = (938.272046938272046 \pm 0.000021)$ MeV [73] the mass of the proton, $\mathcal{B}\,(h_c \rightarrow p\bar{p})$ the branching ratio of $h_c \rightarrow p\bar{p}$, M_{h_c} and Γ_{h_c} the mass and width of the h_c.

The highest value will be at the peak of this resonance, which implies that the square root of Mandelstam variable s, also known as the center of mass energy, is identical to the mass of the h_c. This simplifies the formula to:

$$\sigma = \frac{4\pi\,(2J+1)}{s-4m_p^2} \cdot \mathcal{B}\,(h_c \rightarrow p\bar{p}) \tag{8.9}$$

The total momentum $J = 1$ of the h_c is fixed per definition and the center of mass energy is $\sqrt{s} = 3.525GeV$ [73]. By using this numbers and the extracted upper limit of $\mathcal{B}\,(h_c \rightarrow p\bar{p})$, the upper limit of the production cross section $h_c \rightarrow p\bar{p}$ at 90 % C.L. can be calculated:

$$\sigma < 2.4 \cdot 10^{-4} GeV^{-2} \text{ @ } 90\%\ C.L. \tag{8.10}$$

By using

$$(\hbar c)^2 = 0.389379338(17) GeV^2 mb \text{ [73]}$$

equals

$$\sigma < 89.6nb \text{ @ } 90\%\ C.L. \tag{8.11}$$

This value is a little above the upper limit of result of the E865 experiment, which would be $\sigma < 73.6nb$ @ 90% $C.L.$ if calculated by using the same method.

8.8 Results Related to the $\overline{\text{P}}$ANDA Physics Program

As mentioned before the total inelastic cross section of proton anti-proton collisions is several orders of magnitude larger than the production cross section of the charmonia. One possibility to overcome this enormous difference is analysing the decay of the investigated charmonia into J/ψ + X, while X may be any other particle like a photon or neutral pions, or even combinations of particles like $\pi^+\pi^-$. The reason for this is that the decay of J/ψ into leptons is very clean. Fot the decay of $h_c \to J/\psi\pi^+\pi^-$ only an coarse upper limit of $\mathcal{B}\left(h_c \to J/\psi\pi^+\pi^-\right) < 0.18$ @ 90 % $C.L.$ was determined by [22].

One very important value which indicates if one is able to measure this branching ratio is the integrated Luminosity $\mathcal{L}_{int}$.

$$\mathcal{L}_{int} = \frac{N}{\sigma_x \cdot \epsilon \cdot \mathcal{B}} \tag{8.12}$$

In this formula σ_x is the cross section of the reaction X of interest, ϵ the efficiency and $\mathcal{B}$ the branching ratio into the final state. A list of estimated instantaneous luminosities for the $\overline{\text{P}}$ANDA experiment is shown in the attachment F.

In particle physics a significance level of 5σ is used to claim a disovery[55]. The significance level is directly correlated to the Z-value, which can be calculated like:

$$Z = \sqrt{2(N_S + N_B)ln(1 + N_S/N_B) - 2N_S} \tag{8.13}$$

whereas N_S and N_B are the estimated number of events in the signal and the background. The lower limit of the integrated luminosity to reach the upper limit of the decay $h_c \to J/\psi\pi^+\pi^-$ can be calculated using:

$$5 \leq \sqrt{2(N_S + N_B)ln(1 + N_S/N_B) - 2N_S} \tag{8.14}$$

Using equation 8.12 and equation 8.14 one can calculate the minimum integrated luminosity:

$$\begin{aligned} \mathcal{L}_{int} &\geq \frac{25}{2(S' + B')ln(1 + S'/B') - 2S'} \qquad (8.15) \\ S' &= S_{ee} + S_{\mu\mu} \end{aligned}$$

$$
\begin{aligned}
S_{ee} &= \sigma_S \cdot \epsilon_{S,ee} \cdot \mathcal{B}_{J/\psi\pi^+\pi^-} \cdot \mathcal{B}_{e^+e^-} \\
S_{\mu\mu} &= \sigma_S \cdot \epsilon_{S,\mu\mu} \cdot \mathcal{B}_{J/\psi\pi^+\pi^-} \cdot \mathcal{B}_{\mu^+\mu^-} \\
B' &= B_{NR,ee} + B_{NR,\mu\mu} + B_{gen,ee} + B_{gen,\mu\mu} \\
B_{NR,ee} &= \sigma_{NR} \cdot \epsilon_{B_{NR,ee}} \\
B_{NR,\mu\mu} &= \sigma_{NR} \cdot \epsilon_{B_{NR,\mu\mu}} \\
B_{gen,ee} &= \sigma_{gen} \cdot \epsilon_{B_{gen,ee}} \cdot \mathcal{B}_{e^+e^-} \\
B_{NR,\mu\mu} &= \sigma_{gen} \cdot \epsilon_{B_{gen,\mu\mu}} \cdot \mathcal{B}_{\mu^+\mu^-}
\end{aligned}
$$

In this equation $\epsilon_{S,ee} + \epsilon_{S,\mu\mu}$ are signal reconstruction efficiencies in case of J/ψ decays into electron positron pairs or $\mu^+\mu^-$, similar in case of the generic background $\epsilon_{B_{gen,ee}} + \epsilon_{B_{gen,\mu\mu}}$ and the non resonant background $\epsilon_{B_{NR,ee}} + \epsilon_{B_{NR,\mu\mu}} = \epsilon_{S,ee} + \epsilon_{S,\mu\mu}$.

σ_S is the production cross section of $p\bar{p} \to h_c$, $\sigma_{gen} = 46\ mb$ [43] the cross section of the generic and $\sigma_{NR} = 1.2\ nb$ [36] of the non resonant background.

$\mathcal{B}_{J/\psi\pi^+\pi^-}$ is the branching ratio of $h_c \to J/\psi\pi^+\pi^-$, $\mathcal{B}_{e^+e^-} + \mathcal{B}_{\mu^+\mu^-} = (5.971 \pm 0.032)\% + (5.961 \pm 0.033)\%$ the branching ratios of J/ψ into electron positron pairs or $\mu^+\mu^-$.

The decay of X(3782) to $J/\psi\pi^+\pi^-$ was studied very precisely in [52]. From his analysis I used the generic as well as the non resonant background studies to approximate the background of the decay $h_c \to J/\psi\pi^+\pi^-$. This is possible, since both backgrounds are very homogenously distributed also in the invariant mass region of the h_c, see figure 8.18. Due to this reason I used this values to calculate the lower limit of the integrated luminosity.

Within the frame of this thesis the same efficiencies as used in the analysis [52] were used in the calculation. They are listed in table 8.4:

	$X(3872) \to J/\psi(e^+e)\pi^+\pi^-$		$X(3872) \to J/\psi(\mu^+\mu)\pi^+\pi$	
Counts	N_S	$N_{B_{gen}}$	N_S	$N_{B_{gen}}$
Generated	98000	$9.58 \cdot 10^9$	100000	$8.87 \cdot 10^9$
Simulated	98000	$1 \cdot 10^7$	100000	$1 \cdot 10^7$
Selection	18704	1099	24233	26005

Table 8.3

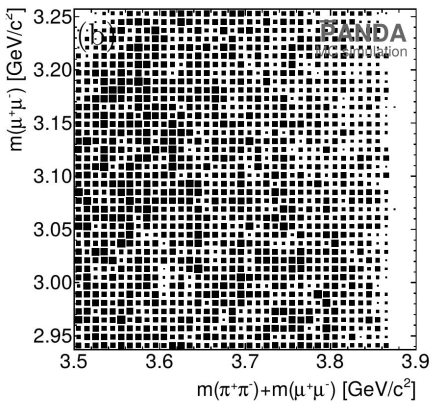

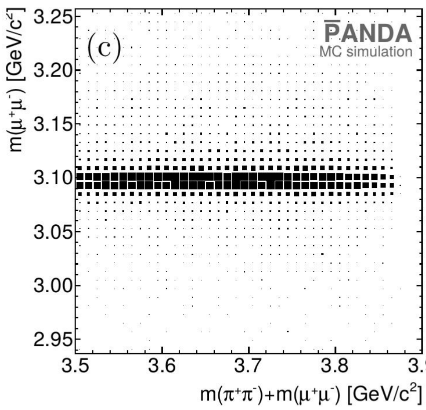

Figure 8.18: Left: Twodimensional plot of the invariant mass distribution of the two muons vs. the invariant mass distribution of the two muons and the two pions for the generic background. Right: Twodimensional plot of the invariant mass distribution of the two muons vs. the invariant mass distribution of the two muons and the two pions for the non resonant background.

By assuming that the cross section would be the same order as the upper limit, the lower limit of the integrated luminosity which is needed to have a significance of 5 σ is:

$$\mathcal{L}_{int} \geq 1.3\, pb^{-1} \text{ @ } 90\%\ C.L. \tag{8.16}$$

By using the estimated luminosities at the energy of the h_c one is able to calculate the lower limit of time t dependent on the stage of FAIR or $\overline{\text{P}}$ANDA respectively. A table of estimated luminosities for various energies can be found in attachment F.

$$t \geq \frac{1.3\, pb^{-1}}{\mathcal{L}_{mode}} \tag{8.17}$$

Here $\mathcal{L}_{mode}$ is the estimated integrated luminosity per day dependent of the mode and the stage of FAIR and the $\overline{\text{P}}$ANDA experiment. HL is the high luminosity mode and HR the high resolution mode, both will be realized in a later stage of FAIR. The start mode will be either the HESR mode or using a recovering of the beam mode HESRr.

mode	Luminosity [nb/d]	time [d]
HL	13475	0.1
HR	1348	1.0
HESR	933	1.4
HESRr	1133	1.2

Table 8.4

By assuming that the cross section is the same order as the measured upper limit, the measuring of $\mathcal{B}(h_c \to J/\psi\pi^+\pi^-)$ would take about 1.5 days in a worst case scenario, in which the HESR mode would be used right in the beginning of FAIR. In a later stage of FAIR, by using the HL mode, this measurement would take only about 2.5 hours.

Chapter 9

Summary & Outlook

This thesis is starting with an introduction of the physics the $\overline{\text{P}}$ANDA experiment will be able to investigate, also an explanation of the $\overline{\text{P}}$ANDA detector is given. Since the $\overline{\text{P}}$ANDA experiment is still under development and is needing input from other experiments, the BES III detector, from which the data for the measurement of the upper limit of the production cross section of h_c in proton anti-proton reactions was taken, is described. Afterwards an illustration of two contributions to the $\overline{\text{P}}$ANDA experiment, including a precise description of the DAQ concept of the $\overline{\text{P}}$ANDA experiment, is given.

The first contribution is the PTDAQ. It is the first version allowing to study the novel DAQ concept of $\overline{\text{P}}$ANDA . The second contribution is the new upper limit of the production cross section of h_c in proton anti-proton collisions. Since both have a great impact to the $\overline{\text{P}}$ANDA experiment, both are summarized separately.

9.1 Summary

The PTDAQ

To study the first principles of the $\overline{\text{P}}$ANDA DAQ a FPGA based prototype trigger-less DAQ was developed. It is a scalable system, starting with one XFP board. This board was developed together with our colleagues from the trigger lab at the high energy physics department located at the IHEP in Beijing, China. A scaled system with more cards was already tested.

To have as much flexibility as possible, several link protocols are implemented: beginning with the lowlevel data link, based on 8b/10b encoding and basic k-characters, via the AURORA protocol from Xilinx up to a UDP implementation [53].

The PTDAQ has several features. Its main task is the burst building, clustering the incoming data streams according to their SBN. Additional features are various filter mechanisms, like coincidences or detector geometries.

Build as a DAQ used for detector prototype tests, the PTDAQ was used in an in-beam environment test of the Proto120 EMC prototype. More than 88 million bursts were successfully build. During the test, no filtering was applied, since it was the first proof of principle for the $\overline{\text{P}}$ANDA DAQ concept. The data was analyzed and no error of the PTDAQ was found. Only in 0.003% of the build bursts one of the DC did not send data, this was handled correctly by the PTDAQ. A more specific analysis of this measurements indicates that the PTDAQ is sufficient to be used as a DAQ in detector prototype tests.

Production Cross-Section

Within this thesis the invariant mass spectrum of $p\bar{p}$ in the decay $\psi(2S) \to p\bar{p}\pi^0$ was analyzed to extract a new production cross section of the h_c charmonium in proton anti-proton collisions. The $\psi(2S)$ itself were produced in electron-positron-collisions. A data set of approximately 447.9 million $\psi(2S)$ decays from the BES III experiment was used.

Before analysing the real data, a Monte Carlo simulation of the signal decay as well as an inclusive Monte Carlo was performed and a reconstruction efficiency of $\epsilon = (31.18 \pm 1.0 \pm 7.7)\%$ was achieved. Furthermore a precise systematic uncertainty exploration was done, before the extraction of a new upper limit of the branching ratio at 90% confidence level is:

$$\mathcal{B}(h_c \to p\bar{p}) < 5.6 \cdot 10^{-5} \text{ @ } 90\%\ C.L. \tag{9.1}$$

It is still above the prediction from Francesco Murgia and still in the same order as the branching ratio of $\chi_2(1P)$. To reach the predictions more data would be needed. Futhermore, it is slightly above the value of the E835 experiment.

Afterwards this value was used to calculate an upper limit at 90% confidence level for the production cross section of h_c in proton anti-proton collisions, using the ansatz of detailed balance.

$$\sigma(p\bar{p} \to h_c) < 89.6\ nb \text{ @ } 90\%\ C.L. \tag{9.2}$$

Using a detailed background analysis from [52] of the decay $X(3872) \to J/\psi\pi^+\pi^-$ as well as the upper limit of the production cross section, the lower limit of integrated luminosity to reach the upper limit of the decay $h_c \to J/\psi\pi^+\pi^-$ was calculated. Under the assumption that the production cross section of h_c is in the same order than the calculated upper limit and on condition of a significance level of 5, the required integrated luminosity at 90% confidence level is:

$$\mathcal{L}_{int} \geq 1.3\ pb^{-1} \text{ @ } 90\%\ C.L. \tag{9.3}$$

Using the estimated luminosities for the several modes, collecting this amount of luminosity at the $\overline{\text{P}}$ANDA experiment in the HL mode would take only 2.5 hours of real data taking. Even in the start version of FAIR this would only take 1.5 days. This concludes that an analysis of this channel is possible aleardy at the beginning of the $\overline{\text{P}}$ANDA experiment. Furthermore, it is an indication that other charmonium and charmonium-like states with similar production cross sections can be analyzed.

9.2 Outlook

In case of the PTDAQ, the next steps would be to test the system with more $\overline{\text{P}}$ANDA prototype detectors. For this, the SODANET implementation at the DC level for more detectors would be needed. Furthermore, more functionalities could be implemented, like for example: the online reconstructing algorithms for the STT from [61] or the cluster finding algorithms for the EMC, which require an upgrade to the full Compute Node.

Since the FPGA of the CN is getting outdated and so is becoming more expensive, a new iteration of the CN with much more powerful FPGAs will be required.

To get a partial width of the $h_c \to p\bar{p}$, more h_c data is necessary. Since the direct production of h_c will not be possible in other experiments than the $\overline{\text{P}}$ANDA experiment, other options would be required.

At the BES III experiment one would have to collect even more $\psi(2S)$ data, which is not foreseen yet. Other experiments like the LHCb or the upcoming experiment Belle II may be an alternative to search for the decay $h_c \to p\bar{p}$.

Danksagung

Bedanken möchte ich mich vor allem bei Prof. Dr. Wolfgang Kühn dafür, dass er mir ermöglichte diese Arbeit zu erstellen. Ganz besonderer Dank gilt Dr. Yutie Liang, für seine tatkräftige Unterstüzung in vielen physikalischen Fragen. Weiterer Dank gebührt auch meinen Eltern Dietmar und Monika Wagner für die Ermöglichung meines Studiums.

Bei meiner Frau Lena möchte ich mich ganz besonders bedanken, da sie in dieser Zeit so wenig von mir hatte und mir so viel andere Arbeit abgenommen hat.

Desweiteren möchte ich mich bei David Münchow für eine angenehme Büroatmosphäre bedanken. Ein Dank gilt auch Pascal Reiter, für viele, vor allem nicht physikalische Unterhaltungen, die eine erholende Abwechslung darstellten. Desweiteren bedanke ich mich noch bei der gesamten Arbeitsgruppe von Prof. Dr. Wolfgang Kühn, für eine sehr nette Atmosphäre während meiner Zeit bei euch. Zum Schluss gilt mein Dank auch sowohl der BES III Kollaboration dafür, dass sie mir die Daten für meine Arbeit zur Verfügung gestellt hat, als auch der $\overline{\text{P}}$ANDA Kollaboration. Hier im Speziellen der Arbeitsgruppe Brinkmann, welche mir die Teilnahme an der Proto120 Strahlzeit ermöglicht hat.

Appendix A

IP Cores

A.1 LocalLink Interfaces (LL)

The interface used in the PTDAQ to transfer large data packages from one core to another is the Xilinx LocalLink interface standard. It is a point to point connection transfering 32-bit words[1] from a source to a destination. The LL uses inverted logic and the minimum of signals which are used are:

Signal	LL used as in put	LL used as out put	valid
Source ready not	I	O	0
Destination ready not	O	I	0
Start of frame	I	O	0
End of frame	I	O	0
Data (32-bit)	I	O	-

If either source or destination are not ready, no data is transfered. The start of frame and the end of frame signal is valid with the first respectively the last word of a frame.

[1] In principle 2n bytes per word are possible. 32-bit is due to the $\overline{\mathrm{P}}$ANDA data format.

A.2 Burst Builder Core

A.2.1 Core properties

- Name: panda_eventbuilder_0
- Current version: v1.00.a
- Type: Standalone

A.2.2 Overview

The burst builder core is the main IP core of the PTDAQ. It sortes and clusters the incoming data frames according to the SBN. It can be configured using the Parameter *Burstbuilder* to be either a frame merger or burst builder. The burst builder core has only two data inputs; to increase the amount of inputs of the PTDAQ the frame merger is used.

- Merger:
  - Sorting the data frames
  - Clustering the data frames
  - Recalculating of the size (if two frames are clustered)
- Burst Builder
  - Sorting the data frames
  - Clustering the data frames
  - Recalculating of the size (if two frames are clustered)
  - Sending additional Header
    - SIZE
    - CAFEBABE
    - Errors (31 downto 16) and ID (15 downto 0)
    - SBN

A.2.3 Ports, Buses and Parameters

The burst builder core has four in- and one output, shown in figure A.1.

As a clock rate the same clock as used in the LL has to be used. For the reset a global reset from the UDP transceiver core can be used. Furthermore the burst builder core has two adjustable parameters:

Signal	I/O
CLK	I
RESET	I
LL_IN_1	I
LL_IN_2	I
LL_out	O

parameter	standart value
ID	0x00001111
Burstbuilder	$\surd$ (If not used the core will behave as a merger.)

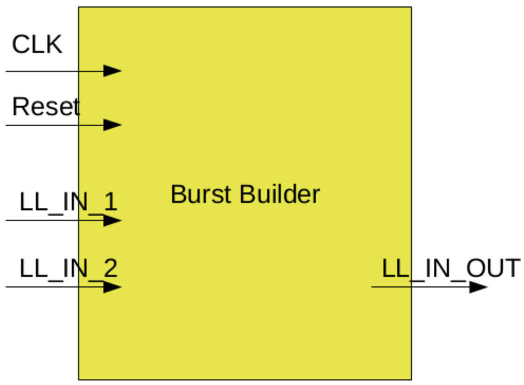

Figure A.1: I/O ports and buses of the burst builder core.

A.3 UDP Transceiver Core

A full description of the UDP core is given in [53]. In this section a description of the settings used in the PTDAQ will be given.

The UDP core uses up to two double GTX of one xFP board, so that it is possible to have up to four UDP connections using the MGTs. Furthermore it supplies a connection to the LL interface. The connectors are adjustable to use them either as a reciever or a transmitter. Each one needs a mac adress, which is also adjustable[2].

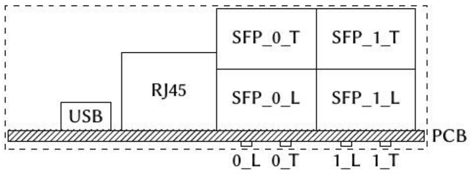

Figure A.2: Front panel view of the xFP board indicating the Connectors placement. Figure is taken from [59].

The following list of pins has to be made to external ports:

- fpga_1_phy_125_clk_pin
- fpga_0_Hard_Ethernet_MAC_TemacPhy_RST_n_pin
- fpga_0_sfp_a_rd_n_pin
- fpga_0_sfp_a_rd_p_pin
- fpga_0_sfp_a_td_n_pin
- fpga_0_sfp_a_td_p_pin
- fpga_0_sfp_b_rd_n_pin
- fpga_0_sfp_b_rd_p_pin
- fpga_0_sfp_b_td_n_pin
- fpga_0_sfp_b_td_p_pin
- fpga_1_sfp_a_rd_n_pin
- fpga_1_sfp_a_rd_p_pin
- fpga_1_sfp_a_td_n_pin

[2]The adress has to be written in big endian.

- fpga_1_sfp_a_td_p_pin
- fpga_1_sfp_b_rd_n_pin
- fpga_1_sfp_b_rd_p_pin
- fpga_1_sfp_b_td_n_pin
- fpga_1_sfp_b_td_p_pin

fpga_0_ and fpga_1_ have to be assigned in the UCF file to the GTX pins. The UDP core in the PTDAQ is only foreseen for the SFP optical transceivers. Their location pins are:

- LOC = GTX_DUAL_X0Y3
- LOC = GTX_DUAL_X0Y4

Appendix B

sADC Connector

To read out the Proto120 using the sADC form Uppsala, a special connector was build together with the electric workshop in Giessen. The sADC is used by several groups in the $\overline{\text{P}}$ANDA collaboration, therefore I publish the schematics in figure B.1 as well as the pcb design in figure B.2.

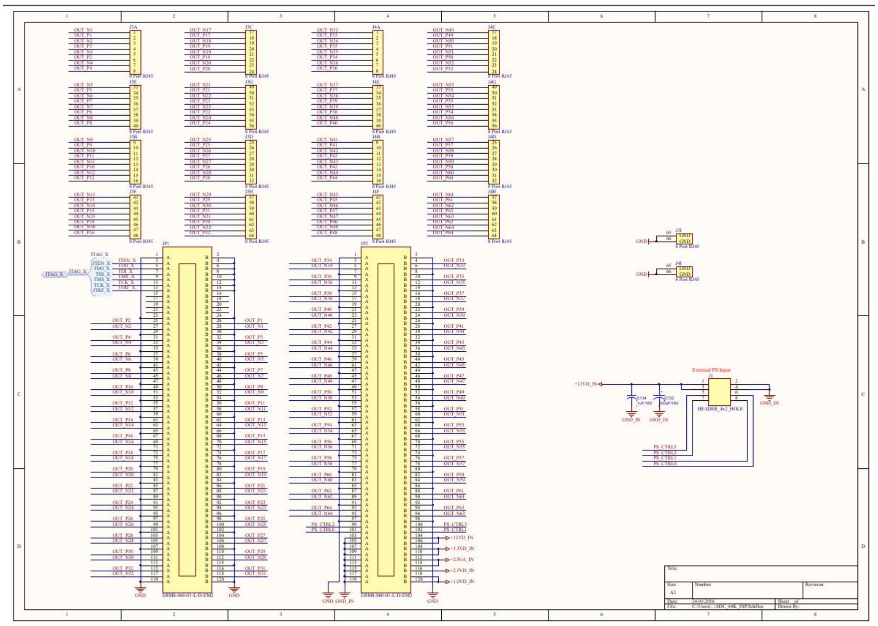

Figure B.1

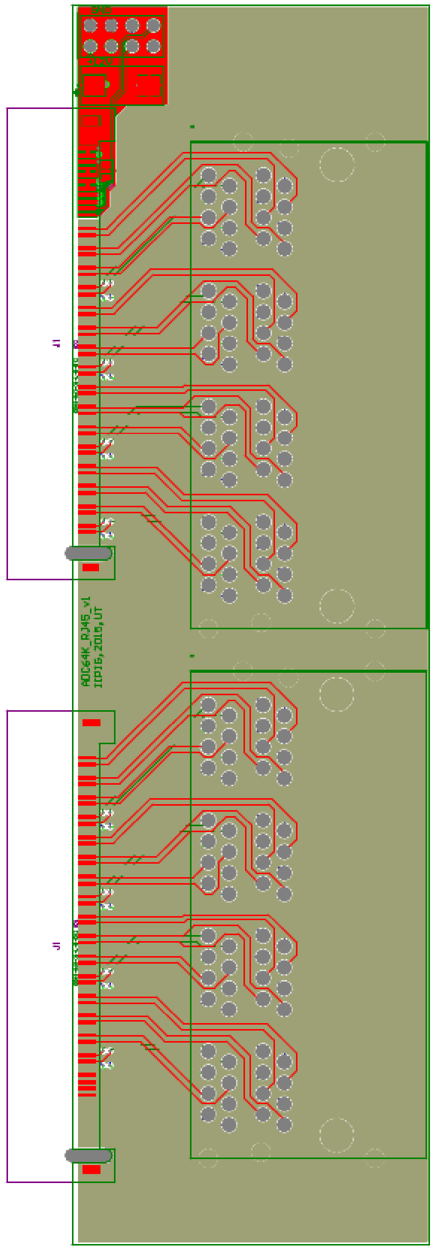

Figure B.2

Appendix C

Differences in the Momentum Distribution of Proton and Anti-proton

To reduce the background of annihilation photons, a broader cut on the angle between the anti-proton track and the photon is applied (see section 8.2). This cut leads to a different momentum distribution for protons and anti-protons. Three different MC samples of 20000 events each were used to figure this out: One with equal cuts for protons and anti-protons, one with a broader cut for anti-protons (equal as in the analysis) and one with a broader cut for protons. Figure C.1 shows that using the same cut results in the same momentum distribution. By changing the broader cut from the anti-proton to the proton, the behaviour changes as it is indicated in figures C.2 and C.3.

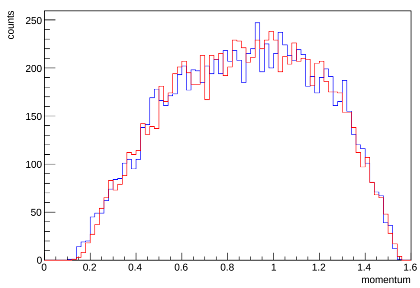

Figure C.1: Proton (blue) and anti-proton (red) momentum distribution for a MC sample of 20000 events using an equal cut.

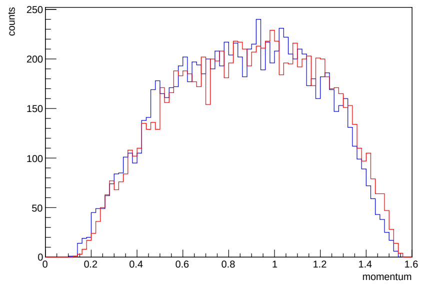

Figure C.2: Proton (blue) and anti-proton (red) momentum distribution for a MC sample of 20000 events using an equal broader cut for anti-protons.

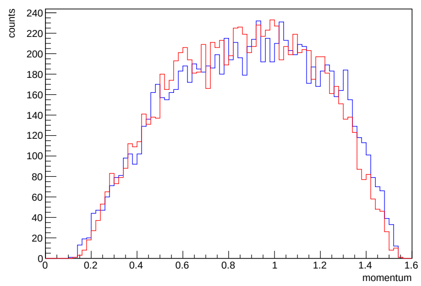

Figure C.3: Proton (blue) and anti-proton (red) momentum distribution for a MC sample of 20000 events using an equal broader cut for protons.

Appendix D

Figure of Merit

The figure of Merit is the final cut of the h_c analysis. This cut was chosen to suppress the background and keep the highest possible efficiency. For this purpose the signal yields of the invariant mass distribution of $p\bar{p}$ in dependence of the χ^2-distribution of the 5C-fit were scanned. Therefore the mean m_{h_c} as well as the standard deviation σ_{h_c} was extracted by fitting the signal in the signal Monte Carlo simulation using a Gaussian distribution.

$m_{h_c} = 3.52621 \pm 0.00004$ GeV/c and $\sigma_{h_c} = 2.45 \pm 0.03 \cdot 10^{-3}$ GeV/c

Afterwards the invariant mass distribution of the signal and the inclusive Monte Carlo simulation were plotted after cutting on three standard deviations to each side of the mean and in addition a cut on the χ^2-distribution of the 5C-fit in binns of 5 was applied. The invariant mass distribution of the signal Monte Carlo is displayed in figures D.1 and D.2, for the inclusive Monte Carlo in figures D.3 and D.4. The extracted values as well as the calculated ones are listed in table D.1.

χ^2	S	B	S+B	$\sqrt(S+B)$	$s/\sqrt(S+B)$
200	3838	18516	22354	149.51254128	25.6700873863
195	3830	17790	21620	147.0374102057	26.0477928348
190	3822	17017	20839	144.3571958719	26.475992256
185	3816	16162	19978	141.3435530896	26.9980477821
180	3808	15343	19151	138.3871381307	27.5170080937
175	3800	14425	18225	135	28.1481481481
170	3797	13645	17442	132.0681642183	28.7503049843
165	3789	12973	16762	129.4681427997	29.2658867121
160	3781	12343	16124	126.9803134348	29.776269232
155	3773	11639	15412	124.1450764227	30.3918617534
150	3767	10813	14580	120.747670785	31.1972891527
145	3761	10313	14074	118.6338906047	31.7025765642
140	3757	9550	13307	115.3559708034	32.5687519583
135	3751	8927	12678	112.5966251715	33.3136094824
130	3743	8253	11996	109.5262525607	34.1744550963
125	3724	7648	11372	106.6395798941	34.9213678795
120	3716	7048	10764	103.7496987947	35.8169714531
115	3707	6572	10279	101.3854032886	36.5634487782
110	3696	6063	9759	98.7876510501	37.4135831828
105	3682	5722	9404	96.9742233792	37.9688526672
100	3668	5177	8845	94.0478601564	39.0014189999
95	3659	4662	8321	91.2195154558	40.1120306517
90	3651	4208	7859	88.6510011224	41.1839680745
85	3632	3772	7404	86.0464990572	42.2097358962
80	3615	3337	6952	83.3786543427	43.3564205191
75	3598	2947	6545	80.9011742807	44.4740145244
70	3574	2604	6178	78.6002544525	45.4705907111
65	3549	2154	5703	75.5182097245	46.9952877981
60	3521	1971	5492	74.1080292546	47.5117208677
55	3485	1715	5200	72.1110255093	48.3282545961
50	3438	1475	4913	70.0927956355	49.0492634632
45	3380	1258	4638	68.1028633759	49.6308059963
40	3322	1071	4393	66.2797103192	50.1209191169
35	3226	809	4035	63.5216498526	50.7858345538
30	3118	633	3751	61.2454079911	50.9099392472
25	2926	445	3371	58.060313468	50.3958698331
20	2698	347	3045	55.1815186453	48.8931813809
15	2335	223	2558	50.5766744656	46.1675273171
10	1746	124	1870	43.2434966209	40.3760134225
5	848	91	939	30.6431068921	27.6734341262

Table D.1: List of all systematic uncertainties, as well as the final sum.

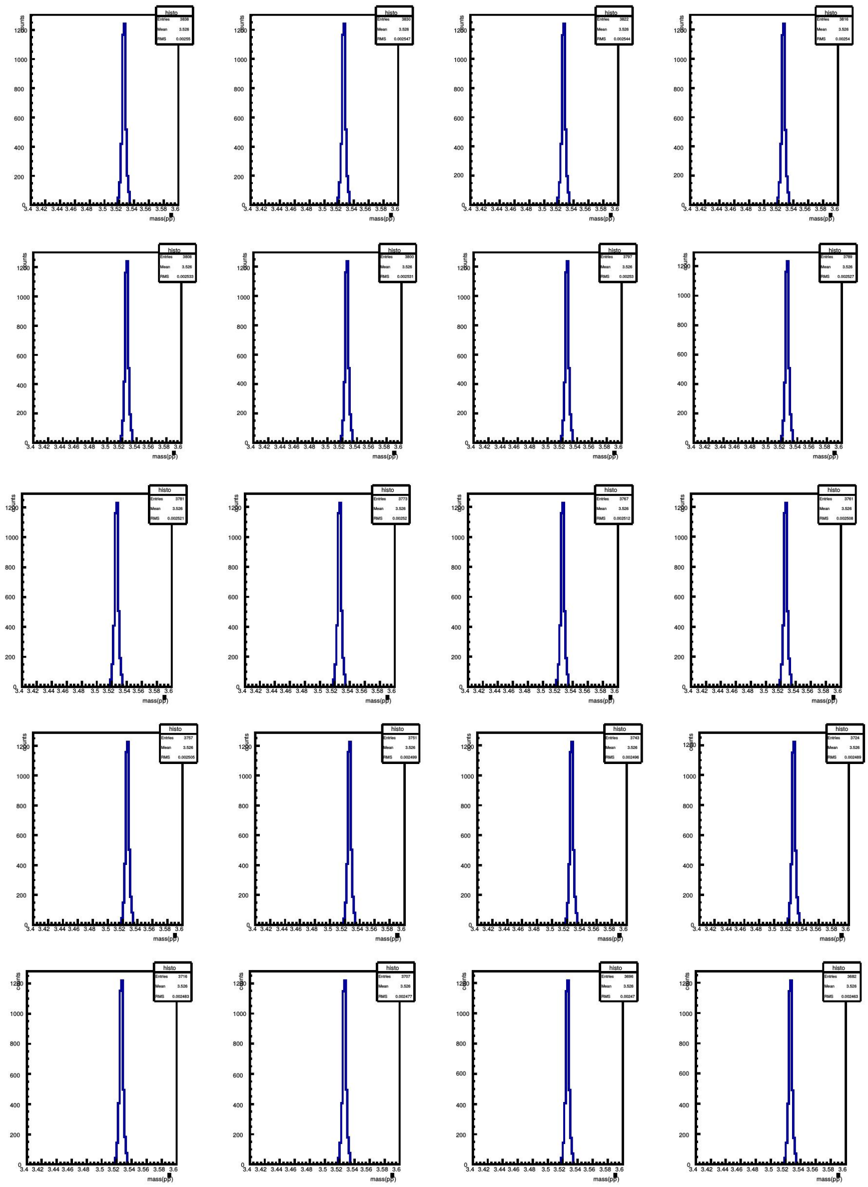

Figure D.1: Invariant mass distribution of $p\bar{p}$ in the signal Monte Carlo. Upper left to lower right: Using a $\chi^2 < 200$ to $\chi^2 < 105$ in steps of -5.

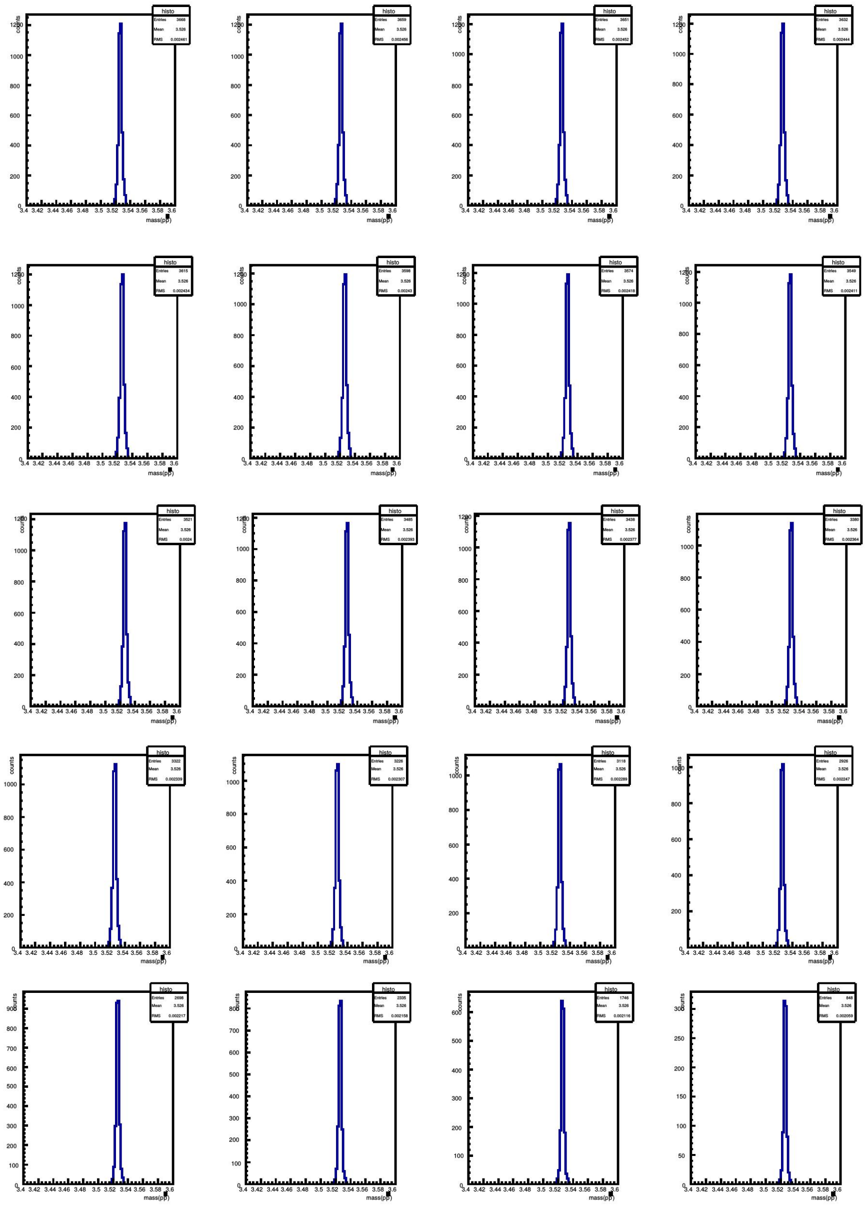

Figure D.2: Invariant mass distribution of $p\bar{p}$ in the signal Monte Carlo. Upper left to lower right: Using a $\chi^2 < 100$ to $\chi^2 < 5$ in steps of -5.

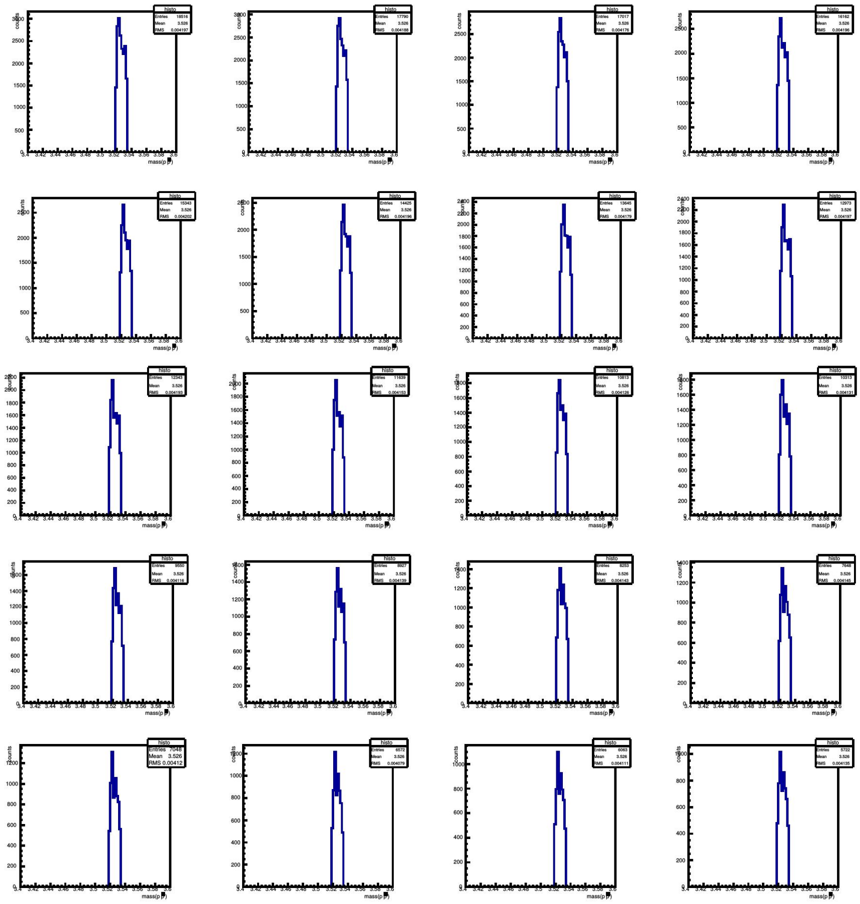

Figure D.3: Invariant mass distribution of $p\bar{p}$ in the inclusive Monte Carlo. Upper left to lower right: Using a $\chi^2 < 200$ to $\chi^2 < 105$ in steps of -5.

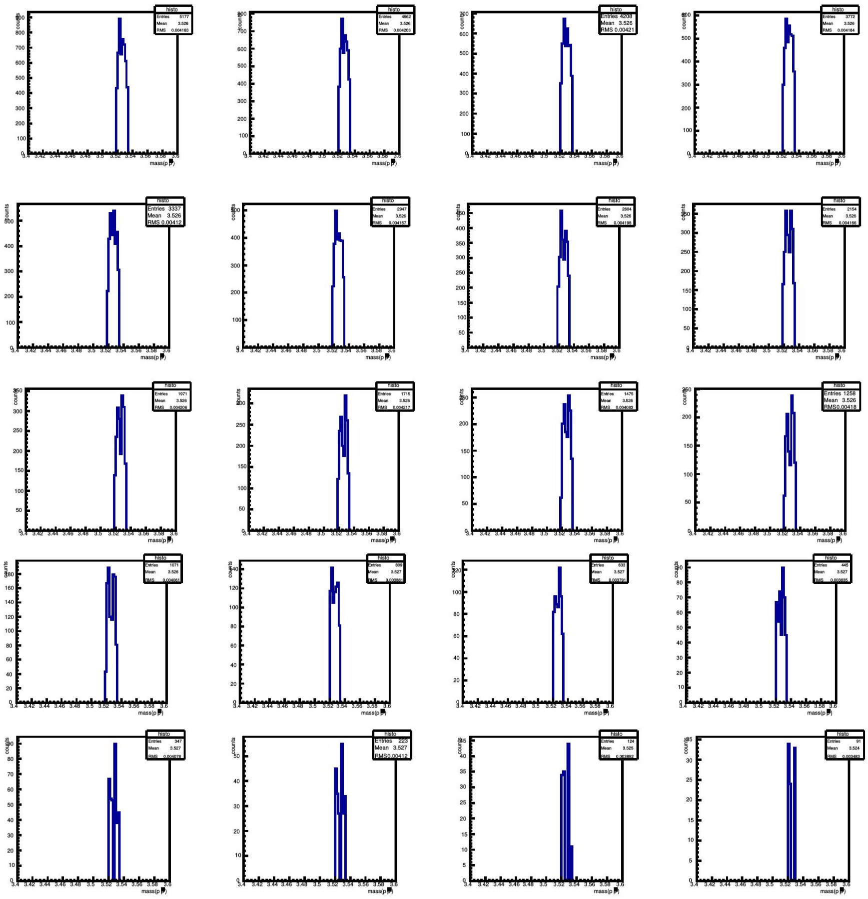

Figure D.4: Invariant mass distribution of $p\bar{p}$ in the inclusive Monte Carlo. Upper left to lower right: Using a $\chi^2 < 100$ to $\chi^2 < 5$ in steps of -5.

Appendix E

Determination of the Likelihood

In figure 8.16 the likelihood profile of entries in the signal yield of the Gaussian distribution fitted to the data is displayed. This profile was used to extract the $-\log likelihood$ and to calculate the likelihood. This allows the calculation of the upper limit of 90% C.L.. The extracted and calculated values are listed in table E.1.

entries	$-\log likelihood$	likelihood
0	1.1216	0.3257581644
1	1.4086	0.2444853231
2	1.7215	0.17879775
3	2.0548	0.1281184567
4	2.411	0.0897255242
5	2.7846	0.0617537856
6	3.1798	0.0415939731
7	3.5908	0.0275762606
8	4.0188	0.0179745214
9	4.4618	0.0115415698
10	4.9175	0.0073174015
11	5.3877	0.004572478
12	5.8726	0.0028155434
13	6.3682	0.0017152439
14	6.8747	0.0010336077
15	7.3926	0.0006157928
16	7.9196	0.0003635477
17	8.4574	0.0002123234
18	9.0062	0.000122647
19	9.5367	$7.21545652729352 \cdot 10^{-5}$
20	10.128	$3.99452816144518 \cdot 10^{-5}$
21	10.7	$2.25449379132122 \cdot 10^{-5}$
22	11.282	$1.25976533930278 \cdot 10^{-5}$
23	11.871	$6.99020971515859 \cdot 10^{-6}$
24	12.468	$3.84783463637208 \cdot 10^{-6}$
25	13.0715	$2.10435826403756 \cdot 10^{-6}$

Table E.1: List of all systematic uncertainties, as well as the final sum.

Appendix F

Luminosity per Day of The $\overline{\text{P}}$ANDA Experiment

The luminosities per day depending on the varius modes explained below are taken from [5] and listed in table F.1.

- HL = High Luminosity mode (accumulation in RESR; rate $R = 2 \cdot 10^7/s$; Nmax=10^{11} antiprotons);
- HR = High Resolution mode (accumulation in RESR; rate $R = 2 \cdot 10^7/s$; Nmax=10^{10} antiprotons);
- HESR = HESR mode (accumulation in HESR with beam dump after cycle; rate $R = 1 \cdot 10^7/s$; Nmax=10^{10} antiprotons);
- HESRr = HESR mode (accumulation in HESR recycling previous beam current; rate$R = 1 \cdot 10^7/s$; Nmax=10^{10} antiprotons);

		$\mathcal{L}$ [1/(nbd]			
p [GeV/c]	Ecm [GeV]	HL	HR	HESR	HESRr
1,5	2,25	6732	1073	627	788
2,0	2,43	8270	1128	689	862
2,5	2,60	9555	1170	737	917
3,0	2,77	10627	1204	776	961
3,5	2,93	11493	1230	809	997
4,0	3,08	12662	1304	871	1070
4,5	3,22	13123	1322	895	1095
5,0	3,36	13363	1336	916	1116
5,5	3,50	13475	1348	933	1133
6,0	3,63	13563	1356	948	1148
6,5	3,75	13631	1363	961	1160
7,0	3,87	13683	1368	972	1170
7,5	3,99	13722	1372	982	1179
8,0	4,11	13751	1375	990	1186
8,5	4,22	13771	1377	998	1192
9,0	4,33	13783	1378	1004	1197
9,5	4,44	13790	1379	1010	1202
10,0	4,54	13792	1379	1015	1205
10,5	4,64	13791	1379	1020	1208
11,0	4,74	13786	1379	1024	1211
11,5	4,84	13778	1378	1028	1213
12,0	4,93	13769	1377	1031	1215
12,5	5,03	13757	1376	1034	1216
13,0	5,12	13744	1374	1037	1217
13,5	5,21	13730	1373	1039	1218
14,0	5,30	13714	1371	1041	1219
14,5	5,39	13698	1370	1043	1219
15,0	5,47	13681	1368	1045	1220
15,5	5,56	13663	1366	1047	1220

Table F.1: List of all systematic uncertainties, as well as the final sum.

Appendix G

Calculation of the Significance Level

The significance level is directly related to the p-value, so that a p-value of 0.05 is related to a significance level of 1.68σ. In particle physics an evidence is claimed if the significance level is above 3σ and an observation above 5σ. To calculate the significance level one uses the Z-value which is:

$$Z = \Phi^{-1}(1 - p) \tag{G.1}$$

where Φ^{-1} is the significance level cumulative distribution function of the unit Gaussian[55]. In addition the Z-value can either be calculated like:

$$Z = \sqrt{2 \ln L_{SB}/L_B} \tag{G.2}$$

whereas L_{SB} and L_B are the maximum likelihood obtained by fitting the data with signal and background and pure background. As an approximation often:

$$Z = \frac{S}{\sqrt{S + B}} \tag{G.3}$$

is used. Nevertheless a more accurate approach is to insert the Poisson likelihood terms in equation G.2 to obtain by using [55]:

$$Z = \sqrt{2(S + B)ln(1 + S/B) - 2S} \tag{G.4}$$

whereas S and B are the estimated amount of signal and background events.

Appendix H

LIST OF ABBREVIATIONS

AMC	Advanced Mezzanine Card
APFEL ASIC	ASIC for $\overline{\text{P}}$ANDA Front-end Electronics
APPA	Atomic and Plasma Physics and Applications
ASIC	Application-Specific Integrated Circuit
ATCA	Advanced Telecommunications Computing Architecture
BBN	Burst Building Network
BEPC	Beijing Electron-Positron Collider
BEPC II	second generation Beijing Electron-Positron Collider
BES	Beijing Electron Spectrometer
BES III	third generation of the Beijing Electron Spectrometer
BNL	Brookhaven National Laboratory
C.L.	Confidence Level
CBM	Compressed Baryonic Matter
CMS	Compact Muon Solenoid
CN	Compute Node
CPU	Central Processing Unit
CR	Collector Ring
DAQ	Data Acquisition
DC	Data Concentrator
DIRC	Detection of Internally Reflected Cherenkov
EBN	Event Building Network
EFN	Event Filter Network
EMC	Electromagnetic Calorimeter
ESR	Experimental Storage Ring

FAIR	Facility for Anti-proton and Ion Research
FEE	Front End Electronic
FPGA	Field-Programmable Gate Array
FRS	Fragment Separator
FWHM	Full Width at Half Maximum
GEM	Gas Electron Multiplier
GPCPU	General-Purpose computing on Graphics Processing Unit
GPD	Generalized Parton Distribution
GSI	Gesellschaft für Schwerionen
HDL	Hardware Description Language
HDSM	Harmonic Double Sided Microtron
HESR	High Energy Experimental Storage Ring
HL	High Luminosity mode
HR	High Resolution mode
HV-MAPS	High Voltage-Monolithic Active Pixel Sensor
IHEP	Institute of High Energy Physics
IP	Interaction Point
IPMI	Intelligent Platform Management Interface
LAAPD	Large Area Avalanche Photo Diode
LINAC	Linear Accelerator
LL	LocalLink Interfaces
LNP-P	Low Noise and Low Power charge Preamplifier
LUT	Lookup Table
LY	Relative Light Yield
MAMI	Mainzer Microtron
MC	Monte Carlo
MCP PMT	Micro-Channel Plate Photomultiplier Tubes
MDC	Mini Drift Chamber
MDT	Mini Drift Tube
MGT	Multi-Gigabit Transceiver
MVD	Micro Vertex Detector
NESR	New Experimental Storage Ring
NUSTAR	Nuclear Structure, Astrophysics and Reactions
ONSEN	Online Selection Nodes
p-LINAC	Linear Accelerator
PANDA	Anti-Proton Annihilation at Darmstadt
PASTA	PANDA Strip Asic
PCB	Printed Circuit Board
PHY	Ethernet Physical transceiver
PID	Particle Identification
PM	Photo Multiplier
PTDAQ	Prototype Trigger-less Data Acquisition
PWO	$PbWO_4$
PWO-II	second version of PWO
QCD	Quantum Chromodynamics
QE	Quantum Effeciency
QED	Quantum Electrodynamic
QFT	Quantum Field Theory

RICH	Ring Imaging Cherenkov Detector
RMS	Root Mean Square
RPC	Resistive Plate Chamber
RTM	Race Track Microtron
sADC	sampling Analog to Digital Converter
SBC	Super-Burst-Command
SBN	Super-Burst-Number
SC	Superconducting
SIS 100	Synchrotrons 100
SIS 18	Synchrotrons 18
SIS 300	Synchrotrons 300
SLAC	Stanford Linear Acclerator Center
SM	Standard Model
SODANET	Synchronization Of Data Acquisition Network
STT	Straw Tube Tracker
TDA	Transition Distribution Amplitude
ToF	Time of Flight
TRBv3	third version of the Trigger and Readout Board
UDP	User Datagram Protocol
VHDL	Very high speed integrated circuit (V)HDL
VPPT	Vacuum Photo Tetrode
xFP	xTCA-based FPGA Processor
xTCA	extended Telecommunications Computing Architecture for physics standard

List of Tables

List of Figures

Bibliography

[1] Advanced mc mezzanine module specification. version 2.0. 2006.

[2] Advanced tca base specification. 2008.

[3] https://indico.gsi.de/conferenceotherviews.py?showsession=all&showdate=all&view=nicecompact&confid=3446.

[4] https://panda-wiki.gsi.de/foswiki/bin/view/daq/webhome.

[5] https://panda-wiki.gsi.de/foswiki/pub/physics/webhome/lumitable.pdf.

[6] https://panda.gsi.de/ oldwww/ framework/ det_iframe.php?section= full %20view.

[7] http://www.kph.uni-mainz.de/bildergalerie/mami_06.jpg (accessed nov. 2015).

[8] http://www.kph.uni-mainz.de/mami.php.

[9] *Xilinx, Inc. DS100. Virtex-5 Family Overview. Version 5.1. 2015. url:* $http : //www.xilinx.com/support/documentation/data_sheets/ds100.pdf..$

[10] *Charmonium Spectroscopy at BaBar*. Proceeding of the 4th High-Energy Physics Conference in Madagascar, 2009.

[11] P. E. V. A. B. Kaidalov. Binary reactions in $p\bar{p}$ collisions at intermediate energies. *Zeitschrift fr Physik C Particles and Fields Volume 63, Issue 3, pp 517-524*, 1994.

[12] R. Aaij et al. Determination of the x(3872) meson quantum numbers. *arXiv:1302.6269*, 2013.

[13] M. Ablikim et al. Design and Construction of the BESIII Detector. *Nucl. Instrum. Meth.*, A614:345–399, 2010.

[14] M. Ablikim et al. Measurements of $h_c(^1P_1)$ in psi' Decays. *Phys. Rev. Lett.*, 104:132002, 2010.

[15] M. Ablikim et al. Determination of the number of J/ψ events with $J/\psi \to$ *inclusive* decays. *Chin. Phys.*, C36:915–925, 2012.

[16] M. Ablikim et al. Observation of a Charged Charmoniumlike Structure in $e^+e^- \to {}^{+-}$ J/ψ at $\sqrt{s}$ =4.26GeV. *Phys. Rev. Lett.*, 110:252001, 2013.

[17] M. Ablikim et al. Search for ${}_c(2S)h_c \to p\bar{p}$ decays and measurements of the ${}_{cJ} \to p\bar{p}$ branching. *Phys. Rev.*, D88(11):112001, 2013.

[18] M. Ablikim et al. Study of $e^+e \to p\bar{p}$ in the vicinity of $\psi(3770)$. *Phys. Lett.*, B735:101–107, 2014.

[19] e. a. Adler, S. S. j/ψ production and nuclear effects for $d + au$ and $p + p$ collisions at $\sqrt{s_{NN}} = 200gev$. *Phys. Rev. Lett.*, 96:012304, Jan 2006.

[20] C. Amsler and F. E. Close. Is f0 (1500) a scalar glueball? *Phys. Rev.*, D53:295–311, 1996.

[21] M. Andreotti et al. Results of a search for the h(c) (1)P(1) state of charmonium in the eta(c) gamma and J/psi pi0 decay modes. *Phys. Rev.*, D72:032001, 2005.

[22] T. A. Armstrong et al. Observation of the p wave singlet state of charmonium. *Phys. Rev. Lett.*, 69:2337–2340, 1992.

[23] D. M. Asner et al. Physics at BES-III. *Int. J. Mod. Phys.*, A24:S1–794, 2009.

[24] B. Aubert et al. Observation of a broad structure in the $\pi^+\pi^- J/\psi$ mass spectrum around 4.26-GeV/c^2. *Phys. Rev. Lett.*, 95:142001, 2005.

[25] B. Aubert et al. Evidence for $X(3872) \to \psi_{2S}\gamma$ in $B^\pm \to X_{3872}K^\pm$ decays, and a study of $B \to c\bar{c}\gamma K$. *Phys. Rev. Lett.*, 102:132001, 2009.

[26] J. J. e. a. Aubert. Experimental observation of a heavy particle j. *Phys. Rev. Lett.*, 33:1404–1406, Dec 1974.

[27] e. a. Augustin, J. E. Discovery of a narrow resonance in e^+e^- annihilation. *Phys. Rev. Lett.*, 33:1406–1408, Dec 1974.

[28] A. V. Belitsky and A. V. Radyushkin. Unraveling hadron structure with generalized parton distributions. *Phys. Rept.*, 418:1–387, 2005.

[29] S. Bethke. Experimental tests of asymptotic freedom. *Prog. Part. Nucl. Phys.*, 58:351–386, 2007.

[30] V. Bhardwaj et al. Observation of $X(3872) \to J/\psi\gamma$ and search for $X(3872) \to \psi'\gamma$ in B decays. *Phys. Rev. Lett.*, 107:091803, 2011.

[31] M. Böhm. *Lie-Gruppen und Lie-Algebren in der Physik*. Springer-Lehrbuch. Springer, 2011.

[32] E. Braaten. Estimate of the partial width for x(3872) into $p\bar{p}$. *Phys. Rev. D 77, 034019*, 2008.

[33] S. J. Brodsky and G. P. Lepage. S. j. brodsky and g. p. lepage, phys. rev. d. *Phys. Rev. D*, 1981.

[34] D. V. Bugg. How Resonances can synchronise with Thresholds. *J. Phys.*, G35:075005, 2008.

[35] R. Chan, L.-H.; O'Connell. Charmonium-the ^1p"1 state. *Physics Letters B 76, S. 121-124*, 1978.

[36] G. Y. Chen and J. P. Ma. Production of $x(3872)$ at panda. *Phys. Rev. D*, 77:097501, May 2008.

[37] C. T. H. Davies et al. High-precision lattice qcd confronts experiment. *Phys. Rev. Lett.*, 92:022001, Jan 2004.

[38] S. Diehl. *Optimization of the Influence of Longitudinal and Lateral Non-Uniformity on the Performance of an Electromagnetic Calorimeter*. PhD thesis, JLU Giessen, 2016.

[39] W. Erni et al. Technical Design Report for PANDA Electromagnetic Calorimeter (EMC). 2008.

[40] J. M. B. et al. Validation/dq group meeting,, Step. 21 2009.

[41] X. B. J. et al. Validation/dq group meeting,, Oct. 10, 2011.

[42] E. Fermi. Exchange forces between neutrons and protons, and fermi's theory. *Nature*, 1934.

[43] e. a. Flaminio. Compilation of cross-sections. *CERN-HERA-84-01*, (1984).

[44] T. Geler, W. Khn, J. S. Lange, Z. Liu, D. Mnchow, B. Spruck, and J. Zhao. The ONSEN Data Reduction System for the Belle II Pixel Detector. *IEEE Trans. Nucl. Sci.*, 62(3):1149–1154, 2015.

[45] S. L. Glashow, J. Iliopoulos, and L. Maiani. Weak Interactions with Lepton-Hadron Symmetry. *Phys. Rev.*, D2:1285–1292, 1970.

[46] M. Hoek et al. The PANDA Barrel DIRC detector. *Nucl. Instrum. Meth.*, A766:9–13, 2014.

[47] e. a. I. Konorov. soda: Time distribution system for the panda ex- periment. *Nuclear Science Symposium Conference Record (NSS/MIC), p.1863*, 2009.

[48] F. Iachello and Q. Wan. Structure of the nucleon from electromagnetic timelike form factors. *Phys. Rev.*, C69:055204, 2004.

[49] J. Iizuka. A systematics and phenomenology of meson family. *Journal of the Physical Society of Japan*, 1966.

[50] R. K. F. N. K. Götzen, D. Kang. Panda software trigger status/plans. talk.

[51] M. Kavatsyuk et al. Trigger-less readout of the panda electromagnetic calorimeter. In *Nuclear Science Symposium and Medical Imaging Conference (NSS/MIC), 2012 IEEE*, pages 1796–1801, Oct 2012.

[52] F. N. K. P. Klaus Götzen, Ralf Kliemt. Simulation study of the width and line shape of the x(3872).

[53] G. Korcyl. *A novel Data Acquisition System based on fast optical links and universal read-out boards.* PhD thesis, AGH-UST, Cracow, 2015.

[54] B. S. W. Kroll, P.; Quadder. Exclusive production of heavy flavours in proton-antiproton annihilation. *Nuclear Physics, Section B, Volume 316, Issue 2, p. 373-390*, 1989.

[55] B. O. S.-S. T. S. G. Krninger, Kevin. *Data Analysis in High Energy Physics.* Wiley, 2013.

[56] E. A. Kuraev, E. S. Kokoulina, and E. Tomasi-Gustafsson. Light meson emission in (anti)proton induced reactions. In *Proceedings, 22nd International Baldin Seminar on High Energy Physics Problems, Relativistic Nuclear Physics and Quantum Chromodynamics, (ISHEPP 2014)*, 2015.

[57] W. Khn, C. Gilardi, D. Kirschner, J. Lang, S. Lange, M. Liu, T. Perez, S. Yang, L. Schmitt, D. Jin, L. Li, Z. Liu, Y. Lu, Q. Wang, S. Wei, H. Xu, D. Zhao, K. Korcyl, J. T. Otwinowski,

P. Salabura, I. Konorov, and A. Mann. Fpga based compute nodes for high level triggering in panda. *Journal of Physics: Conference Series*, 119(2):022027, 2008.

[58] L. Maiani, A. D. Polosa, V. Riquer, . *Phys. Rev. Lett. 99(2007)182003*, 2007.

[59] T. G. ler. *Development of FPGA-Based Algorithms for the Data Acquisition of the Belle II Pixel Detector*. PhD thesis, JLU GIessen, 2015.

[60] Y. Liang. Fpga helix tracking algorithm for panda.

[61] Y. Liang. Fpga online tracking algorithm for the panda straw tube tracker.

[62] X.-H. Liu and Q. Zhao. Further study of the helicity selection rule evading mechanism in η_c, χ_{c0} and h_c decaying to baryon anti-baryon pairs. *J. Phys.*, G38:035007, 2011.

[63] M. F. M. Lutz et al. Physics Performance Report for PANDA: Strong Interaction Studies with Antiprotons. 2009.

[64] P. L. O. K. M. Kavatsyuk, P. Schakel. Status of the sodanet. Talk.

[65] P. MARCINIEWSKI. Emc digitizers and data concentrators. talk.

[66] J. C. McGeorge et al. Upgrade of the Glasgow photon tagging spectrometer for Mainz MAMI-C. *Eur. Phys. J.*, A37:129–137, 2008.

[67] J. Michel, I. Frhlich, M. Bhmer, G. Korcyl, L. Maier, M. Palka, J. Stroth, M. Traxler, and S. Yurevich. The hades trigger and readout board network (trbnet). In *Real Time Conference (RT), 2010 17th IEEE-NPSS*, pages 1–5, May 2010.

[68] R. E. Mitchell et al. J/psi and psi(2S) Radiative Decays to eta(c). *Phys. Rev. Lett.*, 102:011801, 2009. [Erratum: Phys. Rev. Lett.106,159903(2011)].

[69] F. Murgia. The p wave singlet charmonium state decay into p anti-p in QCD models including constituent quark mass corrections. *Phys. Rev.*, D54:3365–3373, 1996.

[70] N. N. A. Tornqvist, Phys. Rev. Lett. 67(1991)556.

[71] H. T. O. Hashimoto. Spectroscopy of λ hypernuclei. *Progress in Particle and Nuclear Physics, Volume 57, Pages 564653*, 2006.

[72] S. Okubo. ϕ-meson and unitary symmetry model. *Physics Letters, Volume 5, Issue 2, Pages 165-168*, 1965.

[73] K. A. Olive et al. Review of Particle Physics. *Chin. Phys.*, C38:090001, 2014.

[74] S. L. Olsen. Search for a charmonium assignment for the x(3872). *Int.J.Mod.Phys. A20 (2005) 240-249*, 2004.

[75] PANDA Collaboration, W. Erni, I. Keshelashvili, B. Krusche, M. Steinacher, Y. Heng, Z. Liu, H. Liu, X. Shen, Q. Wang, and et al. Technical Design Report for the: PANDA Micro Vertex Detector. *ArXiv e-prints*, July 2012.

[76] M. E. Peskin and D. V. Schroeder. *An Introduction To Quantum Field Theory*. Levant Books, 2005.

[77] B. Pire and L. Szymanowski. Hadron annihilation into two photons and backward virtual compton scattering in the scaling regime of qcd. *Phys. Rev. D*, 71:111501, Jun 2005.

[78] B. Pire and L. Szymanowski. QCD analysis of anti-p N —¿ gamma* pi in the scaling limit. *Phys. Lett.*, B622:83–92, 2005.

[79] V. S. P. S. R. Br, U. Krause. The new fair accelerator complex at gsi: Project, controls, challenges and first steps,. *Proceedings of ICALEPCS07*, 2007.

[80] S. Reiter. Test of pcie based readout option for the panda experiment. to be published.

[81] C. Rosenbaum. Optimization of the front-end electronics of the panda emc. to be published.

[82] P. Sievers, K. Knie, M. Steck, B. Franzke, and V. Gostishchev. Concept for the Antiproton Production Target at FAIR. *Conf. Proc.*, C1205201:2570–2572, 2012.

[83] B. Spruck, T. Geler, W. Khn, J. S. Lange, H. Lin, Z. Liu, D. Mnchow, H. Xu, and J. Zhao. The belle ii pixel detector data acquisition and reduction system. In *Real Time Conference (RT), 2012 18th IEEE-NPSS*, pages 1–5, June 2012.

[84] H. Stockhorst, D. Prasuhn, R. Maier, B. Lorentz, F. J. Gmbh, and T. K. Tokyo. Stochastic cooling for the hesr at the gsi-fair complex*.

[85] E. S. Swanson. Z_b and Z_c exotic states as coupled channel cusps. *Phys. Rev. D*, 91:034009, Feb 2015.

[86] E. Tomasi-Gustafsson. Proton Form Factors: phenomenology. *Nuovo Cim.*, C034N06:208–212, 2011.

[87] M. Traxler, E. Bayer, M. Kajetanowicz, G. Korcyl, L. Maier, J. Michel, M. Palka, and C. Ugur. A compact system for high precision time measurements (¡ 14 ps rms) and integrated data acquisition for a large number of channels. *Journal of Instrumentation*, 6(12):C12004, 2011.

[88] M. G. Ullrich. *Measurement of sigma (psi(3770) to proton antiproton neutral pion) and determination of sigma (proton antiproton to psi(3770)neutral pion) for the PANDA experiment*. PhD thesis, Justus-Liebig-Universitt, Otto-Behaghel-Str. 8, 35394 Gieen, 2013.

[89] S. Weinberg. A model of leptons. *Physicsl Review Letters,Volume 19, Number 21*, 1967.

[90] P. Wieczorek. Preliminary results of the apfel 1.4 measurements,.

[91] A. K. Wrblewski. Hypernuclei(and strange particles)how it all began? *ACTA PHYSICA POLONICA B*, 2004.

[92] T. Xiao, S. Dobbs, A. Tomaradze, and K. K. Seth. Observation of the Charged Hadron $Z_c^{\pm}(3900)$ and Evidence for the Neutral $Z_c^0(3900)$ in $e^+e^- \to \pi\pi J/\psi$ at $\sqrt{s} = 4170$ MeV. *Phys. Lett.*, B727:366–370, 2013.

[93] J. Zhao, Z. A. Liu, H. Xu, W. Gong, K. Wang, H. Lin, F. Guo, W. Kuehn, T. Gessler, C. Wang, Z. Liu, and F. Deng. A general xtca compliant and fpga based data processing building blocks for trigger and data acquisition system. In *Real Time Conference (RT), 2014 19th IEEE-NPSS*, pages 1–4, May 2014.

[94] G. Zweig. *CERN Report No.8419/TH412*, 1964.